Measurement of Material Nonlinearity using Laser Ultrasound

by Ian J Collison, MEng

Thesis submitted to the University of Nottingham
for the degree of Doctor of Philosophy, July 2008

Abstract

The aim of the work in this thesis was to develop an NDT technique capable of measuring velocity changes caused by an applied stress.

A dual frequency mixing technique was used to perform the experiments, in which the interaction between two surface acoustic waves (SAWs) was observed. The pump SAW, generated by a transducer, stressed the sample surface. The probe SAW was generated by an Optical Scanning Acoustic Microscope (OSAM), capable of generating ultrasound at 82MHz and its harmonics. The level of stress experienced by the probe SAW was adjusted by controlling the pump-probe interaction-point using a system of timing electronics. The nonlinear interaction was directly measured as a phase modulation of the probe SAW and equated to a velocity change. Detection of both SAWs was achieved using a knife-edge detector. The stresses exerted by the transducer were typically $<$10MPa and the velocity-stress relationship provided a measure of material nonlinearity.

The technique described herein was sensitive to changes in temperature and, therefore, several temperature suppression techniques were developed to improve acquisition of results. CHeap Optical Transducers (CHOTs) were integrated into the experiment and the measurements obtained using these devices were similar to those acquired using the knife-edge detector.

Velocity changes of 115.2mms^{-1}/MPa, -34.4mms^{-1}/MPa and -31.9mms^{-1}/MPa were measured on fused silica, Al-2024 and Al-6061, respectively. Experiments showed that fused silica and aluminium had opposite nonlinear responses, consistent with previous published data. The work in this thesis could be applied to fatigue measurements, for example in the aeronautics industry, to safely and reliably extend the useable life of aircraft engine components.

Acknowledgements

I would first of all like to thank my supervisor Dr M Clark for all of his guidance, support and suggestions throughout this research. Thanks go to Professor M Somekh for his advice and assistance and also to Dr S Sharples who has always been willing to advise. I also express my gratitude to Teti Stratoudaki for our endless, yet enjoyable, discussions and for her encouragement. Thanks go to José Hernández and to my other colleagues: Richard Smith, Robert Ellwood and Wen-qi Li.

My appreciation also goes to the technicians at Nottingham University for allowing me to use their facilities and to Brian Webster for providing his expertise on sample preparation and allowing me to perform experiments on the fatiguing machines in the Mechanical Engineering Department. In addition, I thank Katy Milne and the technicians at Rolls-Royce for their help with fatiguing samples.

My gratitude must also extend to my family and friends for their continued support and encouragement.

Contents

Chapter 1

Introduction

1.1 Objective and outline of thesis

The work in this thesis was based on the development of a sensitive, robust and repeatable nondestructive testing (NDT) technique capable of measuring velocity changes caused by applied stress. The velocity-stress relationship is a direct measurement of material nonlinearity.

The motivation for this work was to investigate the changes in material nonlinearity caused by fatigue. From a material-science perspective, this technique is an extremely powerful tool for accurate material qualification and can be applied to many areas of industry, such as the aerospace industry for example.

The experiments used a dual frequency mixing technique in which the interaction between two surface acoustic waves (SAWs) was observed. A low frequency (500kHz−2MHz) pump SAW was generated by a transducer, which stressed the surface of the sample as it propagated. The high frequency (82MHz, 164MHz, 246MHz) probing SAW, was generated by the Optical Scanning Acoustic Microscope (OSAM) instrument [1].

By altering the point of interaction between the two SAWs, the stress experienced by the probe was controlled, and a change in velocity was directly measured in the phase of the high frequency probe SAW. Ultrasound detection was performed by a knife-edge detector. In addition, the application of CHOTs provided an alternative method to generate and detect ultrasound. The advantage of performing this experiment with lasers was that the experiment was non-contact. Moreover, the benefits of generating and detecting ultrasound with lasers include a higher spatial resolution compared with contact methods and the ability to perform couplant-free experiments.

The ultrasound generated by the laser system in the OSAM instrument had a frequency of 82MHz, meaning that a relatively high pump:probe SAW frequency ratio was possible, compared with previous experiments described in the literature. For example, Vila *et al* (2004) used 2.5MHz and 20MHz bulk waves for the pump and probe sources, respectively [2]. The attraction of a high pump:probe ratio was that the penetration depth of the probe SAW was only $\sim 1\%$ of the pump SAW. Thus, the theory was simplified substantially because the probe SAW experienced only the longitudinal component of stress, while all other stress components go to zero at the surface of the material [3]. This is discussed in detail in section 1.4.2.

The purpose of this chapter is to introduce the common NDT techniques readily used in industry, with emphasis on ultrasonic techniques and sections 1.6 and 1.7 describe various laser ultrasonic generation and detection techniques.

Chapter 2 is a literature review which describes material elasticity and discusses other nonlinear experimental techniques that are under current investigation. For example, an alternative experiment to the one presented in this thesis that is commonly used to measure material nonlinearity is based on measuring the harmonic content of a single frequency wave as it propagates over, or through, the test material. However, the difficulty with this experiment is successfully separating the nonlinearity of the experimental apparatus from the material nonlinearity. Various components, including the amplifier electronics, transducers, wedges and couplant all contribute to some degree to the measured harmonic content, and, therefore, these must be accounted for. The technique presented in this work is immune to this problem because the inter-modulation of two independent SAWs was being measured.

Chapter 3 describes the OSAMs optical setup for the generation and detection of ultrasound, as well as the detector electronics and calibration scheme. During the course of this work, it was found that the stress-related velocity-change measurements were affected by changes in temperature. Various methods were developed to suppress the temperature effect which are presented in Chapter 4.

The generation laser system in the OSAM is capable of generating SAWs at a fundamental frequency of 82MHz, as well as at the harmonics. Therefore, in addition to using the fundamental frequency, the nonlinear experiment could also be performed using frequencies of 164MHz and 246MHz, as demonstrated in Chapter 5.

The materials that were investigated in this work were fused silica and aluminium. These materials were selected because they have a relatively high nonlinearity property [4], compared with other materials (e.g. steel, gold, titanium, copper and silver) making them most appropriate for the development of a nonlinear experiment.

In the literature, the material nonlinearity is often quantified using the β (‘nonlinear’) parameter. Although it is possible to quantify the fatigue level of a material by measuring changes in β, material nonlinearity was not measured using this method in the work presented here. Instead, the relationship between velocity change and stress provided the quantitative measure of nonlinearity. This can be referred to as a measurement of acoustoelasticity i.e the stress dependence of acoustic wave velocity in elastic media [5].

According to the literature, fused silica and aluminium are reported to have opposite nonlinear responses [4]. In order to validate this experiments were performed on these materials and the results are presented in Chapter 5.

In parallel with the nonlinear research, the Applied Optics Group (AOG) at the University of Nottingham has been developing CHeap Optical Transducer (CHOT) technology. These devices are activated by lasers and can generate and detect ultrasound with the generation-CHOT (g-CHOT) and detection-CHOT (d-CHOT), respectively. The advantage of a CHOT-nonlinear system was that the optical setup could simplified. CHOTs were applied to the nonlinear experiment and the results are presented in Chapter 5. Finally, Chapter 6 will summarise the work, discuss improvements, limitations and possible improvements, and describe the future of the experiment for NDT applications.

1.2 The need for NDT

Nondestructive testing (NDT) is the process through which material is tested for abnormalities and defects without causing any damage to it i.e. to evaluate an object's integrity without changing it in any way. This process may also be referred to as nondestructive inspection (NDI) or nondestructive evaluation (NDE).

NDT is essential in many industrial sectors such as the aerospace, nuclear, and pipeline industries. Ultimately, the motivation behind NDT is to provide reliable products by minimising the risk of failure thereby reducing costs and maximising safety. NDT is used to characterise materials, monitor manufacturing processes and detect defects.

Defects are caused by many manufacturing processes such as melting, grinding, welding and joining. It is important that NDT is applied at various stages of manufacture to demonstrate that a component continues to meet a specific standard and that the material has not been weakened by the manufacturing processes.

The application of NDT during component testing provides useful information about the presence and growth of defects, which can then be used to make ‘life-time’ predictions. Once in service, factors such as over-loading the component, fatigue and corrosion can cause further defects and, therefore, ‘in-service’ inspection is vital so that components can be repaired or replaced, if necessary.

The down-time required for this kind of inspection is usually minimised to reduce costs and particularly for the aerospace industry, often leads to ‘on-wing’ inspection. Developing NDT techniques that can be performed quickly, efficiently and in difficult to reach places is challenging but has obvious benefits.

In the aerospace industry, there is momentum towards lighter and more efficient engines, driven by attempts to reduce the cost of flying. To reduce weight, new materials such as carbon composites and metal matrix composites (MMCs) are being developed. Before they can be put into service, it is essential that the risks involved are managed − NDT forms an essential part of managing these risks.

With the introduction of new materials comes the potential requirement for new NDT techniques. In addition, there is a demand for inspection methods that can provide earlier indications of material failure than present techniques and, thus, provides a strong rationale for the work presented in this thesis.

1.3 NDT techniques currently used in industry

The most widely used NDT methods in industry include visual inspection, penetrant testing, magnetic particle inspection (MPI), eddy current inspection (ECT), radiography and ultrasound. Selection of the most appropriate method is based on the material type, defect size and location, and accessibility.

Visual inspection involves chemically etching or electro-chemically etching the component, so that the surface condition can be examined. Variations in grain size, inclusions, grinding abuse, cracks and folds can be identified using this method. Although it is a simple and fairly rapid method, it is limited only to surface inspection.

Liquid penetrant testing (LPI) involves coating the component with a liquid penetrant, which will enter into any surface cracks. Subsequently, excess penetrant is removed and a developer is applied. The developer ‘draws’ out the penetrant that remains in the crack making it visible. Although this is an inexpensive and simple method it is relatively slow and limited to non-porus materials.

MPI is limited to surface inspection of ferromagnetic materials. It is based on detecting changes in the magnetic permeability of ferromagnetic materials, due to the presence of flaws. However, it is only sensitive to flaws that are transverse to the magnetic field being applied to the material.

ECT inspection is limited to inspecting cracks near the surface of conductive samples. It is unable to examine large-areas but it is still very popular in industry because it is portable and provides immediate test results.

Inspecting with radiography consists of using X-rays to penetrate the surface of the sample. The radiation emerging from the opposite side of the material can then be detected and used to determine the location and presence of flaws inside the sample. It can be applied to all materials with any surface condition and no couplant is required. However, it is expensive and requires access to the opposite side of the object under investigation, which is not always possible or straight-forward.

1.4 Ultrasound

The role of ultrasonics within the NDT community has increased dramatically over the last 30 years. At present, industrial ultrasonic inspection techniques use contact transducers for through-transmission and pulse-echo measurements, but there is a potential for further ultrasonic methods to be exploited, such as non-contact and nonlinear techniques.

Sounds that have a frequency above the audible human range (20Hz$-$20kHz) are termed ultrasonic. Ultrasound is useful because it allows media to be non-invasively inspected. Many people are familiar with its application to the medical industry and its ability to ‘see’ inside the human body. The fact that it provides information about the inside of an object makes it a very important technique, suitable for a wide range of applications.

When applied to NDT, the ultrasonic wave frequency and mode is selected depending on factors, such as material type, geometry, defect size, shape, orientation and location. The following sections briefly describe the most commonly used wave modes that are used for ultrasonic inspection.

1.4.1 Bulk waves

In an isotropic solid, there are two distinct bulk wave modes – the longitudinal and transverse modes. The longitudinal wave mode causes the particles in the solid to vibrate parallel to the direction of wave propagation. Waves that have this form of vibration can also be called compressional, pressure or density waves. The other is the transverse or shear mode, which causes the particles to oscillate at right angles to the direction of wave propagation. Figure 1.1 compares the particle movement for the two modes.

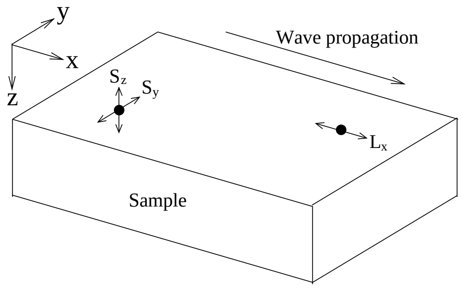

Figure 1.1: Particle displacement for the propagating longitudinal (L) and shear (S) modes. Particle L has motion in the x direction, while particle S experiences motion in the y and z directions.

Bulk waves are used to detect defects located within the material and are often generated and detected using contact transducers (see section 1.5.1). The probability of detection (POD) is increased by using a number of transducers, which excite bulk waves at different angles. This is because the reflected (or transmitted) sound depends on the orientation of the defect with respect to the propagating ultrasound.

1.4.2 Rayleigh waves

The use of ultrasound to detect the presence of defects is not limited to the interior of materials. Defects located on or near the surface of materials are more effectively detected using surface waves than bulk waves. This is because the minimum distance between the defect and the surface is related to the pulse duration of the transducer.

The type of surface wave that is of interest to the NDT community is the Rayleigh wave [6]. The penetration depth of Rayleigh waves is approximately equal to their wavelength, which makes them suitable for inspecting the near-surface of materials. During the 1950s, investigators began using Rayleigh waves for material inspection in the laboratory [7, 8]. Following these early investigators, Rayleigh wave 'visualisation' techniques based on optical scanning detection systems were successfully developed [9, 10].

In an isotropic medium, a Rayleigh wave has both longitudinal and shear contributions [3], which have a 90° phase difference that produces an elliptical particle motion. At a depth of 0.2λ the longitudinal component disappears and changes sign, leaving only the transverse motion. Deeper still, the motion becomes elliptical again but in the opposite direction. The particle displacement disappears at a depth of 2λ. This is shown in figure 1.2.

Rayleigh waves have been used extensively for NDT purposes e.g. detecting surface-breaking fatigue cracks [11, 12], measuring stress [13, 14, 5, 15, 16], assessing surface roughness [17, 18] and imaging surface features [19, 20].

For the purposes of this work, it is important to establish the degree of stress that is applied to the sample by the low frequency (pump) Rayleigh wave. Working

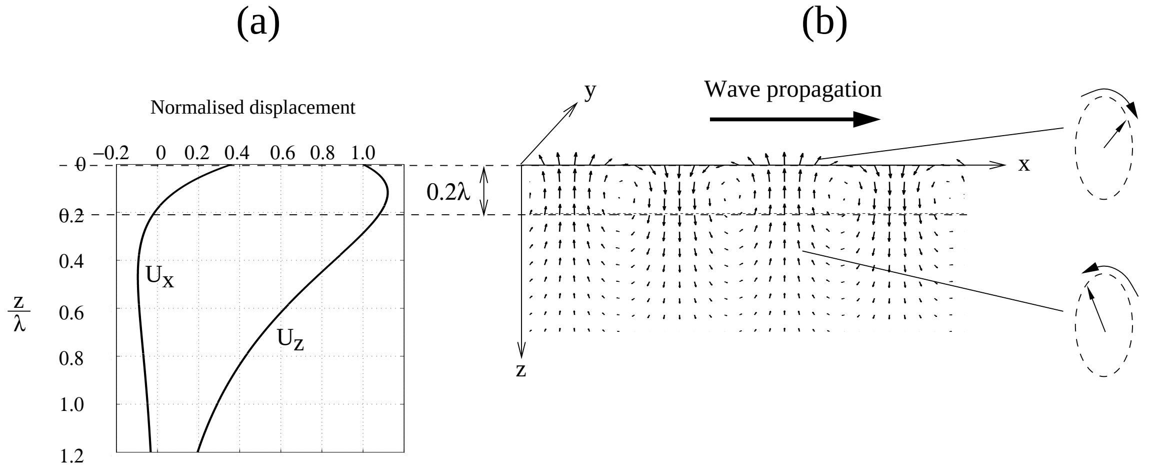

Figure 1.2: Normalised displacements (U_x and U_z) in the x and z directions (a). Particle motion caused by a propagating Rayleigh wave in the positive x direction (b). Both (a) and (b) were produced by the author using the theory explained in the latter part of this section.

from [3], the particle displacements along the x and z axes of figure 1.2 are written as follows:

$$U_x = \frac{\partial \varphi}{\partial x} - \frac{\partial \psi}{\partial z} \tag{1.1}$$

$$U_z = \frac{\partial \varphi}{\partial z} + \frac{\partial \psi}{\partial x} \tag{1.2}$$

where φ and ψ are the scalar and vector potentials of the displacements given below:

$$\varphi = Ae^{-qz}e^{i(kx-\omega t)} \tag{1.3}$$

$$\psi = Be^{-sz}e^{i(kx-\omega t)} \tag{1.4}$$

where A and B are arbitrary constants, k is the wave number, ω is the angular frequency, and where q and s can be written as:

$$q^2 = k^2 - k_l^2 \tag{1.5}$$

$$s^2 = k^2 - k_t^2 \tag{1.6}$$

in which k_l and k_t are the wave numbers for the longitudinal and transverse modes, respectively, and are given below:

$$k_l = \omega\sqrt{\frac{\rho}{\lambda + 2\mu}} \tag{1.7}$$

$$k_t = \omega\sqrt{\frac{\rho}{\mu}} \tag{1.8}$$

where λ and μ are the bulk and shear moduli, respectively, and ρ is the medium density. The stress components (σ_{xx}, σ_{zz} and σ_{xz}) are also given as:

$$\sigma_{xx} = \lambda(\frac{\partial^2\varphi}{\partial x^2} + \frac{\partial^2\varphi}{\partial z^2}) + 2\mu(\frac{\partial^2\varphi}{\partial x^2} + \frac{\partial^2\psi}{\partial x\partial z}) \tag{1.9}$$

$$\sigma_{zz} = \lambda(\frac{\partial^2\varphi}{\partial x^2} + \frac{\partial^2\varphi}{\partial z^2}) + 2\mu(\frac{\partial^2\varphi}{\partial z^2} + \frac{\partial^2\psi}{\partial x\partial z}) \tag{1.10}$$

$$\sigma_{xz} = \mu(2\frac{\partial^2\varphi}{\partial x\partial z} + \frac{\partial^2\psi}{\partial x^2} - \frac{\partial^2\psi}{\partial z^2}) \tag{1.11}$$

By substituting equations 1.3 and 1.4 into 1.11 (for example), it is possible to obtain an expression for B in terms of A as follows:

$$B = -\frac{2Aqik}{k^2 + s^2} \tag{1.12}$$

Also, by using 1.6 with 1.8 and 1.5 with 1.7, an expression for μ and λ, respectively, is obtained:

$$\mu = \frac{\omega^2 \rho}{k^2 - s^2} \tag{1.13}$$

$$\lambda = \frac{\omega^2 \rho((k^2 - s^2) - 2(k^2 - q^2))}{(k^2 - q^2)(k^2 - s^2)} \tag{1.14}$$

By using equations 1.1, 1.2 and 1.12 and taking the real part only, the equations for the displacements are as follows:

$$U_x = -Ak(e^{-qz} - \frac{2qs}{k^2 + s^2} e^{-sz}) sin(kx - \omega t) \tag{1.15}$$

$$U_z = -Aq(e^{-qz} + \frac{2k^2}{k^2 + s^2} e^{-sz}) cos(kx - \omega t) \tag{1.16}$$

By substituting 1.12, 2.4 and 1.14 into 1.9, 1.10 and 1.11, respectively, similar expressions are obtained for the stress components, taking the real parts only:

$$\sigma_{xx} = (\lambda A e^{-qz}(q^2 - k^2) - 2\mu A k^2 (e^{qz} - \frac{2qs}{k^2 + s^2} e^{-sz})) cos(kx - wt) \tag{1.17}$$

$$\sigma_{zz} = (\lambda A e^{-qz}(q^2 - k^2) + 2\mu A q (q e^{-qz} - \frac{2k^2 s}{k^2 + s^2} e^{-sz})) cos(kx - wt) \tag{1.18}$$

$$\sigma_{xz} = -2\mu A q k (e^{-sz} - e^{-qz}) sin(kx - wt) \tag{1.19}$$

Using equations 1.17, 1.18 and 1.19, the stresses in a particular material caused by a Rayleigh wave can be determined.

Figure 1.3 shows the normalised stresses. At the surface of the sample, the σ_{zz} and σ_{xz} components disappear leaving σ_{xx}. For example, if a 1MHz pump SAW

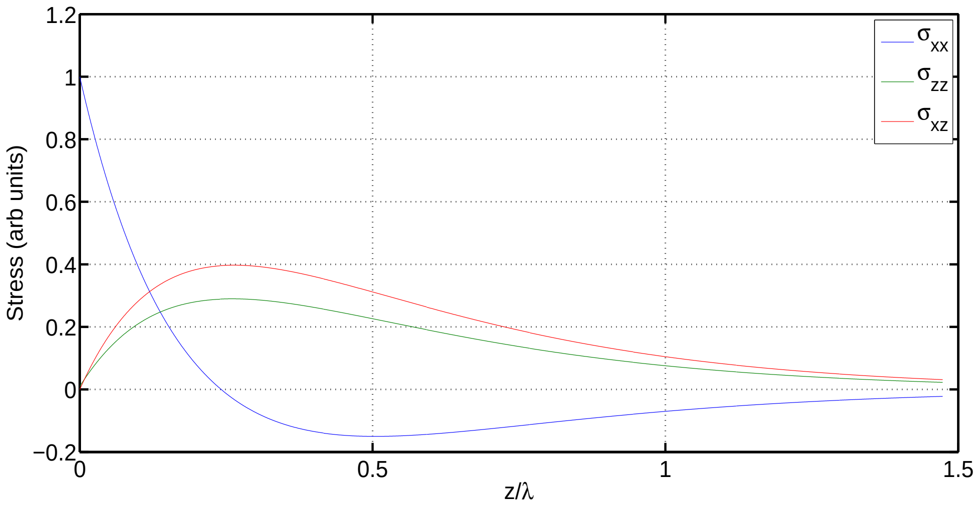

Figure 1.3: Rayleigh wave stress components. Here, the data are normalised, whereas in Chapter 5, the same theory was used to ascertain the actual applied stress on fused silica and aluminium samples using the material properties presented in Appendix A.

propagates in a material that has a velocity of 3000m/s, the acoustic wavelength (λ_{LF}) of the SAW is 3mm. A propagating 82MHz probe SAW in the same material has a wavelength (λ_{HF}) of 36μm. Since $\lambda_{HF} \ll \lambda_{LF}$, it can be assumed that the probe SAW experiences the stress components at the surface of the sample, i.e. σ_{xx}.

From figure 1.2(b), we can see that the longitudinal stress component (σ_{xx}) causes the particles at the peak and trough of the Rayleigh wave to be 'pulled' apart and 'squeezed' together, respectively. The material is, therefore, experiencing a tensional stress ($+\sigma_{xx}$) at the peak and a compressional stress (-σ_{xx}) at the trough.

In the elastic region of a 'linear' material, the relationship between stress and strain is constant, which means that the ultrasonic velocity at $+\sigma_{xx}$ and -σ_{xx} would be equal. This is only an approximation because, in a realistic (i.e. 'non-Hookean' or 'nonlinear') material the stress-strain relationship is nonlinear. In this case, the induced stress alters the elastic constants of the material, causing subtle changes in its properties, which can be measured by a change in ultrasonic velocity. How ultrasonic velocity is affected by applied stress depends on the material type.

1.4.3 Lamb waves

Lamb waves are useful for NDT techniques because they have the potential to propagate over considerable distances and, therefore, can be used to inspect large structures [21]. Research into their interaction with notches [22], delaminations [23] and cracks [24, 25] has been performed. Non-contact methods of generating and detecting Lamb waves have been previously studied [26, 27].

A Lamb wave travels through the entire thickness of a material, meaning that both the surfaces and the bulk of the material are interrogated [28]. There are a number of possible Lamb wave modes, which are often presented in phase (or group) velocity-dispersion curves. However, two modes that are commonly used are the symmetrical (S_0) and asymmetrical (A_0) modes. The shapes of these modes are shown schematically in figure 1.4.

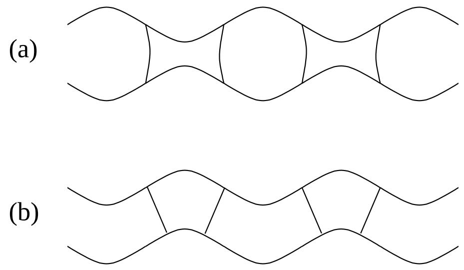

Figure 1.4: Schematic diagram of the A_0 (a) and S_0 (b) modes that are commonly used in NDT.

In this thesis, the nonlinear experiment was performed on samples that had a thickness greater than the wavelength of the pump SAW (i.e. with Rayleigh waves). However, it is also feasible that this experiment will be applied equally well to relatively thin samples. If the sample thickness is lower than the wavelength of the pump SAW, then Lamb waves will be excited into the sample. The advantage of using Lamb waves to stress the surface of the sample is that their point of generation could potentially be metres away from the point of nonlinear inspection, providing greater experimental flexibility for difficult to reach areas, for example.

1.5 Ultrasound generation and detection using contact devices

Alternative methods exist for generating SAWs other than using a transducer, and will be reviewed in this section. The advantages and disadvantages of each device will be discussed.

1.5.1 Transducers

Transducers are a very common method of generating and detecting ultrasound. They can be used to generate and detect bulk waves or, when attached to a wedge, excite and detect SAWs.

The active element is made of a piezoelectric or ferroelectric material that when excited by a time-varying voltage will expand and contract with the applied voltage. Conversely, if the element is made to expand and contract due to an applied force, a time-varying voltage output will be generated. A transducer can, therefore, be used to generate and detect ultrasound.

Transducers are commonly used in two modes of operation: transmit-reflection (pulse echo) and through-transmission, shown in figure 1.5a and 1.5b respectively.

In transmit-reflection mode, a single transducer is used to excite a bulk wave into the material. Defects present within the bulk of the material will reflect the sound back to the source, which the transducer will convert back into a voltage signal. The time of arrival indicates where the defect is in relation to the sample surface.

Through-transmission requires two transducers – one for generation and the other for detection. A defect will prevent the wave from propagating through the material and, therefore, the receiving transducer will not detect the wave.

When used to generate surface waves, the wedge that couples the ultrasound between the transducer and the sample has to be angled appropriately. The wedge

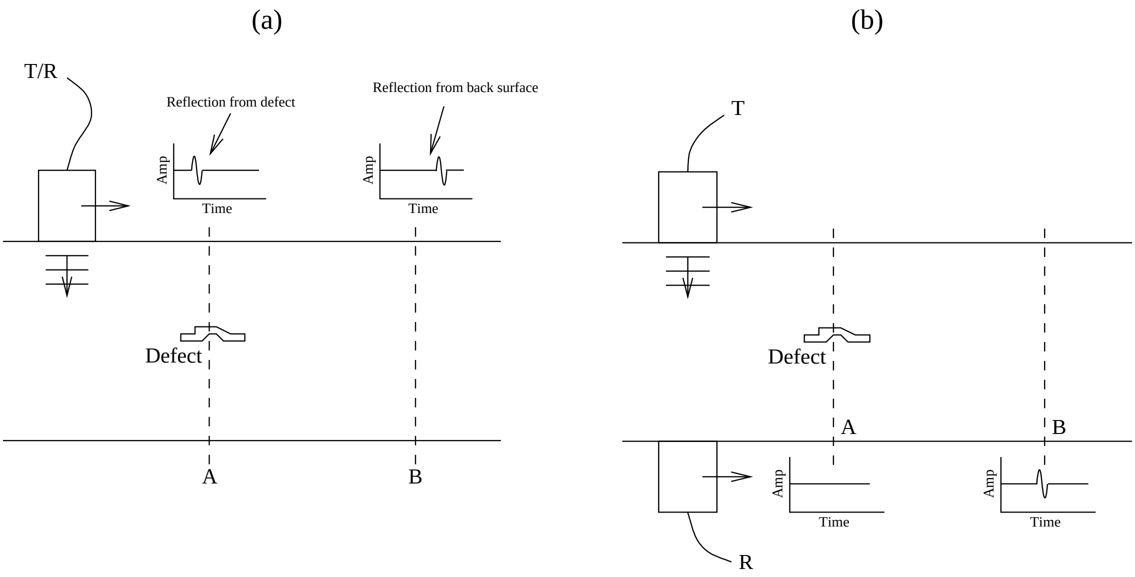

Figure 1.5: The use of transducers for transmit-reflection (a) and through-transmission (b) to locate a defect.

angle depends on the ratio of ultrasound velocity in the wedge material to that of the sample material. They are related by Snell's law, as shown in equation 1.20.

$$\frac{sin\theta_i}{v_i} = \frac{sin\theta_r}{v_r} \tag{1.20}$$

Where θ_i is the incident angle and θ_r is the angle of refraction from the normal, as shown in figure 1.6 (to generate a SAW, θ_r=90°). v_i and v_r are the ultrasound velocities in the wedge and sample materials, respectively.

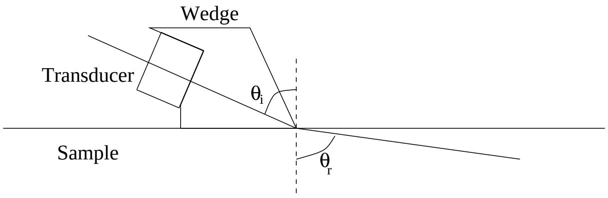

Figure 1.6: A wedge is used to angle the transducer so that a SAW can be generated on the surface of the sample.

Polystyrene is the preferred material for transducer wedges because it has a very low attenuation coefficient (∼0.18dB/mm at 5MHz) [29]. In comparison, PVC has a higher attenuation factor of 1.12dB/mm at 5MHz [29]. The shape of the wedge is also an important consideration. It has to be designed so that the emitted sound beam from the transducer is not reflected around the wedge which would otherwise cause spurious signals.

Attachment of the transducer to the wedge or sample can be achieved in a number of ways. Liquid couplant such as water or oil can be used as a temporary measure, but over a period of time, this type of couplant dries out. The alternative is to use a dry couplant, which bonds the two surfaces together. Phenyl salicylate forms a solid bond at room temperature but when heated to ∼36 °C, melts and the bond is broken. Once Phenyl salicylate is attached, the measurements are much more reproducible compared with a liquid-based couplant.

1.5.2 EMATs

Electromagnetic acoustic transducers (EMATs) [30, 31] can be used to generate and detect ultrasound in conductive or magnetic materials. EMATs operate without requiring couplant or contact, which makes it possible for them to work on moving objects and on oily or rough surfaces − their standoff distance is very low (<2mm).

An EMAT consists of a coil and a magnet, which can be configured in several different ways, depending on the wave mode that is to be excited/ detected. The principle behind their operation is often discussed in terms of a single wire placed in the vicinity of a metal surface. When a changing current flows through the wire, eddy currents are induced in the metal. In the presence of a static magnetic field, the eddy currents will experience a Lorentz force. If the current is driven at an ultrasonic frequency, an ultrasonic wave is excited into the metal sample. Figure 1.7 shows a cross-section of an EMAT, which can generate and detect Rayleigh waves [32].

EMATs have been used alongside laser generation systems to observe the interaction of Rayleigh waves with surface features on aluminium [33] and to accurately

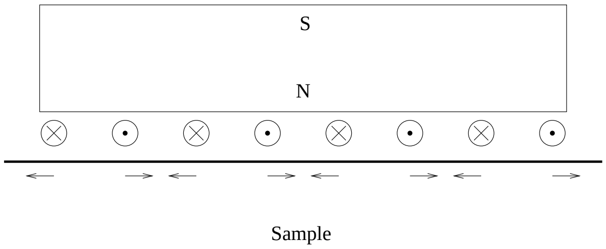

Figure 1.7: Cross-section of an EMAT configuration used to generate and detect Rayleigh waves. A ‘meandering’ wire is placed under a magnet and the motion of the coil (indicated by the arrows) induces an ultrasonic wave into the sample.

monitor the thickness of an aluminium plate [31, 34].

1.5.3 SAW devices

A section on SAW devices has been included in this chapter because they are analogous to CHOTs (see sections 1.6.2 and 1.7.3). Conceptually, SAW devices and CHOTs are very similar. However, the fundamental difference is that CHOTs are optically activated, giving them the advantage of being non-contact; in contrast, SAW devices have to be physically connected to external electronics.

Figure 1.8 shows the structure of a SAW device [35]. It consists of two interleaved sets of ‘fingers’ which are spaced to match the acoustic wavelength of the ultrasound to be generated. The fingers are metal electrodes that have been deposited on a piezoelectric substrate such as quartz. By applying an alternating voltage across the two sets of fingers, at an appropriate frequency, the surface of the piezoelectric material expands and contracts accordingly. This gives rise to a generated SAW on the surface of the attached sample. The SAW can be detected by a similar device commonly operating between a 10MHz−1GHz frequency range.

1.5.4 Comb transducers

A comb transducer (sometimes referred to as the Sokolinskii comb device) uses a specifically designed wedge, consisting of a comb-like structure, to excite SAWs

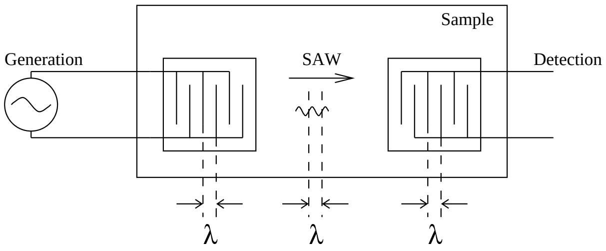

Figure 1.8: A SAW device is placed onto the surface of a sample and is used to generate and detect SAWs at a frequency determined by the finger separation.

onto a sample [3]. The teeth of the comb are periodically separated by a distance equivalent to the acoustic wavelength of the SAW to be generated. Figure 1.9 shows the structure of the device that is bonded to the sample. A transducer is placed on the upper surface of the wedge for activation of the ultrasound. Comb transducers have been used to excite Rayleigh waves on aluminium samples for nonlinear experiments [36].

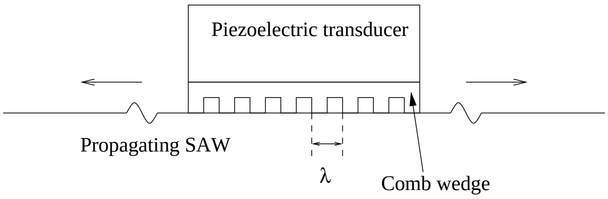

Figure 1.9: Structure of a comb transducer. In this case a SAW propagates in both directions. If a series of arcs is machined into the wedge, the SAW will propagate in a particular direction.

1.6 Generating ultrasound with lasers

Except for EMATs, all the techniques discussed in previous sections have a disadvantage in that they are all contact methods. The disadvantage with contact techniques is that they require couplant, which can dry out and become less effective over time. Contact devices load the sample surface and, therefore, influence the propagation of ultrasound.

The advantage with using lasers over the devices described in section 1.5 is that they are non-contact, allowing them to operate remotely, on moving objects, at extreme temperatures and in isolated or hazardous environments. In addition, the optical beams can be steered by mirrors into less accessible places.

Two regimes in which laser generated ultrasound can be considered important are thermoelastic and ablation regimes. Figure 1.10 shows the mechanisms by which ultrasound is generated in each regime. The fundamental difference between the two is the level of incident beam power density and the properties of the material itself. If the laser pulse energy incident on the surface of the sample is at a sufficiently low power density to prevent ablation, ($<10^5$ Wmm^{-2} for aluminium [32]), then ultrasound is generated in the thermoelastic regime. The area of the sample that is illuminated by the laser experiences an increase in temperature causing local thermal expansion. The time over which this occurs is comparable to the rise time of the incident laser pulse. The expansion generates stress in the material, generating bulk and surface acoustic waves that propagate away from the area.

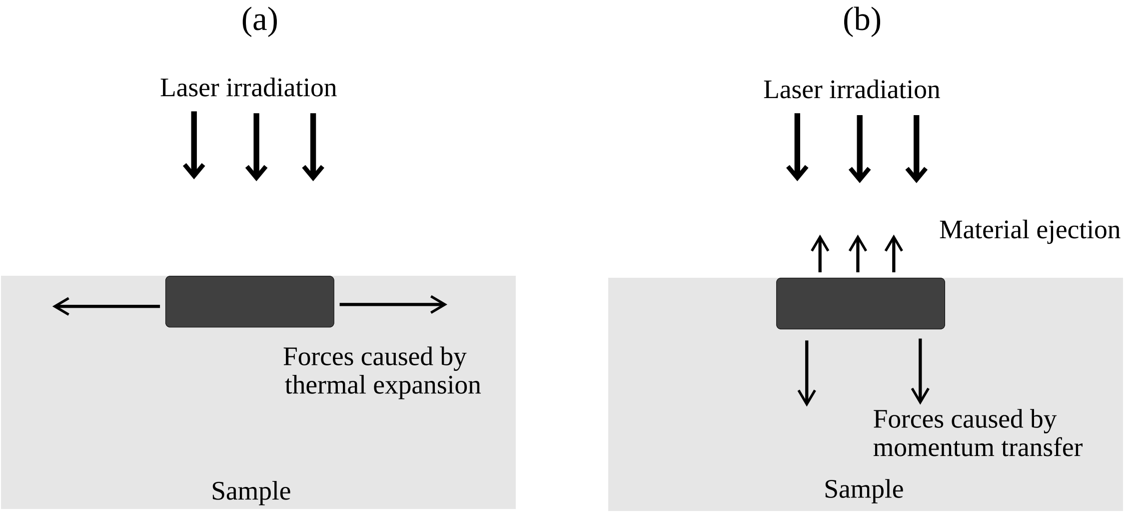

Figure 1.10: Schematic of the thermoelastic (a) and ablation (b) regimes for the generation of ultrasound using a laser.

In the ablation regime, the incident laser pulse power density is relatively high and causes the sample surface to be damaged immediately. The matter that is ejected outwards from the region of illumination places pressure on the locally surrounding material, exerting stresses and generating both bulk and surface waves in the material.

1.6.1 Review of laser generation techniques

Generating ultrasound using lasers can be achieved using several techniques that differ in complexity (figure 1.11).

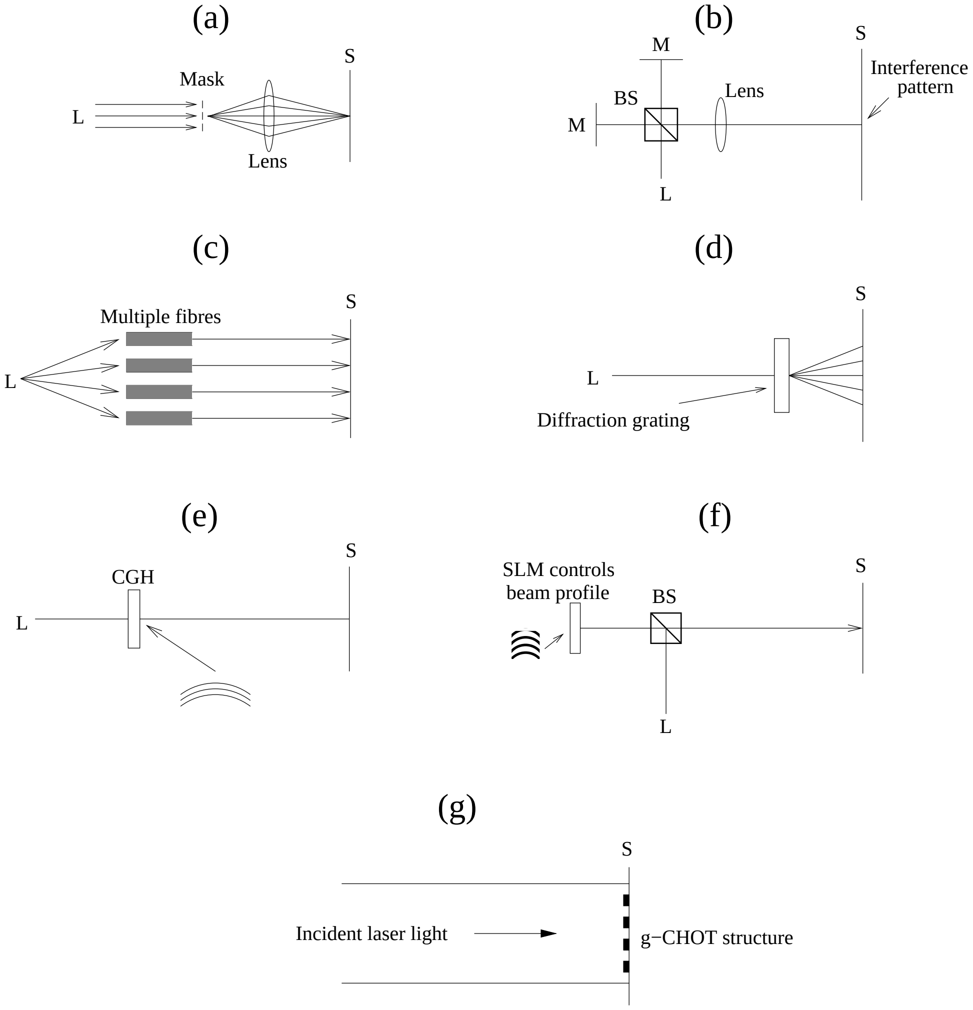

Figure 1.11: Laser generation of ultrasound with a mask (a), interferometry (b), multiple fibres (c), diffraction grating (d), computer generated hologram (e), SLM (f), and g-CHOT (g). L=laser source, S=sample, BS=beamsplitter, M=mirror.

The less complex methods involve focusing the laser beam to a point [37] or a line [38] and often this results in sample damage. To prevent damage, a number of techniques can be used and are now discussed.

By imaging a number of lines onto the sample, for example, a SAW can be generated at a desired frequency. The principle is similar to that of the comb transducer and the SAW devices described in sections 1.5.4 and 1.5.3, respectively, in that the line spacing is chosen to match the acoustic wavelength of ultrasound to be generated. The amplitude of the SAW is dependent upon the contrast in absorbed energy between the illuminated and non-illuminated regions of the sample.

A mask can be placed between the laser source and the sample (figure 1.11(a)), which partially blocks the laser beam so that the incident light is tailored. A different approach is to use interferometry [39] (figure 1.11(b)), where the constructive and destructive interference of two coherent laser beams produces light and dark regions on the sample surface. An array of optical fibres (figure 1.11(c)) directs the light onto the sample surface and the distance between lines is adjusted by simply altering the separation of the fibres [40]. Diffraction gratings (figure 1.11(d)) placed between the laser and sample distribute the laser beam over several discrete regions of the sample [41]. Another alternative is a computer generated hologram (CGH) (figure 1.11(e)) [42]. Here, the laser beam is manipulated so that a single arc or a series of arcs illuminate the surface of the sample, which focuses the SAWs to a point. The disadvantage of these devices is that they are inflexible and difficult to fabricate. The most adaptable device is the spatial light modulator (SLM) (figure 1.11(f)) [43]. This is computer controlled and can manipulate the beam so that the intensity of light is distributed over the sample to form a number of lines or arcs. Section 3.2.4 discusses how the SLM has been integrated into the OSAM system.

The development of the CHOT (figure 1.11(g)) has introduced a further technique that uses lasers to generate and detect ultrasound [44]. CHOTs are an innovative ultrasonic transducer system that are optically activated by a laser beam. There are two kinds of CHOTs: the g-CHOT and the d-CHOT. Although both can work independently of each other, a coupled CHOT system provides a powerful, robust, sensitive and remotely operated technique.

1.6.2 The g-CHOT

The g-CHOT is a structure deposited onto the sample surface. The geometrical characteristics of the structure control the generated wave mode, direction and wavelength. The principle behind the making of the g-CHOT was to create an ultrasonic source with an appropriately high contrast between absorbing and non-absorbing regions of the irradiated sample. An example of a g-CHOT structure for the generation of SAWs is shown in figure 1.12.

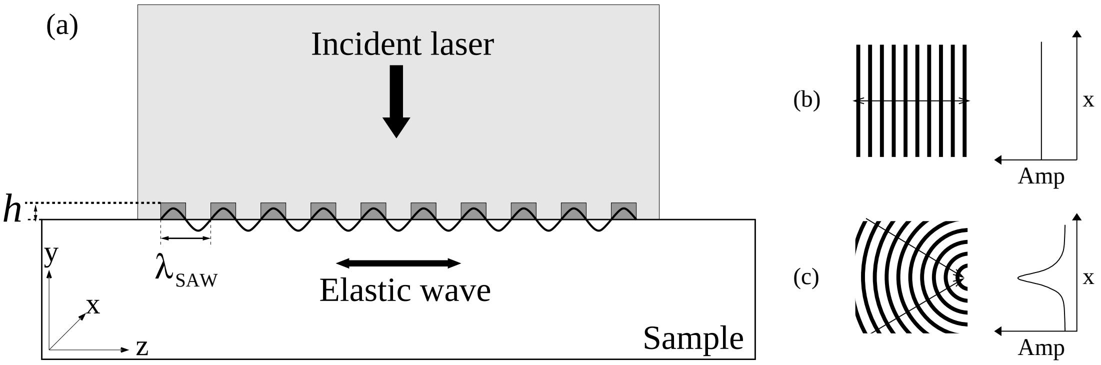

Figure 1.12: Basic g-CHOT cross section showing the structure required for SAW generation (a). Incident laser light illuminates a series of titanium lines separated by one acoustic wavelength λ_{SAW}. g-CHOT profiles can be fabricated as a series of lines (b) and arcs (c) that generate plane and focused ultrasound.

The profile of the CHOT lines can be altered to control the direction of the wave propagation. For example, by having a pattern with straight parallel lines, the resulting SAWs will have a plane wavefront that would propagate from both ends of the CHOT. The advantage of using an arc profile is that the ultrasound is focused to a single point, improving the signal-to-noise-ratio (SNR) for point detection. In this way the g-CHOT controls the directivity of the generated waves.

The incident radiation has to be pulsed since, otherwise a static thermal equilibrium would be reached between the absorbing and non-absorbing regions of the sample and in this condition, a SAW would not be excited. The pulsed laser light could be considered to be analogous to the alternating current that was applied across the two electrodes of a SAW device as described in section 1.5.3. The advantage of using light as the actuator, as opposed to an alternating current (AC) voltage, is that no physical connection exists between transducer and actuator. Therefore, using a laser offers a completely remotely operated and non-contact system for generating ultrasound.

1.7 Detecting ultrasound with lasers

There are several laser detection techniques which can be broadly classified as either interferometric and non-interferometric methods [45, 46, 39]. A disadvantage of optical detection techniques compared with contacting transducers is that they are relatively insensitive [47]. Another disadvantage of laser detection is that if the sample surface is rough, the reflected beam is scattered. Possible solution to this problem include the use of a Fabry-Pérot interferometer [45, 48, 49], or a photo-emf detector [50]. This section describes the knife-edge and interferometry techniques used to detect ultrasound.

1.7.1 Knife-edge detection

The knife-edge detector, also referred to as the optical beam deflection technique, [51, 52] can have several configurations (figure 1.13) [51].

The incident laser beam is focused onto the surface of the sample by a lens, and the reflected beam is focused onto a single photodetector. In this case, a knife-edge is placed over half of the reflected beam and a single photodiode converts the detected light into a voltage signal. A propagating SAW causes the surface gradient to change, which will deflect the reflected beam to a different position and alter the

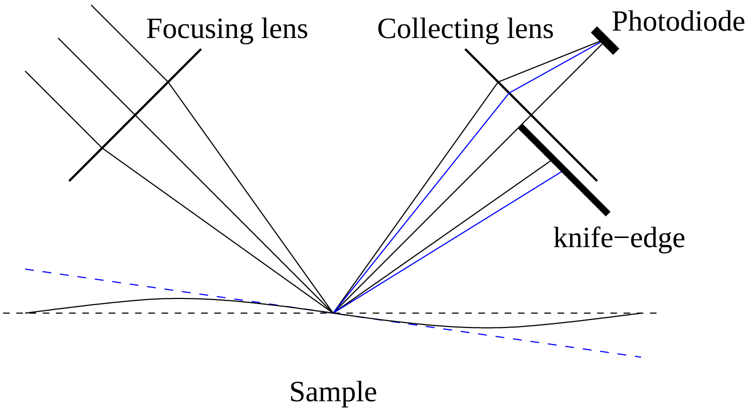

Figure 1.13: The knife edge detector. A propagating SAW causes the reflected beam to be shifted causing the light intensity, measured by the photodiode, to be modulated.

intensity of light being focused onto the detector. The surface of the sample needs to have a polished finish so that light scatter is minimised, and light incident on the photodiode is maximised.

For the work in this thesis, an alternative knife-edge detector arrangement was used (see section 3.3). Here, a differential detection technique is employed in which the knife-edge is replaced by a second photodiode. The advantage with the differential method is that the common-mode noise (due to intensity fluctuations of the probe beam) is reduced.

1.7.2 Interferometry

A common interferometer configuration is the Michelson interferometer [53, 54], which is shown in figure 1.14.

The light emitted from the laser is divided into two beams. One of these beams is incident on a reference mirror, which is held in a fixed position. The other beam is incident on the surface of the sample. Both beams are reflected off their respective elements and recombine at the beamsplitter, where they interfere either constructively or destructively. The recombined beam is incident onto a detector, which measures the intensity of the beam. Any change in path length brought on by the

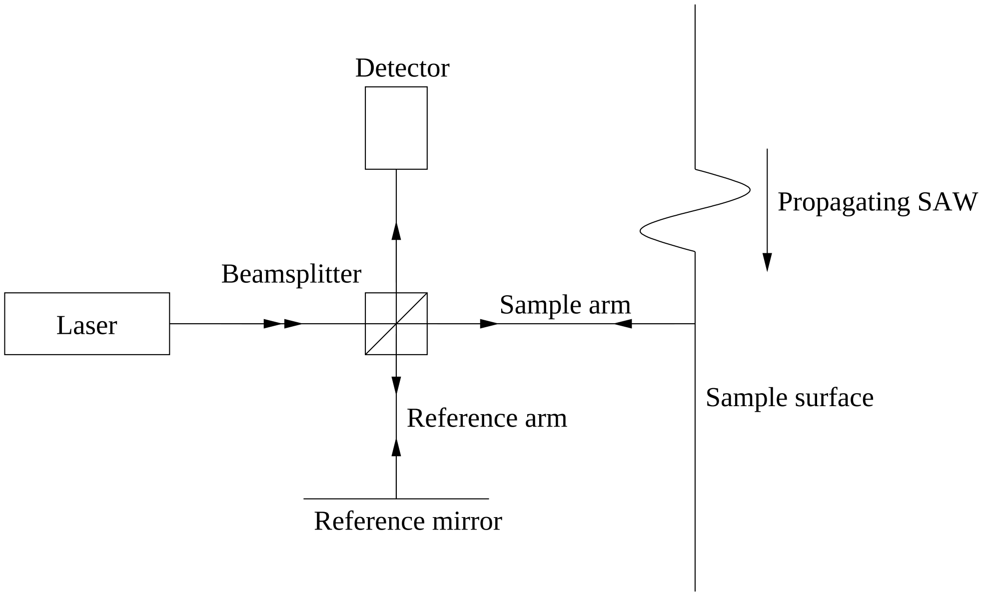

Figure 1.14: Detection of ultrasound using a Michelson interferometer. By placing a frequency shifter in either the reference or signal arms, it becomes a heterodyne interferometer.

presence of a SAW under the probe beam, produces an amplitude change measured by the detector.

This interferometer is very sensitive to vibrations and to compensate for this, an 'active feedback system' can be incorporated [39]. This involves attaching the reference mirror to a piezo-electric device, which can accurately adjust the position of the reference mirror to compensate for any variation in path length difference between the two arms caused by the background vibrations.

The alternative is to use a heterodyne interferometer [39]. In this configuration, the optical frequency in one arm is shifted by a radio frequency and the detector receives a signal at this shifted frequency, phase modulated by both the ultrasound and vibrations. The ultrasonic displacement can then be acquired independently of the vibration using a system of electronics.

1.7.3 The d-CHOT

Since the g-CHOT (section 1.6.2) generates narrowband ultrasound, it is favourable to have a matching narrowband detection system as well and this has led to the development of the d-CHOT. As with the g-CHOT, the d-CHOT consists of a structure placed onto the sample surface. However, as it reflects light, the d-CHOT can be considered a reflective grating. It is designed so that its geometrical features will select the desired mode and frequency. The basic d-CHOT structure for the detection of SAWs is shown in figure 1.15.

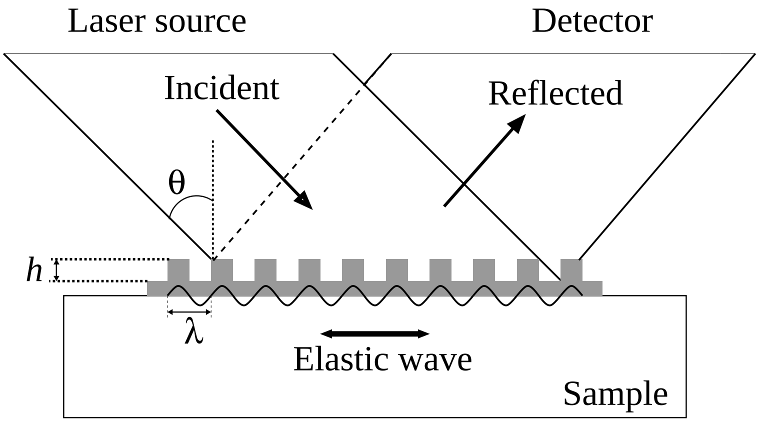

Figure 1.15: Cross-section of basic d-CHOT structure with appropriate height (h) and spacing (λ) to detect SAWs. As with the g-CHOT, the lines can be set for the detection of plane or focused waves.

The d-CHOT is activated by an incident continuous (CW) laser and the reflected beam is separated into a number of diffraction orders. The line spacing is chosen to ‘select’ or ‘match’ the acoustic wavelength of the waves that are to be detected. The height of the steps in the grating is designed in such a way as to introduce the desired path length difference in the incident light. The height of the steps is given by equation 1.21.

$$h = \frac{\lambda_{opt}}{8\cos(\theta)} \tag{1.21}$$

where h is the step height, λ_{opt} is the optical wavelength of the incident laser and θ

is the angle of incidence. In order for maximum sensitivity, the effective path length difference between the two beams is 1/4 of the wavelength of the incident laser light. For normal incident light, the path length difference is $2h$ meaning that h must be 1/8 of the optical wavelength. Each step of the d-CHOT can be considered to be a miniature common path interferometer. Figure 1.16 shows a schematic of the d-CHOT in which the 'signal' and 'reference' beams can be considered to be from the top and the bottom of the steps.

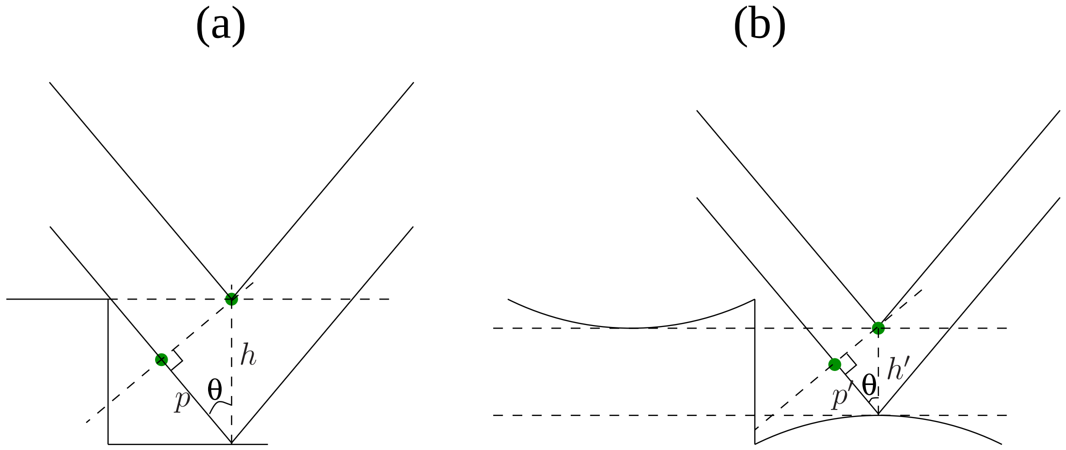

Figure 1.16: Schematic of d-CHOT without (a) and with (b) a propagating SAW. The height of the steps is changed by the elastic wave. The light energy contained with the reflected diffraction orders is modulated accordingly.

As the SAW propagates over the d-CHOT structure, the height of the steps changes and, therefore, the path length difference between the signal and reference beams changes from $2p$ to $2p'$ (figure 1.16(a) and 1.16(b) respectively). This causes the light energy contained within these orders to be modulated. One of the reflected diffraction orders (preferably the zero order, as this is the direct reflection) is selected by an iris and focused onto a single photodetector. The modulation of light energy between the orders is measured in the light intensity received by the detector.

1.8 Summary

The motivation behind this work is to develop a NDT method that can be applied to monitoring material fatigue. To achieve this, the first objective is to establish an experimental technique capable of measuring material nonlinearity. The second objective is to apply the technique to fatigued samples. The level of fatigue would cause the measured nonlinearity to change.

This thesis presents a laser-based ultrasonic experimental technique which aims to fulfil the first of these objectives. The experiment measures a change in ultrasonic velocity caused by an applied stress. The velocity-stress gradient is a direct measure of material nonlinearity and can, therefore, be used to monitor fatigue.

The work presented here is novel because the experiment was performed using SAWs which were generated and detected using lasers and therefore has the advantage of being non-contacting.

Chapter 2

Literature Review

2.1 Introduction

The purpose of this chapter is to provide a review of material elastic behaviour (section 2.2) and the nonlinear experimental techniques that are currently being used in NDT (section 2.3). A broad historical overview of nonlinear ultrasound can be found in [55] and [56].

Material nonlinearity manifests itself as acoustic-waveform distortion due to amplitude-dependent wave propagation, higher harmonics generation, velocity modulation and the inter-modulation of two independent propagating waves (sum and difference frequencies). Material nonlinearity is often quantified by the β-parameter, defined in section 2.3.1. The work in this thesis does not use β, instead the velocity-stress relationship is used to quantify material nonlinearity.

Fatigue is defined as the decline in mechanical properties encountered in a metal subjected to repeated cycles of stress [57]. Fatigue damage is a distributed phenomenon affecting the structure at many locations. Before the initiation of a terminal crack, small-scale micro-cracking occurs, which can be considered to be an even degradation of the material. These micro-cracks can be regarded as nuclei of the fracture process and since the nuclei are much smaller than the acoustic wavelength at the frequencies generally used for NDT, linear acoustic indications (e.g. changes in attenuation and velocity) have insufficient sensitivity to detect their presence. However, micro-cracks do give rise to excess material nonlinearity, which can be orders of magnitude higher than the intrinsic nonlinearity of an undamaged material.

A nonlinear ultrasonic technique locates fatigue by causing micro-cracks to open and close (referred to as 'clapping'). When a crack is forced to close, the local elastic modulus approaches that of a continuous (undamaged) material. As a crack is opened, the elastic modulus decreases. This parametric modulation in elastic modulus is caused by the stress dependence of the interfacial stiffness of the crack. In a fatigued material, the presence of local residual stresses cause cracks to be partially open and these contribute to the excess nonlinearity [58, 59, 60]. Material nonlinearity can be quantified by the β-parameter or by the velocity-stress gradient. The presence of fatigue, would therefore cause these parameters to change.

The nonlinear methods discussed in this chapter are subjects of research in the AERONEWS (health monitoring of aircraft by nonlinear elastic wave spectroscopy) project and Delsanto (2007) [61] provides a complete and recent publication on the application of these nonlinear experiments to non-destructive evaluation.

2.2 Linear elasticity

A material is said to be 'linear' if the relationship between stress and strain in the elastic region of the material is constant, i.e. a constant Young's modulus. In a homogeneous, isotropic and linear material, the relationship between stress (σ_{ij}) and strain (ϵ_{kl}) is given by Hooke's law, which states that the degree of strain is linearly related to the applied stress (equation 2.1):

$$\sigma_{ij} = C_{ijkl}\epsilon_{kl} \tag{2.1}$$

where C_{ijkl} is the second order elastic constants (or the 4th rank stiffness tensor), which has 81 components. Using a compressed (Voight) notation, the number of components can be reduced to 36 and these components can be shown in a 6×6 matrix (equation 2.2).

$$\begin{pmatrix} \sigma_{xx} \\ \sigma_{yy} \\ \sigma_{zz} \\ \sigma_{yz} \\ \sigma_{zx} \\ \sigma_{xy} \end{pmatrix} = \begin{pmatrix} C_{11} & C_{12} & C_{13} & C_{14} & C_{15} & C_{16} \\ C_{21} & C_{22} & C_{23} & C_{24} & C_{25} & C_{26} \\ C_{31} & C_{32} & C_{33} & C_{34} & C_{35} & C_{36} \\ C_{41} & C_{42} & C_{43} & C_{44} & C_{45} & C_{46} \\ C_{51} & C_{52} & C_{53} & C_{54} & C_{55} & C_{56} \\ C_{61} & C_{62} & C_{63} & C_{64} & C_{65} & C_{66} \end{pmatrix} \begin{pmatrix} \epsilon_{xx} \\ \epsilon_{yy} \\ \epsilon_{zz} \\ \epsilon_{yz} \\ \epsilon_{zx} \\ \epsilon_{xy} \end{pmatrix} \tag{2.2}$$

For an isotropic solid the stiffness tensor matrix can be simplified since $C_{xy} = C_{yx}$ (reducing the number of constants to 21). Also, the following relations are true:

$$C_{11} = C_{22} = C_{33} = \lambda + 2\mu \tag{2.3}$$

$$C_{44} = C_{55} = C_{66} = \mu \tag{2.4}$$

$$C_{12} = C_{13} = C_{21} = C_{23} = C_{31} = C_{32} = \lambda \tag{2.5}$$

where λ and μ are the Lamé constants (all other constants in the matrix are zero). The Lamé constants are known as the second order elastic constants, and together they can be used to completely describe the elastic behaviour of an isotropic solid. They are related to the Young's modulus (E), Poisson's ratio (ν) and bulk modulus (K) by equations 2.6, 2.7 and 2.8, respectively.

$$E = \frac{\mu(3\lambda + 2\mu)}{\lambda + \mu} \tag{2.6}$$

$$\nu = \frac{\lambda}{2(\lambda + \mu)} \tag{2.7}$$

$$K = \lambda + \frac{2}{3}\mu \tag{2.8}$$

In a solid, the relationship between sound velocity, v and the elastic constants is given by equation 2.9 [62].

$$v = \sqrt{\frac{C_{xy}}{\rho}} \tag{2.9}$$

where ρ is the material density. The shear velocity (v_s) and longitudinal velocity (v_l) are calculated by substituting C_{xy} with the shear (G) or longitudinal (L) moduli, respectively. G and L are given in equations 2.10 and 2.11, respectively [63]:

$$G = \frac{E}{2(1 + \nu)} \tag{2.10}$$

$$L = K + \frac{4}{3}G \tag{2.11}$$

A Rayleigh wave has both shear and longitudinal contributions, and the Rayleigh wave velocity (v_r) can be obtained using the Bergmann approximation [3]:

$$\frac{v_r}{v_s} = \frac{0.87 + 1.12\nu}{1 + \nu} \tag{2.12}$$

In the linear regime, the elastic constants (and, therefore, the ultrasonic velocity) are unaltered by applied stress, providing that all other variables such as temperature [64], remain constant. However, there have been numerous experiments that have disproved this. For example, when steel and silicon nitride samples were placed into a 4-point bending jig, it was found that the velocity of SAWs changed with stress [13]. For steel, the Rayleigh wave velocity was found to change by $-5.76\text{mms}^{-1}/\text{MPa}$

and for silicon nitride, a velocity change of approximately 52.6mms^{-1}/MPa was measured.

2.3 Nonlinear experimental techniques

There are numerous experimental techniques that are being used to measure material nonlinearity. The purpose of this section is to review these methods and discuss their advantages and disadvantages.

2.3.1 Higher harmonic generation – 'self-stressing' method

In a 'nonlinear material', a high amplitude wave experiences an accumulative increase in distortion (in addition to attenuation and diffraction) as it propagates [65]. The reason for this is because different parts of the wave propagate at different velocities. This type of wave can be considered as 'self-stressing', i.e. the velocity of the wave depends on the stress that it is imposing on the sample (figure 2.1 [65]).

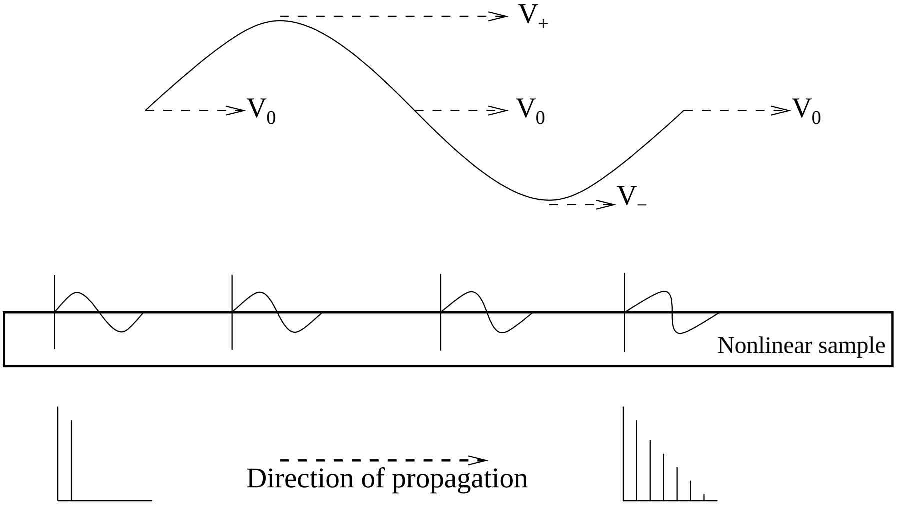

Figure 2.1: Propagation of a high amplitude ('self-stressing') wave in an elastic material. As the propagation distance increases, the wave profile becomes distorted. The harmonic content of the wave can be obtained to provide a measure of the material nonlinearity.

In figure 2.1 the peak and trough of the wave are propagating faster and slower respectively than the zero stress position, causing the wave to become distorted. The degree of distortion depends on the material type, the wave amplitude and how far the wave has propagated. In the case of an undamaged elastic material, this is a gradual effect. Contrastingly, in the presence of internal stresses, micro-fatigue cracks and damage, it can occur suddenly, since these significantly increase the nonlinear response of the material.

The wave distortion causes the frequency content of the wave to change because the acoustic energy is transferred from the fundamental frequency to its harmonics. This is different from the pump-probe method used in this thesis, in which the 'stressing' and 'velocity measuring' were performed by two independent waves.

By measuring the harmonic(s) amplitude relative to the fundamental, it is possible to obtain a measure of material nonlinearity. Equation 2.13 relates the ratio of the fundamental and second harmonic with this nonlinearity, in terms of the β-parameter.

$$\beta = (\frac{A_2}{A_1^2})\frac{8}{kd} \tag{2.13}$$

where A_1 and A_2 are the amplitudes of the fundamental and second harmonic components of the detected ultrasound, respectively, k is the propagation constant ($\frac{2\pi}{\lambda}$) and d is the distance over which the wave has propagated. The experimental principle is, therefore, to excite a wave in the sample at frequency f and detect at frequencies f and 2f. This is a very popular technique [66, 67, 68, 69, 70, 71, 72], and has been used to investigate the effect of dislocation density [73] using various detection techniques such as a capacitive transducer [74], optical probing [75] and Michelson interferometry [76, 77]. Recently, the harmonic generation technique has been performed with a Rayleigh wave [78].

The experiment performed by Blackshire *et al* aimed to detect the presence of a fracture in titanium samples [79]. A 5MHz bulk wave was generated and as the sound path approached a fracture, there was a 320% increase in the nonlinear parameter. A similar experiment was performed at various fatigued stages of a titanium alloy sample using a 20MHz fundamental frequency [80]. When the results from the nonlinear technique were compared with 'linear parameters', such as attenuation and velocity, the sensitivity of the nonlinear technique was found to be far greater.

The concern with this approach is that the experimental apparatus can introduce harmonics into the measurements. Therefore, it is important to separate the material nonlinearity from the apparatus nonlinearity if a reliable value for β is to be measured. The quality of the transducer-sample bonding may vary between experiments, making it difficult to obtain consistent measurements. For these reasons, the parametric interaction technique is preferred (section 2.3.2).

2.3.2 Parametric interaction

In a nonlinear material, a propagating wave is affected by the presence of a second wave or vibration. Material nonlinearity can be measured in terms of the inter-modulation of two signals, and the experimental techniques discussed in this section measure this inter-modulation as either:

1. A frequency modulation (sum and difference frequencies) of the two input signals.
2. A phase modulation of the higher frequency signal.

Frequency modulation

The low frequency (pump) signal can be an ultrasonic wave [81], a sinusoidal modulating vibration [82, 60] or an impact hammer or shaker [83, 84, 85].

The frequency modulation technique has been applied to cracked samples [86, 87], detecting contact interfaces [88, 89] and fatigue [83, 84]. The purpose of the modulating signal is to open and close the defect. This modulation of the defect means that the high frequency (probe) signal (generated by a transducer, for example) will become distorted as it propagates through the defect. The combined result of the pump and (distorted) probe waves generates side bands in the frequency spectrum. The modulation of the defect can be achieved using an incident laser source, which thermally expands and contracts the material around the crack [90].

Phase modulation

With this technique, the interaction between the pump and probe waves is measured in the phase of the probe wave. This can be considered as measuring changes in the 'time of flight' of the probe signal as it interacts with the pump wave.

The β-parameter of polystyrene, aluminium, titanium and fused silica was measured and compared using this method [2, 4]. Here, a 2.5MHz pump signal with a $\sim$0.8μs duration was mixed with a 20MHz probe signal with a duration of 2.5μs. With this setup, different parts of the probe signal were modulated by different degrees simultaneously by the pump. This experiment was performed using bulk waves.

In contrast, the phase modulation experiment developed in this thesis used SAWs. Here, the pump SAW packet was typically 3μs in duration (assuming a 3-cycle 1MHz signal) and the probe was approximately 0.8μs duration. Since the pump wave was considerably longer in duration than the probe signal, the degree of phase modulation experienced by the probe depended on which portion of the pump wave it interacted with. In order to see changes in the phase response of the probe signal, its point of interaction with the pump wave had to be altered. This was achieved by controlling the point in time at which the two SAWs were excited, i.e. by delaying the triggering time of the probe pulse with respect to the pump.

2.3.3 Nonlinear-time reversal acoustics (NL-TRA)

The time reversal (TR) technique can be applied to the harmonic generation and wave modulation techniques described above [91]. To describe how TR is implemented, this section will focus on its application to the harmonic generation technique.

A single emitting transducer generates ultrasound into the sample. This ultrasound is then detected at various locations around the sample using a number of detecting transducers and the signals that these detector transducers obtain are then time reversed. The detector transducers are then converted to emitters and what was the emitter transducer is now converted to a detector. The emitter transducers now generate their respective TR signals, which recombine with each other as they propagate back through the material. If the material is completely linear and damage-free, then there will be no harmonic content in any of the signals. Therefore, this recombined signal, which is the superposition of all these TR signals, will be detected by the detection transducer. However, if the sample is damaged and, therefore, has a higher nonlinearity content, then harmonics will have been generated. On sending back the TR signals in a damaged material, the harmonic contributions would recombine at the focus of their source, i.e. at the damaged region. Meanwhile, the fundamental components of the TR signals would recombine back at their source, i.e. at the detector transducer. A highpass filter could be applied to the TR signals ensuring that only the harmonic contributions would be sent back into the sample. By imaging the ultrasound on the sample surface with a laser detection system, for example, the area of damage can be located.

2.3.4 Nonlinear reverberation spectroscopy (NRS)

The aim of NRS is to identify the presence of damage in a component, rather than specifically locating the precise area of damage [92]. A sample is globally excited by a mono-frequency source at a constant amplitude for a known duration of time. A loud speaker, placed relatively near the sample, is used to generate a frequency close to the resonant frequency of the specimen. The duration over which this frequency is emitted has to be long enough for the sample to reach a steady state response. The transmitting sound is then stopped and the reverberation response from the specimen is recorded. This detection is carried out either with a laser vibrometer or with a contact transducer which is sensitive to this resonant frequency. The detected signal, consisting of a decaying time signal, is then analysed. This waveform is broken up into several time windows, each with typically a 20-cycle duration. Exponentially decaying sine functions are then fitted to each window and the frequency content between each window is compared. If the material is linear and damage-free, then there is no change in frequency content between the windowed data. However, the presence of damage means that the reverberation signal frequency content increases with time. This can then be plotted directly as a function of amplitude of the reverberation signal.

Materials such as carbon fibre reinforced plastics (CFRP) have produced positive nonlinear measurements [92]. Here, a number of samples were exposed to different temperatures to change the elastic (i.e. nonlinear) properties of the material.

The NRS technique is useful to globally test for damage in a given sample or component and, therefore, would lend itself well to a 'pass or fail' test scenario, but to actually locate the precise region of damage, further experimental techniques would also incorporated.

2.4 Summary

This chapter began with a review of material elasticity and showed how stress and ultrasonic velocity are related. Numerous nonlinear experimental methods were described including the higher harmonic generation method, parametric interaction, NL-TRA and NRS. Most of these techniques are sensitive to material nonlinearity brought on by the presence of a crack or a region of damaged material. The ability to identify the location, or even simply detect the presence of damage within a specimen minimises the risk of failure while in use. However, NDT techniques capable of measuring changes in material nonlinearity before the initiation of a crack are a very important tool that would have applications in a broad range of industries. This would require an extremely sensitive experimental technique, but if it was possible, it would allow the identification of potentially problematic specimen areas thereby minimising the risk of catastrophic failure of a component.

Using this knowledge obtained from these nonlinear techniques, accurate tolerances for various parts of an aircraft could be specified. The experimental method presented in this thesis is capable of measuring material nonlinearity and the next stage in the development of this method would be to apply it to fatigued samples.

At the very early stages of fatigue, nonlinear measurements are efficient at detecting damage. However, if too many microcracks appear (or if the microcracks become too large) in the area on the sample, then it becomes difficult for the ultrasound to propagate through the material. In this case, a linear ultrasonic technique (e.g. wave reflection) could be considered a more suitable approach.

Chapter 3

Instrumentation

3.1 Introduction

This chapter will describe the OSAM instrument, in terms of its optical and electronic configuration, the generation and detection setups, and the calibration procedure for the knife-edge detector. Finally the high speed analogue electronics used to acquire the magnitude and phase information of the detected ultrasound will be described. This set of electronics was not used for the nonlinear experiment, however it proved useful for taking aerial point spread functions (PSFs) of several samples, which have been included in section 1.6.2.

3.2 Optical setup for the generation of ultrasound

The optical system used for the generation of ultrasound is shown in figure 3.1.

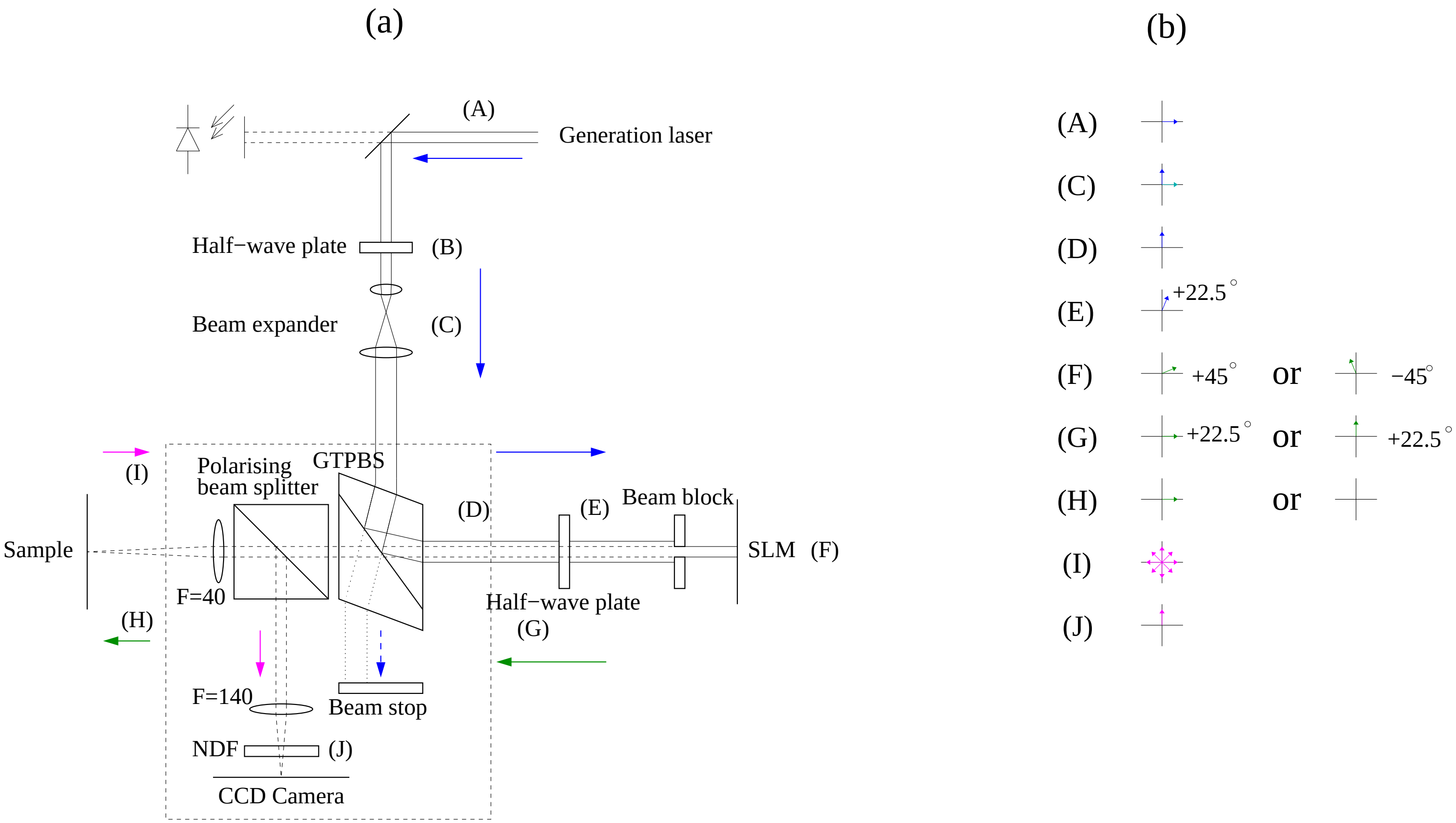

Figure 3.1: Optical setup (a) for laser generation of ultrasound (not to scale) and flow diagram (b) of the system. The main points (A)−(J) will be discussed in sections 3.2.1 to 3.2.5. The dashed box refers to section 6 (F, focal length).

3.2.1 Generation source

The generation laser (A) is a Q-switched and mode-locked infra-red (IR) laser that emits light at a wavelength of 1064nm. In order to generate SAWs, the laser has to be pulsed and this is the purpose of the mode-locker. By pulsing the laser, the sample surface that is illuminated by the beam experiences thermal expansion and contraction at the same rate as the pulsing frequency. This dictates the frequency of the generated SAW. A mode-locker is an acousto-optical device placed in the laser cavity and its frequency of operation, f is related to the laser cavity length by equation 3.1.

$$f = \frac{c}{2L} \tag{3.1}$$

where c is the speed of light and L is the cavity length. The laser cavity is 1.83m in length, meaning the fundamental frequency of the laser is 82MHz. In the mode-locked state, the laser generates a continuous train of pulses, which are separated by $1/82\times10^6$s. The duration of each pulse is 200ps and since these pulses are very short in time, the laser output has a high harmonic content.

The Q-switcher can operate at repetition rates ranging from a few hundred hertz up to 100kHz, although with higher frequencies, the peak power levels off and is eventually reduced. In the OSAM system, the Q-switcher operates at 1015Hz, and is dictated by the operating frequency of the SLM.

Between each trigger event of the Q-switcher, the energy within the laser accumulates and is then released over a 0.4μs time window. In this way, the Q-switcher increases the peak optical power of the laser source, thereby increasing the amplitude of the generated SAW. The average optical power output from this laser system has been measured at 2.4W. There are approximately 30 pulses in each Q-switched burst, equating to 80μJ/pulse.

The horizontally-polarised light emitted from the generation laser is directed onto a half-wave plate (B) using a mirror (reflectance >99.2%). The light that is transmitted by the mirror is incident onto a photodetector, which provides a 'coherent trigger pulse'. Figure 3.2(a) shows the output of the photodetector and figure 3.2(b) is the Fourier transform of the signal.

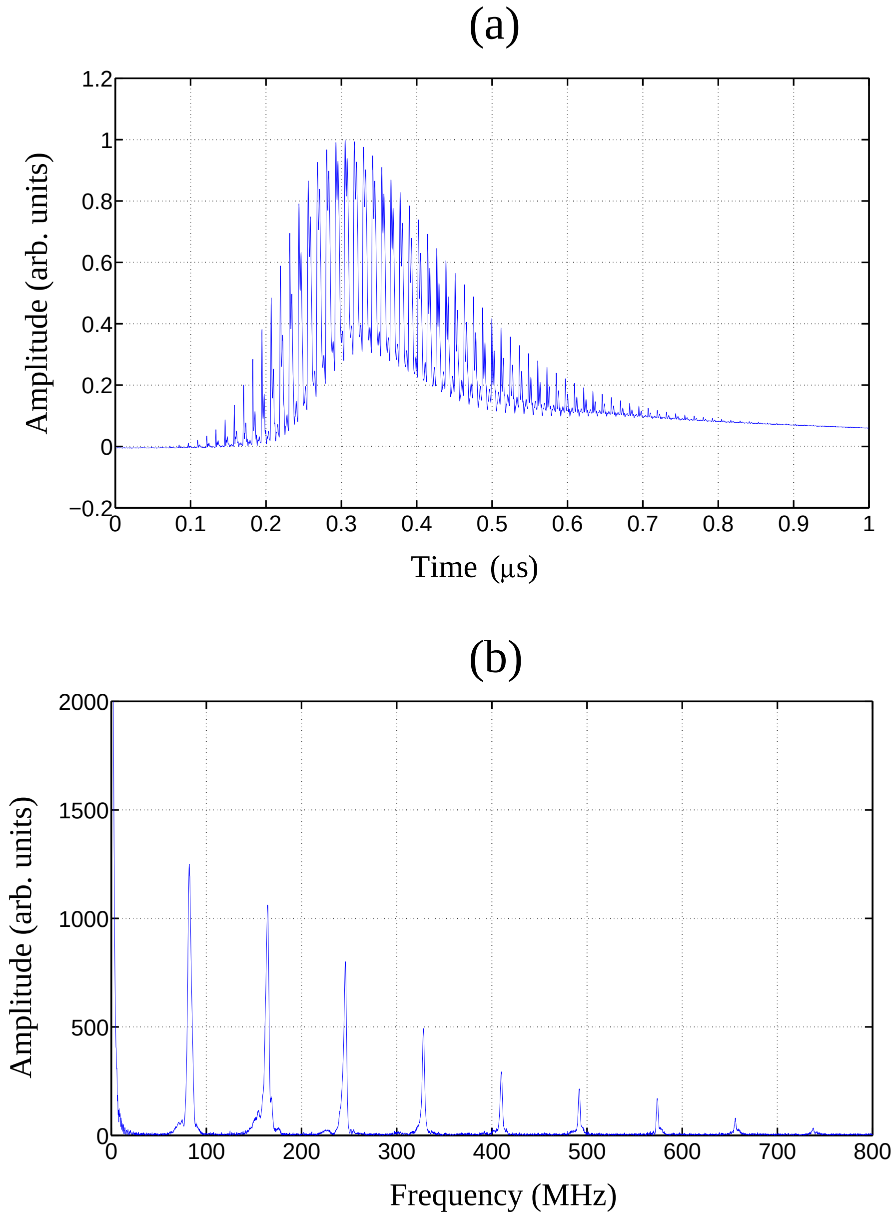

Figure 3.2: The coherent trigger pulse in the time (a) and frequency (b) domains detected by the photodiode placed at the end of the laser cavity.

In theory, the amplitude of all the harmonics should have the same amplitude as the fundamental frequency up to 5GHz (since 200ps pulses), however, because the photodetector (and electronics) has a limited bandwidth, the amplitude of the harmonics decreases at higher frequencies (figure 3.2(b)).

3.2.2 Beam expansion

The Glan Taylor polarising beam splitter reflects vertically-polarised light towards the SLM and transmits horizontally polarised light towards the beam stop. Therefore, it is important to maximise the vertically-polarised contribution incident on the beam splitter. This is achieved by placing a power meter after the beam splitter and rotating the halfwave plate (B) until maximum light power is measured.

The active area of the SLM is 7.68×7.68mm and it is important to illuminate as much of this as possible. The beam emitted directly from the laser has a diameter of approximately 1.5mm, meaning that an expansion ratio of 5 is required. Between the halfwave plate and the Glan Taylor beam splitter is a beam expander (C) that uses a combination of two lenses (figure 3.3).

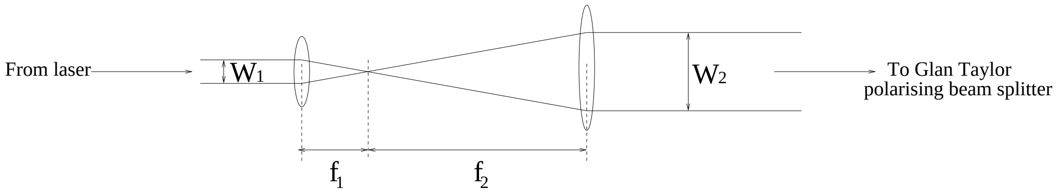

Figure 3.3: Beam expander optical set-up.

The magnification factor is determined by the focal length ratio of the two lenses and is related to the beam diameters before (W_1) and after (W_2) expansion by equation 3.2.

$$\frac{W_2}{W_1} = \frac{f_2}{f_1} \tag{3.2}$$

where f_1 and f_2 are the focal lengths of the lenses and are 40mm and 180mm, respectively.

3.2.3 Beam manipulation

The Glan Taylor beam splitter used in the OSAM instrument (Halbo Optics: PBS12M) is made of two calcite prisms, assembled together with an air-space between them (figure 3.4).

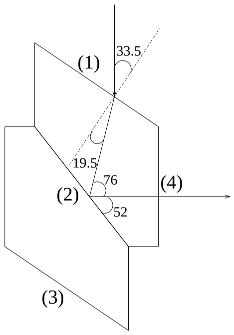

Figure 3.4: The Glan Taylor polarising beam splitter used in the OSAM system (Scale: 1:1). The path of the vertically polarised light is shown in (1)−(4).

For maximum system efficiency, the beam incident on surface (1) of this Glan Taylor beam splitter needs to be vertically-polarised. However, if the beam does have both vertical and horizontal components, then the birefringent properties of the calcite causes them to be refracted at different angles and therefore, hit surface (2) at different angles. Side (1) is cut at an angle so that the vertically-polarised light hits surface (2) at the critical angle for total internal reflection (TIR) to occur, while the horizontally-polarised light hits (2) at a different angle. This means that horizontally-polarised light exits the beam splitter at (3) and vertically -polarised light exits at (4). This particular Glan Taylor polarising beam splitter is unusual because the shape of the prisms have been designed so that the reflected and transmitted light are orthogonal to each other, which is convenient for the layout of the OSAM optical system.

Any light exiting at (3) is incident on a beam stop and is wasted. The useful (vertically-polarised) light leaves the beam splitter at (4). This is rotated by +22.5° by the halfwave plate (E) and is then reflected by the SLM (F), undergoing a +45° or −45° rotation accordingly (the reason for this is described in section 3.2.4). When passing back through the halfwave plate, the light experiences another +22.5° rotation (G). At this point, the light is either horizontally or vertically polarised, depending on the SLM and will be either transmitted or reflected by the Glan Taylor beam splitter respectively.

The horizontally polarised light passes back through the Glan Taylor beam splitter, through a second polarising beam splitter (the purpose of which will be described in section 3.2.5) and is focused by a lens onto the surface of the sample (H). Meanwhile, the vertically polarised light is reflected by the Glan Taylor beam splitter back towards the generation laser.

Between the halfwave plate and the SLM is an aperture comprising a rectangular window. Its purpose is to absorb the laser beam energy that would otherwise fall onto the highly sensitive electronics surrounding the active part of the SLM, thereby removing the potential for damage.

3.2.4 SLM

The SLM is an analogue ferroelectric liquid crystal-spatial light modulator (FLC-SLM) system developed by Boulder Nonlinear Systems Incorporated (BNS). The purpose of the SLM is to manipulate the light that is reflected from it into a required intensity profile or distribution, which is then focused onto the sample. It has a 512×512 pixel array with a 15μm pitch and an overall size of 7.68×7.68mm. The approximate size of the SLM image on the sample surface is 2×2mm.

Each individual pixel can be regarded as a reflective halfwave plate and the polarisation angle of the reflected light is controlled by an applied voltage that has 256 discrete states and is in turn, controlled by the host computer. Using these input voltages, the angle of rotation ranges from −45° (control level 0) to +45° (control level 255), relative to the incident polarisation angle.

In the optical system shown in figure 3.1, if a pixel has an input control level of 0, the area of the sample that the pixel is imaged onto will not be illuminated ('black'). Conversely, a control level of 255 would mean that the same area will be illuminated with 100% of the available laser power ('white'). Finally, if an intermediate control level is selected, a corresponding fraction of laser power would be incident on the sample. Therefore, the SLM can be considered an analogue device. However, in the OSAM system, the SLM is used in a 'digital' mode of operation, where only black or white illumination levels are required. Figure 3.5 schematically illustrates how the polarisation angle of the laser beam is manipulated.

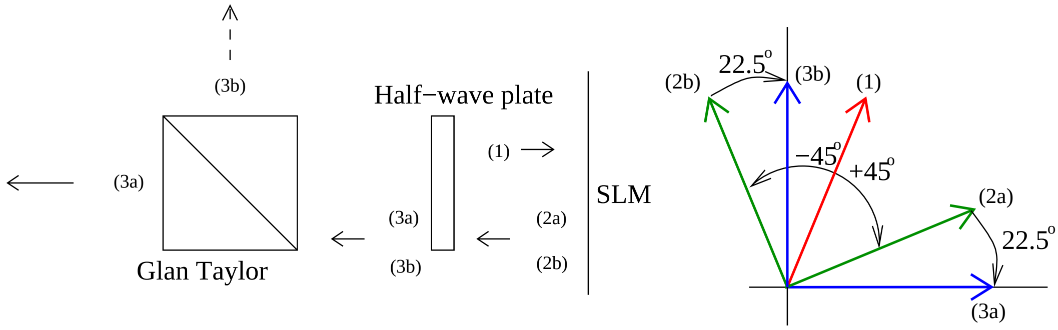

Figure 3.5: The polarisation angle of the light incident on the SLM (1), is rotated by +45° (2a) or −45° (2b), depending on the pixels' input voltage. The half-wave plate rotates the polarisation angle by +22.5° so that the light is either horizontally (3a) or vertically (3b) polarised. The horizontally-polarised will be transmitted by the Glan Taylor polarising beam splitter and be incident on the sample. The vertically polarised light is reflected back towards the source.

The light leaving the Glan Taylor (on its way to the SLM) is vertically polarised and is rotated by +22.5° by the half-wave plate (indicated by the red arrow in figure 3.5). Depending on the SLM control level, the reflected light is either rotated by +45° or −45° (green arrows). The half-wave plate then rotates the reflected light by +22.5° so that it is either horizontally or vertically polarised (blue arrows). The former will be transmitted by the Glan Taylor and be incident on the sample, while the latter is reflected back towards the laser.

The SLM image is controlled by uploading a 512x512 element picture from the computer and can be completely arbitrary. These images are either a series of lines or arcs that generate plane or focused ultrasound. The separation of the lines in both cases has to match the mode-locked frequency of the laser (or a harmonic of this frequency). The pitch is chosen according to $v = \lambda f$, where v is the Rayleigh wave velocity of the material, f is the frequency of ultrasound that is to be generated and λ is the acoustic wavelength or line separation.

Since the laser source only generates frequency components of 82MHz and its harmonics, the value of f in the above equation can only be multiples of 82MHz. On glass, for example, the velocity is 2096m/s, so at 82MHz a 36μm line spacing is required. This means that there are approximately 60 lines within the SLM image.

To demonstrate the relationship between the pixel control level and polarisation angle (light intensity on sample), an experiment was performed in which the SLM was programmed to generate a series of arcs onto the surface of a glass sample. The line spacing of the arcs was chosen to generate 82MHz SAWs and at the arc focus, the signal was detected by a knife-edge detector (see section 3.3). At each control level, an 82MHz signal was detected and the 82MHz frequency component extracted (figure 3.6). Outside of the $30-200$ pixel control level range, the SLM has a more 'nonlinear' response. However, this is not a critical issue because only 0% or 100% illumination levels are required in the OSAM system. By maximising the degree of contrast between illuminated and non-illuminated areas of the sample, higher SAW amplitudes are generated.

3.2.5 Camera system

In order to view the pattern generated by the SLM on the sample surface, a camera system was incorporated, hence the reason for the second beam splitter. The light that is reflected from the surface of the sample figure (3.1(I)) will be partially depolarised due to the rough surface of the sample. The 40mm focal length lens is

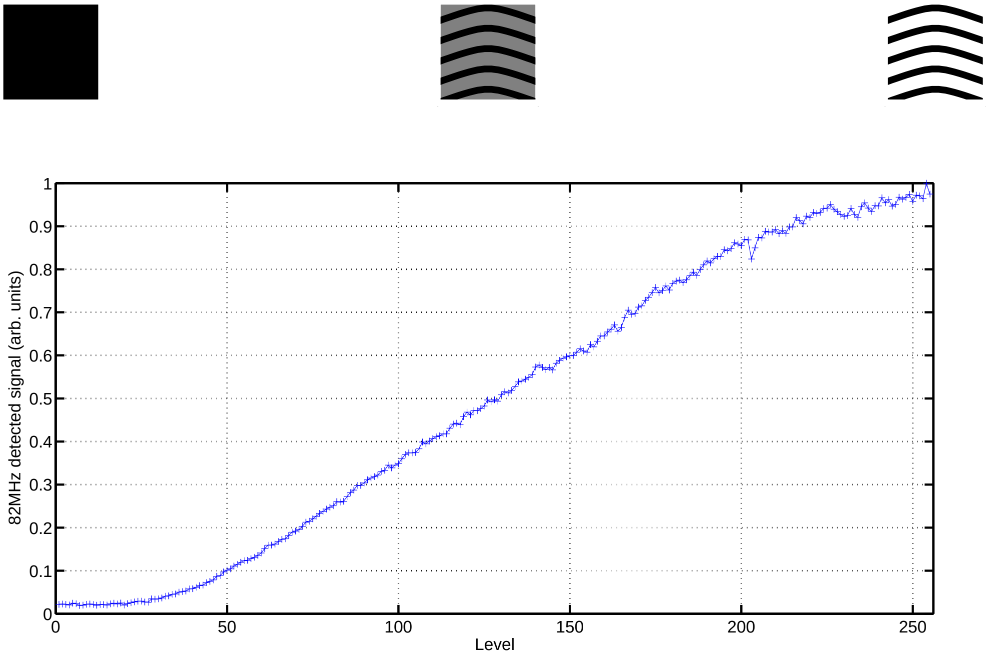

Figure 3.6: The detected 82MHz SAW with increasing pixel control level. At level 256, maximum contrast is obtained.

used to collect this light, which is then directed by the second beam splitter to the charge-coupled device (CCD) camera. A 140mm lens is used to focus the light onto the camera. A neutral density filter (NDF) is placed in front of the CCD camera (J) to reduce the light intensity on the camera and optimise the image.

3.3 Knife-edge detector

The detection system used in the OSAM instrument was a knife-edge detector. The general principle has been reviewed in section 1.7.1, and the following sections will explain how the detector is configured in terms of the optics and electronics.

3.3.1 Optical configuration

The OSAM instrument uses a knife-edge detector comprising two photodiodes (figure 3.7). The reflected beam from the sample surface oscillates between the two photodiodes when the surface of the sample is displaced by a passing SAW.

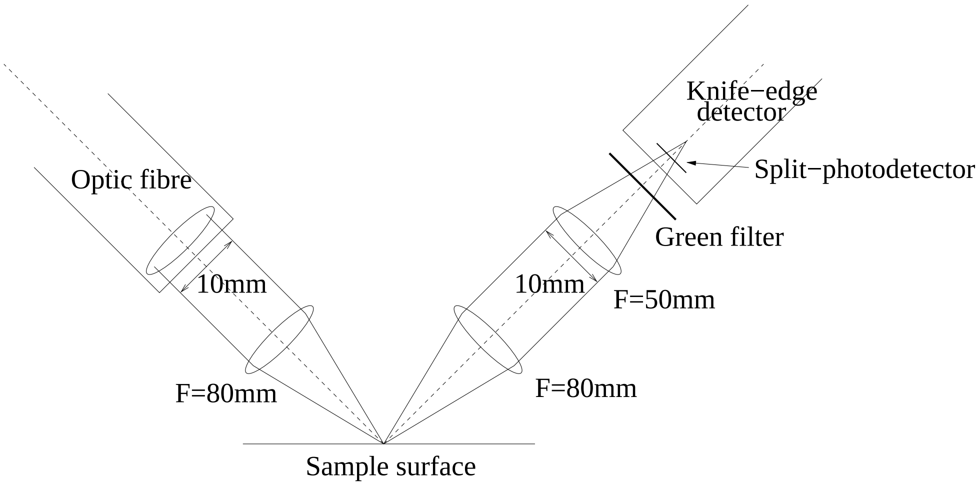

Figure 3.7: Schematic diagram of the modified knife-edge detection system. All optical components, as well as the detector are mounted on the detector arm so that all components are in a fixed position relative to each other. The entire detector arm is attached to x-y stages, enabling the detector to be moved relative to the sample.

The detection laser is a doubled neodymium-doped yttrium aluminium garnet (Nd:YAG) CW laser which generates light at a wavelength of 532nm. It has a power level of 150mW and is coupled to an optic fibre, the output aperture of which is then attached to the detection arm. The arm itself can be moved by computer controlled x-y stages, enabling scanning of the detector beam relative to the sample. A manual z-stage is also used to focus the detector with respect to both the sample and the generation system.

The beam that exits the fibre is expanded and collimated to a diameter of 10mm and a NDF can be inserted at this stage to reduce the optical power if required. The beam is then focused onto the sample surface using a lens of focal length 80mm and the reflected beam is collected by a second lens, also with focal length 80mm, producing a parallel beam with a diameter of 10mm. A focusing lens with a focal length of 50mm is placed in front of the knife-edge detector and a green filter is used to prevent any stray IR light from the generation laser entering the detector. The lens situated in front of the knife-edge detector can be moved in the vertical and horizontal planes to ensure that the beam is accurately focussed and covers equal areas of the two detectors.

As the sample surface is tilted by a passing SAW, the reflected beam is shifted. In order for the detector to sense the surface tilt, the photodiodes have to be placed either slightly in front or behind the beam focus (i.e. a 180° phase difference exists between the two positions).

3.3.2 Electronic configuration

The knife-edge detector consists of two sets of electronics, termed as the ‘front-end’ and ‘back-end’ electronics. Both will be described in this section, however, first it is important to describe where these fit into the overall detector system (figure 3.8).

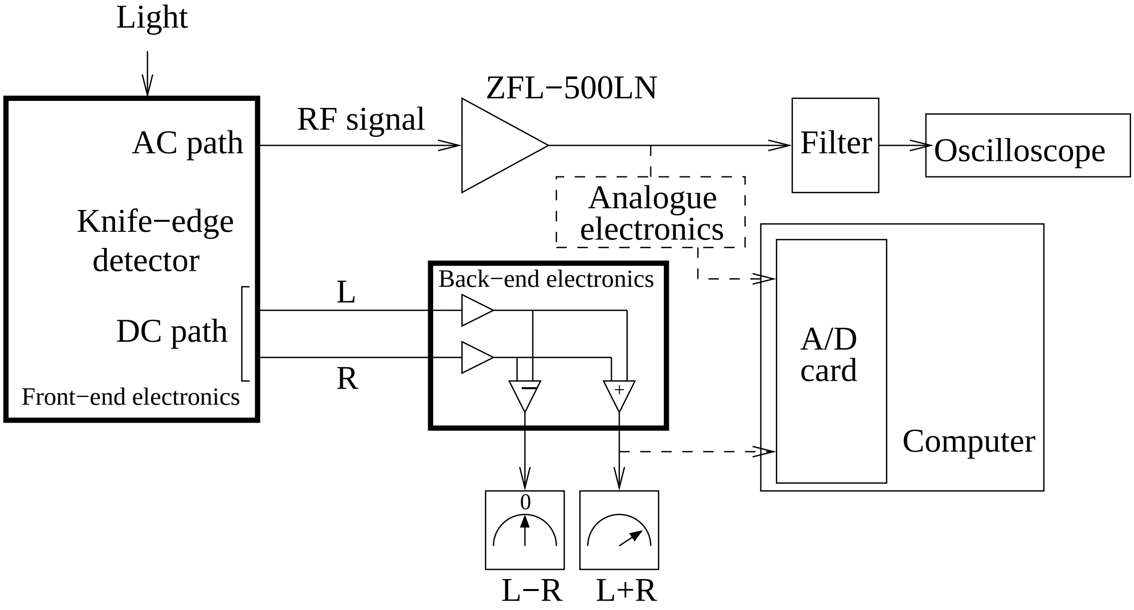

Figure 3.8: Schematic of the complete detector system. The front-end and back-end electronic sections of the knife-edge detector are outlined in bolded boxes. The analogue electronics (dashed box) were not permanently connected to the experimental apparatus.

There are two output paths from the front-end electronics of the knife-edge detector. The first is the alternating current (AC) path, in which the radio-frequency (RF) signal (generated by the ultrasound) is amplified, filtered and observed on an oscilloscope. The data required for the nonlinear experiment were obtained using the oscilloscope. Occasionally, the analogue electronic system (that outputs the real and imaginary components of the RF signal to the analogue-to-digital converter [A/D] card in the computer) was used for acquiring c-scans and aerial PSFs. As the analogue electronics were not used for the nonlinear experiment, it was not permanently connected to the detection system and, therefore, is discussed separately in section 3.5.

The second output path from the front-end electronics is the direct current (DC) path, consisting of a 'left' and a 'right' channel corresponding to their respective photodiodes. The information obtained from these channels was used to balance the knife-edge detector so that equal light intensities are incident on both photodiodes. This was achieved by manually moving the lens situated in front of the photodiodes (figure 3.7).

The back-end electronics consist of a system of amplifiers that add and subtract the signals in the left and right channels. Measuring the difference between them provides an indication of how central the laser beam is on the photodiodes. For a fully balanced system, this difference should be zero. By adding the two signals together, the combined light intensity is obtained. The L−R and L+R signals are connected to voltmeters to indicate when the system is aligned correctly.

The L+R output channel from the back-end electronics can also be connected to the A/D card in the computer. This is not required for the nonlinear experiments but is useful for imaging a sample because it provides a measure sample reflectivity. It is referred to as the 'DC light image' or the 'optical image' [93].

Front-end electronics

The front-end electronics are shown in figure 3.9. In order to be sensitive to high frequency SAWs (up to 300MHz) a fast detector system is required. The response time of the photodiode is fundamentally determined by its size − the smaller the photodiode, the faster its response. A Hamamatsu S6058 silicon pin photodiode was used since it is a quadrant detector and, therefore, consists of 4 small (0.295×0.595mm) photodiodes − although only two were used for the knife-edge detector. At a wavelength of 532nm the photosensitivity of these photodiodes is 0.35A/W, the photodiode pitch is 0.305mm and the separation is 10μm.

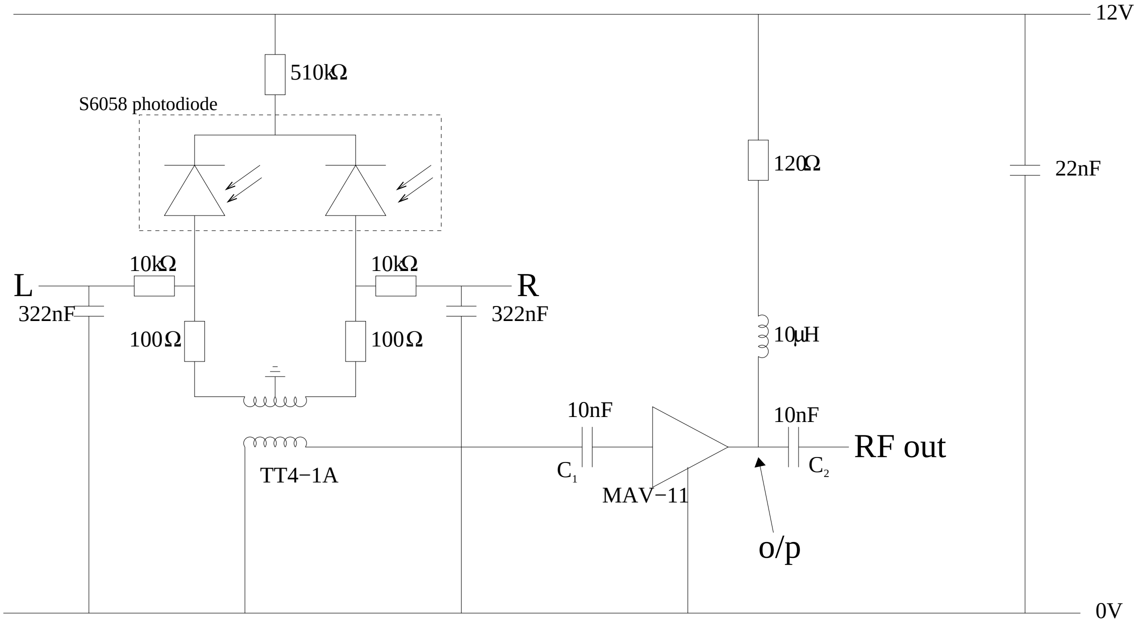

Figure 3.9: The knife-edge detector front-end electronics (o/p, output pin).

Both photodiodes are reverse-biased to widen the depletion zone, thereby increasing the reaction volume and making their response time faster. The photodiodes are connected to the positive supply via a 510Ω resistor. The purpose of this resistor is to limit the current drawn by the photodiodes so that if there is an unusually intense laser beam incident on the photodetectors, the risk of any damage is reduced.

When laser light is incident on a photodiode, a current flows from the positive rail down through the 100Ω resistor to the ground connection, via the primary coil of the transformer.

In the absence of a SAW, the light intensity incident on the photodiodes is constant and, therefore, no current is induced in the secondary windings of the transformer. However, a passing SAW causes the reflected beam to oscillate between the two photodiodes, generating an alternating current in the primary coil of the transformer. This gives rise to a changing magnetic field, generating a current in the secondary coil of the transformer. The TT4-1A type transformer being used here has a useful frequency response from 100kHz to 300MHz.

A MAV-11 monolithic amplifier with a gain of 12.7dB is used to amplify the output of the transformer. The amplifier is powered through its output pin (o/p figure 3.9), connected to the supply rail via a 120Ω bias resistor, the value of which is given by equation 3.3.

$$R_{bias} = \frac{V_c - V_d}{I_{bias}} \tag{3.3}$$

where V_c is the supply voltage (12V), V_d and I_{bias} are the voltage and current values at the output pin specified to be 5.5V and 60mA, respectively, by the manufacturer. A 10μH inductor is required to ensure no loss of RF signal due to the bias connection and that the RF signal on the output does not feedback to the input via the power rail (since gain is related to V_d), thereby causing oscillation.

Both the input and output pins are connected to capacitors (C_1 and C_2) to block any DC. The appropriate capacitor value is chosen for a particular frequency range of operation. The low frequency cutoff (f_c) of the amplifier is given by equation 3.4.

$$f_c = \frac{1}{2\pi RC} \tag{3.4}$$

where R is the load impedance on the transformer secondary winding (50Ω) and C is the value of the capacitor. In terms of frequency range, it is necessary to be able to detect 0.5MHz SAWs, in which case from equation 3.4, a minimum of 6.4nF is required. The actual value of the capacitors used was 10nF.

A single resistor and a capacitor are connected to the output of the left and right channels as shown in figure 3.9 and the DC voltages at these points (L and R) are then connected to the back-end electronics.

Back-end electronics

Figure 3.10 shows the circuit diagram for the back-end electronics used in the knife-edge detector system.

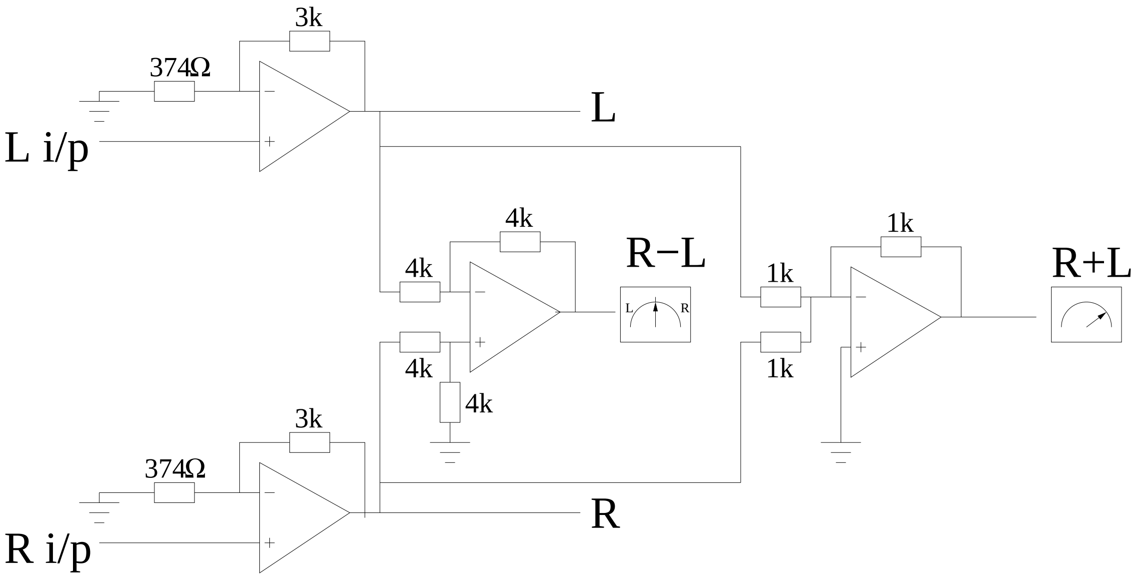

Figure 3.10: Detection system back-end electronics used to amplify the left (L) and right (R) channels of the front-end knife-edge detector electronics. The sum and difference signals are used to balance the detector.

The signals from the left and right channels are amplified by two non-inverting amplifiers, both of which have a gain factor of 9. A differential amplifier is used to provide the difference between the two channels, and when perfectly balanced the voltage output from the difference amplifier is zero. A summing amplifier is then used to provide the sum of the two channels and, therefore, the overall magnitude of the light intensity received by both detectors. This has to be maximised for optimal detector sensitivity. Voltmeters connected to the outputs of these amplifiers provide the visual means for optimum system setup.

3.3.3 Calibrating the detector system

A knife-edge detector does not give absolute surface displacement measurements, instead a measure of surface gradient is obtained. In order to obtain surface displacement, the knife-edge detector system has to be calibrated. A wave propagating on the surface of the sample (figure 3.11), can be represented by equation 3.5.

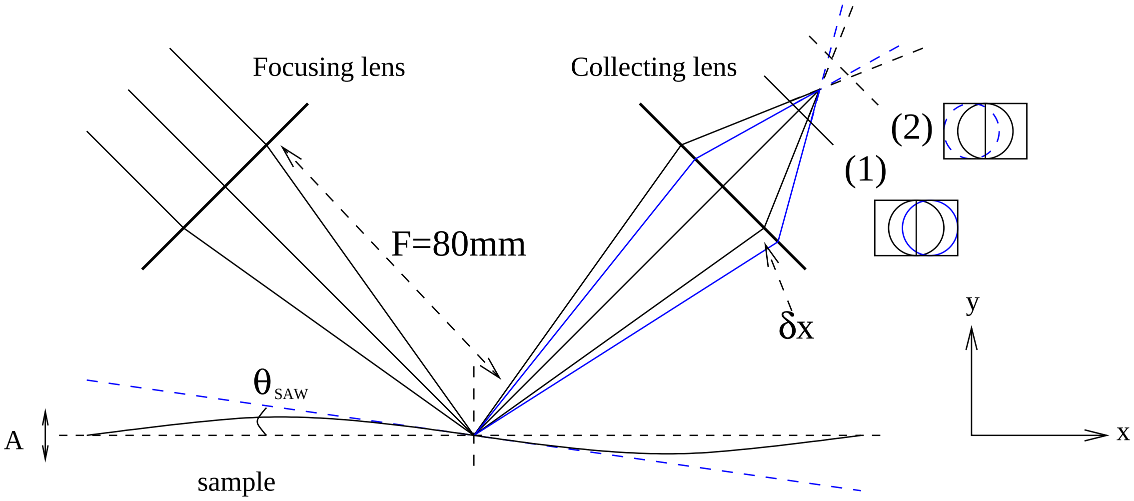

Figure 3.11: The knife-edge detection technique. A passing SAW causes the reflected beam to oscillate by δx. The position of the photodiodes can be either before (1) or after (2) the focus point of the collecting lens. The difference between the two is a 180° phase difference.

$$y = Asin(kx + \omega t) \tag{3.5}$$

where A is the wave amplitude, k is the wave number, ω is the angular frequency and t is time. The knife-edge detector is sensitive to the surface gradient caused by the wave and is given by equation 3.6.

$$\frac{dy}{dx} = kAcos(kx + \omega t) \tag{3.6}$$

The surface gradient, θ_{SAW}, is equivalent to $tan^{-1}(\frac{dy}{dx})$, but if all angles are assumed to be small, then θ_{SAW} can be given by equation 3.7.

$$\theta_{SAW} \approx \frac{dy}{dx} \tag{3.7}$$

The sample displacement due to the presence of this SAW causes a change, δx, in the position of the intensity distribution, as shown in figure 3.11, and is given by equation 3.8 [52].

$$\delta x = 2\theta_{SAW} F \tag{3.8}$$

where F is the focal length of the focusing lens shown in figure 3.11. The maximum deviation of the reflected beam is, therefore, obtained by substituting equation 3.7 into equation 3.8 to give equation 3.9.

$$\delta x = 2\frac{dy}{dx}F \tag{3.9}$$

and substituting 3.6 into 3.9 we obtain equation 3.10

$$\delta x = 2kAcos(kx + \omega t)F \tag{3.10}$$

For maximum surface displacement, δx is equal to 2kAF. Figure 3.12 shows how the reflected beam deviates from its zero displacement position to the maximum displacement position. Assuming that the photodiodes are sufficiently large so that all the light is collected and that there is no space between them, the power drop observed on one photodiode is equal in magnitude to the power gained by the other.

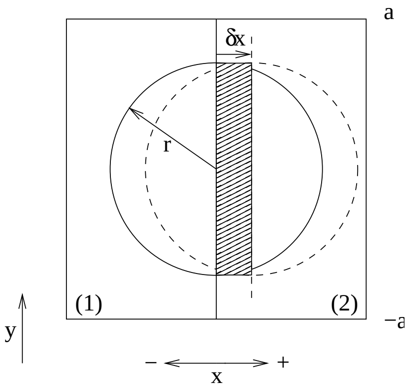

Figure 3.12: The reflected beam is displaced by δx. The shaded part is the increase in light on detector (2) and is equal to the decrease in light on detector (1).

The current, δi, in one photodetector is given by equation 3.11.

$$\delta i = Q_e \int_{-a}^{a} I(x,y)|_{x=0} dy dx \tag{3.11}$$

where Q_e is the quantum efficiency of the photodiode and I is the incident light intensity. Equation 3.11 can be simplified to equation 3.12.

$$\delta i = Q_e I_{line} 2kAF \tag{3.12}$$

where I_{line} is the integral light intensity along the vertical line at $x = 0$ and is given by equation 3.13.

$$I_{line} = \int_{-a}^{a} I(y) dy \tag{3.13}$$

For a top-hat beam profile,

$$I(y) = \begin{cases} \frac{P}{\pi r^2} & \text{for -r<y<r} \\ 0 & \text{for -r>y>r} \end{cases}$$

where P is the laser power and r is the beam radius. Substituting I(y) into 3.13 gives equation 3.14

$$I_{line} = \int_{-r}^{r} \frac{P}{\pi r^2} dy = \frac{2P}{\pi r} = \frac{2P}{\pi (NA) F} \tag{3.14}$$

where NA is the numerical aperture given by NA=$\frac{r}{F}$. Substituting equation 3.14 into equation 3.12 gives equation 3.15:

$$\delta i = \frac{4 Q_e P A k}{\pi (NA)} \tag{3.15}$$

and substituting $k = \frac{2\pi}{\lambda}$ (where λ is the wavelength of the wave) into 3.15 produces equation 3.16:

$$\delta i = \frac{8 Q_e P A}{\lambda (NA)} \tag{3.16}$$

The next stage is to determine the DC and AC output voltages of the detector electronics. Figure 3.13 shows the DC and AC equivalent circuits.

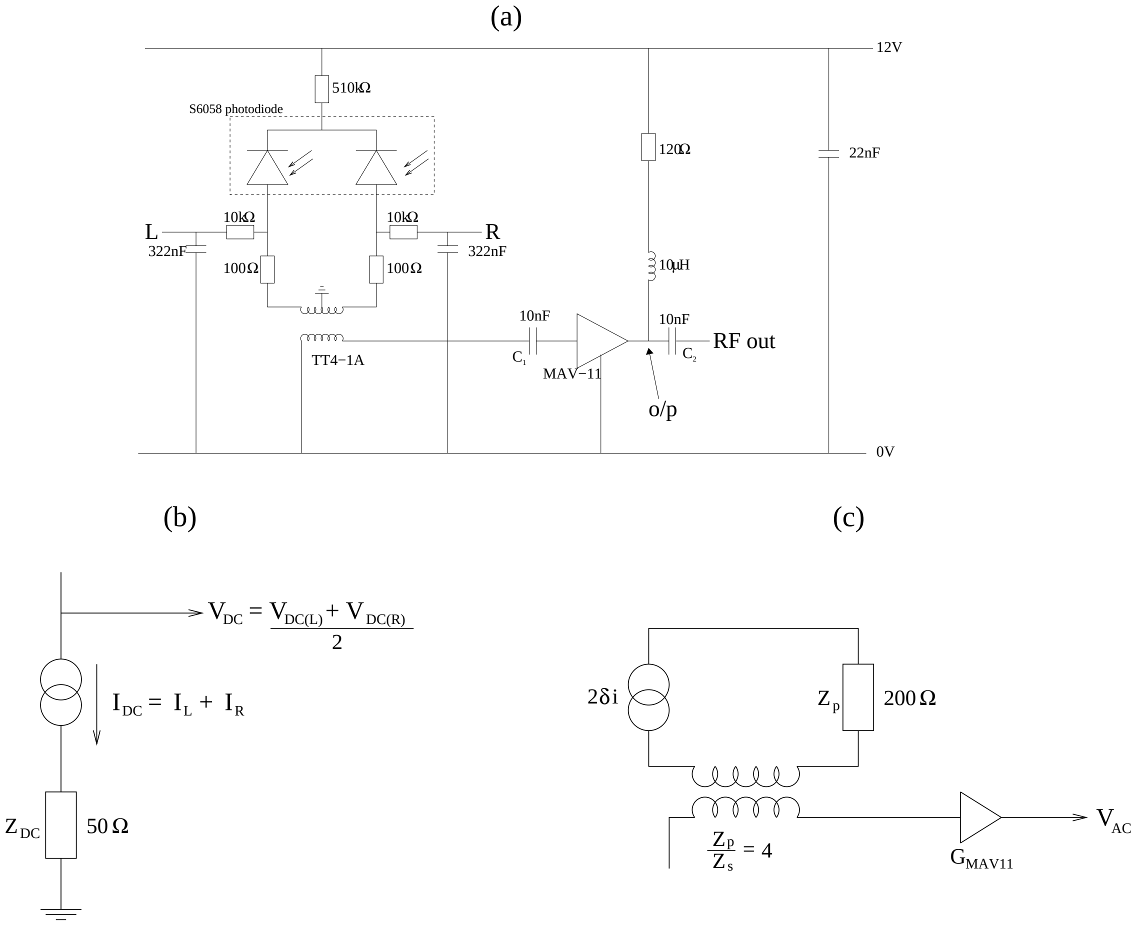

Figure 3.13: Knife-edge detector front-end electronics (a) and its DC (b) and AC (c) equivalent circuits. In terms of the DC circuit, both photodiodes can be considered as a single current source producing a current (I_{DC}) through a 50Ω resistor. The DC voltage (V_{DC}) is the sum of the voltages in the left ($V_{DC(L)}$) and right ($V_{DC(R)}$) channels. In the AC circuit, the current generated by both photodiodes is 2δi (δi is given by equation 3.16) and the transformer impedance ratio ($\frac{Z_p}{Z_s}$) is 4. A monolithic amplifier (with gain, G_{MAV11}) is connected to the secondary side of the transformer and the output signal is V_{AC}.

The DC current (I_{DC}) and voltage (V_{DC}) are given by equations 3.17 and 3.18, respectively.

$$I_{DC} = Q_e P \tag{3.17}$$

$$V_{DC} = I_{DC} Z_{DC} = Q_e P Z_{DC} = Q_e P 50 \tag{3.18}$$

where Z_{DC} is the resistance in the DC equivalent circuit. The impedance ratio ($\frac{Z_p}{Z_s}$) of the transformer is 4 and is, therefore, equivalent to a voltage ratio of 2. The voltages across the primary windings (V_p) and secondary windings (V_s) of the transformer are given by equations 3.19 and 3.20, respectively.

$$V_p = 2\delta i Z_p = 2\delta i 200 \tag{3.19}$$

$$V_s = \frac{V_p}{2} = \delta i Z_p = \delta i 200 \tag{3.20}$$

where Z_p is 200Ω (figure 3.13(c)). The AC voltage (V_{AC}) is given by equation 3.21:

$$V_{AC} = V_s G_{MAV11} = 200\delta i G_{MAV11} \tag{3.21}$$

where G_{MAV11} is the gain of the MAV-11 amplifier shown in figure 3.13(a). Substituting equation 3.16 into equation 3.21, we obtain equation 3.22

$$V_{AC} = \frac{1600 Q_e P A G_{MAV11}}{\lambda(NA)} \tag{3.22}$$

rearranging equation 3.18 for P and substituting into 3.22, generates equation 3.23

$$V_{AC} = \frac{32 V_{DC} A G_{MAV11}}{\lambda(NA)} \tag{3.23}$$

Rearranging equation 3.23 for A, we obtain equation 3.24:

$$A = \frac{V_{AC}}{V_{DC}} \frac{\lambda(NA)}{32 G_{MAV11}} \tag{3.24}$$

Equation 3.24 relates the surface displacement (A) to the output voltages from the front-end electronics (V_{AC} and V_{DC}). To complete the calibration of the detector system, the gains in the AC and DC output paths have to be considered. The complete detector system is shown in figure 3.14.

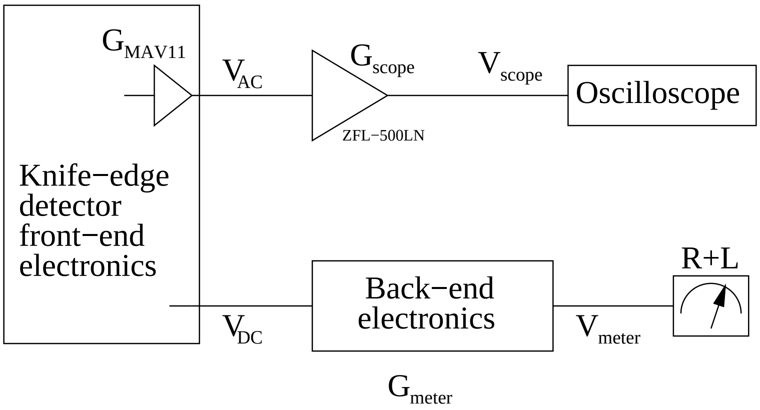

Figure 3.14: The complete detector system. The ZFL-500LN amplifier had a gain factor of 24 and the gain factor in the back-end electronics (see figure 3.10) is 18.

The voltages received by the oscilloscope and by the meter are given by equations 3.25 and 3.26 respectively.

$$V_{scope} = V_{AC} G_{scope} \tag{3.25}$$

$$V_{meter} = V_{DC} G_{meter} \tag{3.26}$$

By rearranging equations 3.25 and 3.26 for V_{AC} and V_{DC}, respectively, and substituting them into equation 3.24, we obtain equation 3.27:

$$A = \frac{V_{scope}}{V_{meter}} \frac{G_{meter}}{G_{scope}} \frac{\lambda(NA)}{32 G_{MAV11}} \tag{3.27}$$

The gain factors of the MAV-11 amplifier (G_{MAV11}) and back-end electronics (G_{meter}) is 4.32 and 18 respectively. The amplification in the AC path (G_{scope}) consisted of a ZFL-500LN mini-circuits amplifier with a measured gain of 24. Substituting these three gain values into equation 3.27 along with the NA value of $\frac{5}{80}$, we obtain equation 3.28:

$$A = 3.39 \times 10^{-4} \frac{V_{scope}}{V_{meter}} \lambda \tag{3.28}$$

Equation 3.28 was readily used for the results presented in Chapter 5.

3.4 CHOT system configuration

In addition to performing nonlinear experiments using the OSAM, CHOTs provided an alternative method of generating and detecting ultrasound [94]. This section describes the CHOTs that were specifically integrated into the nonlinear experiments described in section 4.4.

3.4.1 g-CHOT

A fused silica substrate was used for this nonlinear experimental work. Using photolithography, a g-CHOT, made up of multiple lines of titanium, was deposited on the sample. The efficiency of the g-CHOT was dependent on the absorption contrast between the substrate and the deposited material. The layer of titanium deposited was ∼146nm thick and the lines were equally spaced, which provided a periodic absorption contrast between the coated and non-coated areas of the substrate. When the incident laser beam was used to activate the g-CHOT, the titanium absorbed the radiation more strongly than the transparent fused silica substrate. Based on published reflection and transmission coefficients [95], it is estimated that 76% of the incident light radiation was reflected, 20% was transmitted and 4% was absorbed by the thin titanium layer. In contrast, the fused silica substrate transmitted 96% of the radiation through its 6mm thickness (according to the manufacturer), while 3% of it was reflected. The titanium coated parts of the fused silica experienced local thermal expansion, whereas the uncoated regions did not. The difference in local expansion when illuminated by a pulsed laser caused the generation of an elastic wave. Even though the absorption contrast between the g-CHOT pattern and the substrate was only 4%, it was still sufficient to generate detectable ultrasound.

Selecting appropriate line spacing

The line spacing was selected to match the acoustic wavelength of the ultrasound to be generated on the inspected material using $\lambda_{SAW}=v/f$: where λ_{SAW} is the acoustic wavelength (line spacing), v is the Rayleigh wave velocity and f is the frequency of the SAW. If the g-CHOT is activated by a laser containing a broad frequency spectrum, then the CHOT is designed to actively select any frequency within the bandwidth of the laser, and the outcome of this is narrowband-generated ultrasound. However, in this work the g-CHOT was activated by a Q-switched and mode-locked Nd:YAG laser. The output frequency spectrum from this source was narrowband with a fundamental frequency of 82MHz. This meant that the line spacing of the g-CHOT had to match the acoustic wavelength at 82MHz on the material. In order to accurately obtain the appropriate wavelength of a material (i.e. fused silica) with an unknown velocity, a 'λ-scan' was performed by the OSAM instrument prior to CHOT fabrication to measure the line spacing (figure 3.15). During this experiment, the SLM was programmed to adjust the line spacing and the 82MHz signal was detected by the knife-edge detector. The magnitude of the 82MHz frequency component was then plotted (figure 3.15). The 82MHz frequency component was most efficiently generated when the SLM line spacing was 41.7μm, which corresponded to a velocity of 3419ms^{-1}. For the experiments presented in this chapter, the actual spacing of the fabricated g-CHOT was 41μm.

Imaging ultrasound generated by the g-CHOT

Using the high-speed analogue electronics that were described in section 3.5, it was possible to image the generated ultrasonic field. This was achieved by raster scanning the knife-edge detector over the sample surface, and obtaining the amplitude and phase information of the detected signal at each point in the scan. The image that this produced is termed an aerial PSF. Figure 3.16 shows aerial PSFs obtained for

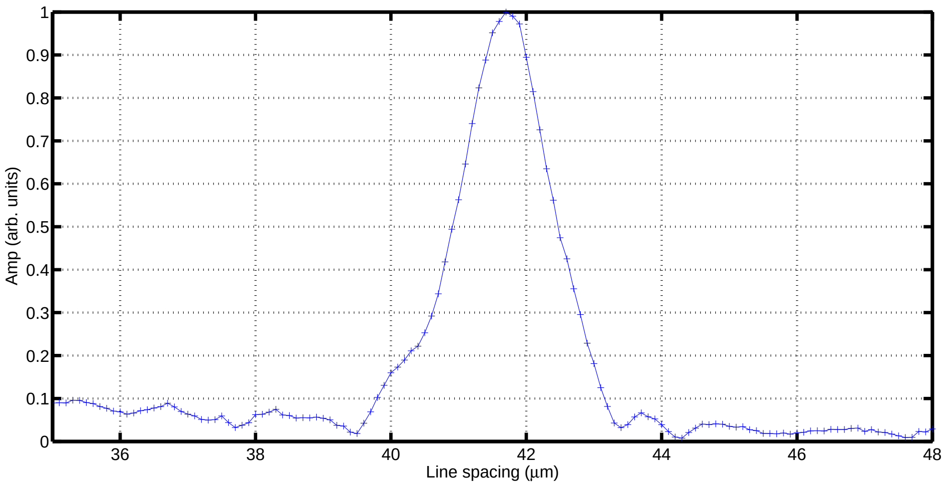

Figure 3.15: Using the SLM to accurately determine the appropriate line spacing of the g-CHOT on fused silica.

a plane and focused g-CHOT on fused silica.

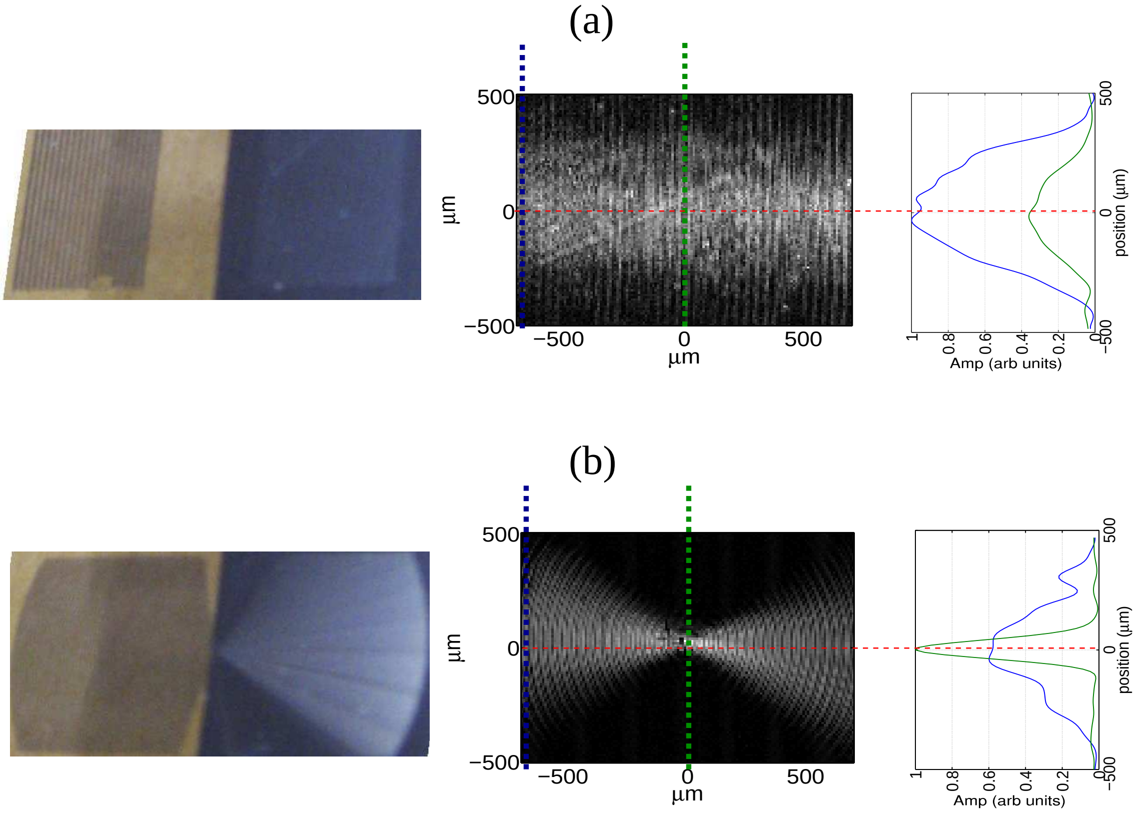

Figure 3.16: Aerial PSF from a plane (a) and focused (b) g-CHOT on fused silica. The knife-edge detector was scanned in 10μm steps over the sample surface. The plane wave g-CHOT was made up of titanium lines, while the focused g-CHOT structure was composed of deposited aluminium lines.

3.4.2 d-CHOT

The d-CHOT was made by evaporating an initial layer of silver (∼140nm) to make the sample surface reflective and then fabricating the lines using photolithography. The second deposited layer of silver created steps of ∼82nm in height. The step height was dependent on the incident angle of the laser beam (relative to the sample surface) and for the experiment presented in this work, the incident angle was 45°. According to equation 1.21, the steps should be 94nm in height for optimum operation at 45° incidence angle. Therefore, although the experiment was not operating at 100% optimum conditions, the reduction in efficiency was small and estimated to be 0.99 of the optimum value.

Optical configuration

For the nonlinear experiments performed in this work, a frequency doubled 532nm Nd:YAG CW laser was used at an incident angle of 45° relative to the sample surface. The d-CHOT was activated by focusing the detector laser beam to a 2mm spot using a combination of two lenses shown in figure 3.17.

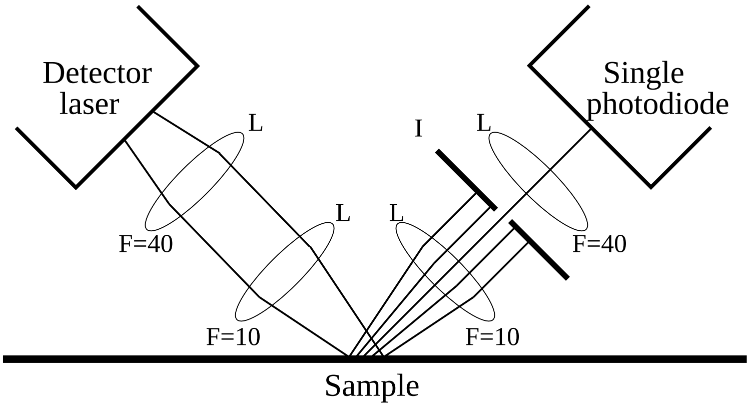

Figure 3.17: Basic optical configuration required for the activation of the d-CHOT. L=lens, fl=focal length (mm), I=iris.

The light power at the sample surface was measured to be 30mW. The reflected beam was split into several diffractive orders by the d-CHOT and an iris was used to select the zero order beam, which was focused onto a single photodiode detector using a 40mm focal length lens.

Electronic configuration

The detector electronics required to detect the signals are shown in figure 3.18. A BPX65 pin photodiode is reverse-biased to maximise its sensitivity to light. When light is detected a current flows from the 12V positive rail down through the 200Ω resistor to ground, via the primary coil of a mini-circuits ADCH-80A transformer. The change in magnetic field brought on by the current flow in the transformer coil gives rise to a current flow in the secondary winding. This is amplified by a MAV-11 monolithic amplifier, which is powered through its output pin, connected to the supply rail via a 120Ω bias resistor and a 10μH inductor. The capacitors positioned either side of the amplifier act as a highpass filter. The values of the capacitors are chosen so that there is a 67.7MHz cut-off frequency (calculated using equation 3.4 in section 3.3.2). The direct output (DC out) from the photodiode is obtained by measuring the voltage across the 200Ω resistor. Typically, this is connected to a channel of the oscilloscope and is useful for aligning the photodiode with the laser beam.

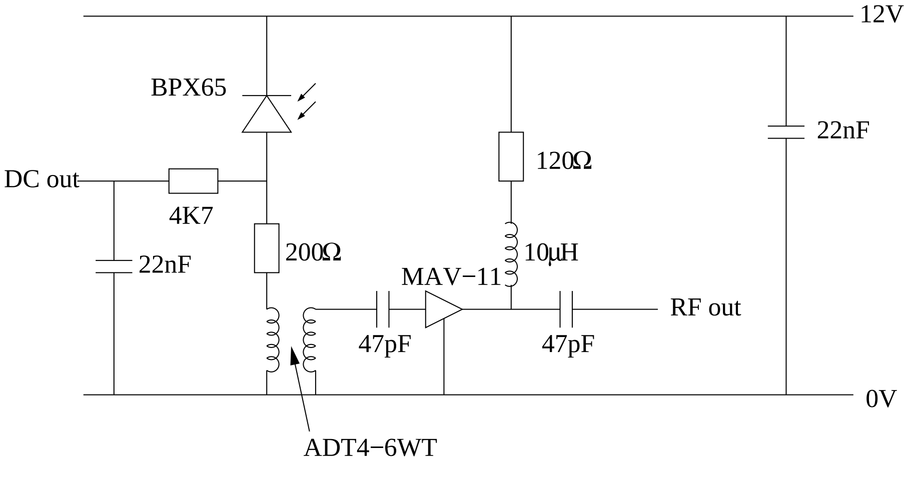

Figure 3.18: Electronic configuration for the single photodiode used to measure the modulated light intensity in the zero order beam caused by a propagating SAW.

3.5 High-speed data acquisition – the analogue electronics

The electronics that are used for the high-speed data acquisition have been described previously in [93], and will be summarised in this section. The purpose of this electronic system is to acquire the amplitude and phase information of the detected ultrasound on the sample at high-speed.

Specifically, 'phase' refers to the difference between the 82MHz components of the detected and reference signals. This system is able to acquire information rapidly, making it useful for producing c-scans and aerial PSFs. In order to acquire the amplitude and phase information, there are three required inputs to the system figure 3.19:

1. Detected signal by the knife-edge detector.
2. The coherent trigger pulse.
3. A reference 41MHz signal.

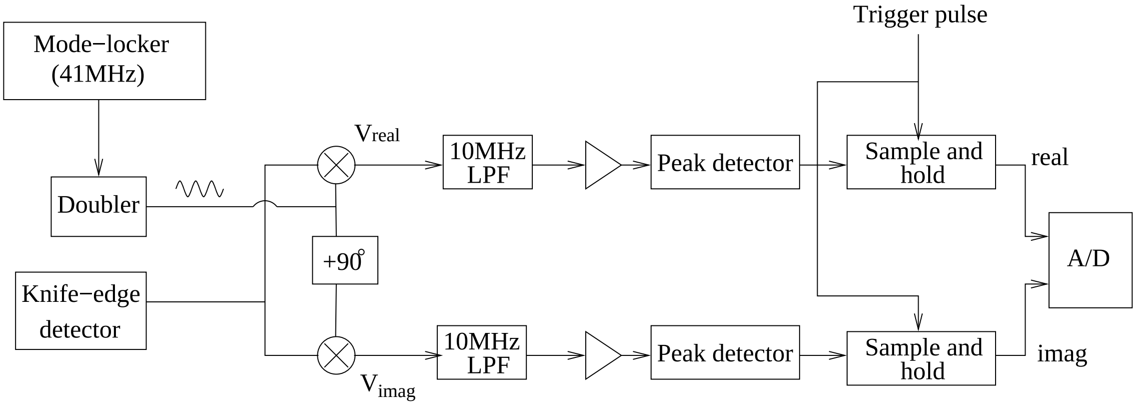

Figure 3.19: Diagram of the analogue electronics required for high-speed data acquisition.

A 41MHz reference signal derived from the mode-locker (and coherent with the laser pulses) is doubled and then mixed with the detected signal from the knife-edge detector. The mixers are used in quadrature generating two output signals V_{real} and V_{imag}, which represent the real and imaginary parts of the the detected signal.

With these two signals, the principle of obtaining the amplitude (A) and phase (ϕ) of the detected signal is shown in figure 3.20 and is calculated using equations 3.29 and 3.30.

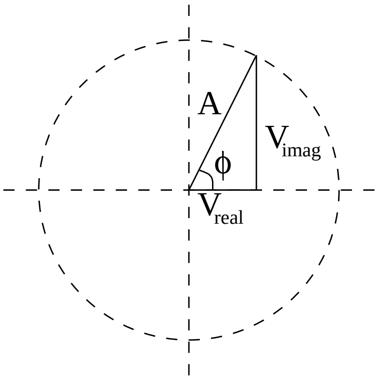

Figure 3.20: The principle of extracting the amplitude (A) and phase (ϕ) using quadrature mixing.

$$A = \sqrt{V_{real}^2 + V_{imag}^2} \tag{3.29}$$

$$\phi = tan^{-1}(\frac{V_{imag}}{V_{real}}) \tag{3.30}$$

In practice, the output of the mixers cannot be used directly, necessitating further electronic processing on these signals (figure 3.19). Both signals follow a duplicate path consisting of a 10MHz lowpass filter, amplification, peak detection, and sample and hold devices. The filter and amplifier components ‘clean’ the signals allowing the peak detector to locate the maximum amplitude. In order for the A/D board to have sufficient time to capture the data, a sample and hold device is required.

3.6 Summary

The generation system used in the OSAM instrument consists of a Q-switched and mode-locked IR laser and a SLM. The fundamental frequency of the generated SAWs is 82MHz, but generating SAWs at the harmonics of 82MHz is possible. Detections of SAWs is performed using a knife-edge detector system. For reference purposes, a guide to aligning the OSAM instrument is included in Appendix C.

The calibration of the detection system has meant that surface displacement can be obtained and from this the stress exerted by the pump SAW can be acquired. The velocity modulation experienced by the probe SAW is presented with respect to surface stress (see Chapter 5). The relationship between stress and velocity modulation provides the measure of material nonlinearity.

Chapter 4

Experimental Method

4.1 Introduction

The OSAM instrument had to be adapted for the integration of the nonlinear experiments. The following three modifications had to be made.

1. A low frequency ('pump') SAW generation system was integrated.
2. Accurate timing electronics were required to control the relative triggering times of the pump and probe SAWs.
3. The effects of temperature variation had to be suppressed.

Since the experiment relies on adjusting the point at which two SAWs interact with each other, an accurate timing control system was constructed to delay the triggering of one source of ultrasound with respect to another. Although this system could set the delay to within an 8ns accuracy but there were additional, albeit relatively minor contributions of timing jitter from other experimental apparatus.

A more significant source of noise compared with the timing jitter was due to changes in ambient temperature in the laboratory. During the course of this work, it was found that velocity variations due to temperature changes were of the same order to the those caused by material nonlinearity. It was crucial to the success of these experiments to minimise the effect of temperature. Two techniques were used to achieve this. Firstly, a highly stable temperature controlled environment was designed and constructed, capable of maintaining the air temperature around certain elements of the experimental apparatus to within ∼0.01°C. Secondly, an adapted data collection technique was developed that suppressed the effect of temperature, typically by a factor of 200.

4.2 Experimental aim and concept

The experiment aimed to measure material nonlinearity by observing a velocity change caused by an applied stress, induced by a low frequency ('pumping') SAW packet in the frequency range 0.5−2MHz. Figure 4.1 shows the stress imposed by a 1MHz wave packet on an aluminium-2024 sample.

The stress exerted by the transducer was calculated by first calibrating the knife-edge detector to acquire the displacement and then using the analysis reviewed in section 1.4.2, to determine the stress. The material properties for aluminium-2024 used in the analysis are shown in Appendix A.

The sample surface experienced maximum stresses at points A and B and zero stress at point C. Previous experiments have shown that applied stress influences the velocity of ultrasound [13]. If a second ('probing') SAW interacted with the pump SAW at positions A, B and C, then the probe SAW would experience a velocity shift depending on these stress levels. The point of interaction between the two SAWs was achieved by delaying the triggering time of the probe relative to the pump.

Figure 4.2 is a trace of a typical probe pulse. The probe pulse envelope had a full-wave-at-half-maximum (FWHM) of 0.4μs and, therefore, instead of seeing a discrete stress level (as figure 4.1 indicates), it actually experienced a range of stresses (over its entire duration) exerted by the pump SAW − approximately 40%

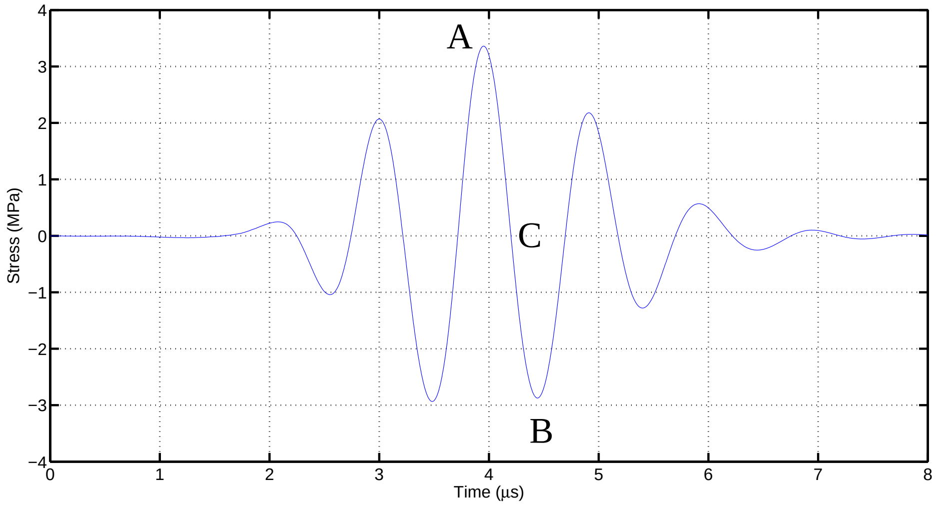

Figure 4.1: Surface stress induced by a 3-cycle SAW generated by a 1MHz transducer on an aluminium-2024 sample. The stress experienced by the probe SAW depends on its point of interaction with the pump – three interaction positions are labelled A, B and C.

of a 1MHz pump cycle. Despite this, it was still possible to measure the velocity shift experienced by the probe. The experimental measurements were, therefore, an ‘averaged’ result over the portion of the pump wave that the probe interacted with. By using a lower frequency transducer, the stress range experienced by the probe pulse would be reduced.

In a truly linear sample, the velocity of the probe pulse would not change with induced stress, i.e. there would be no interaction between the pump and probe waves. In reality, all materials exhibit nonlinearity to a greater or lesser extent depending on their elastic properties.

4.3 Nonlinear experiment configuration

The essential elements of the experimental apparatus that have not yet been discussed are shown in figure 4.3.

A typical interaction distance (also referred to as the arc focal length) for the

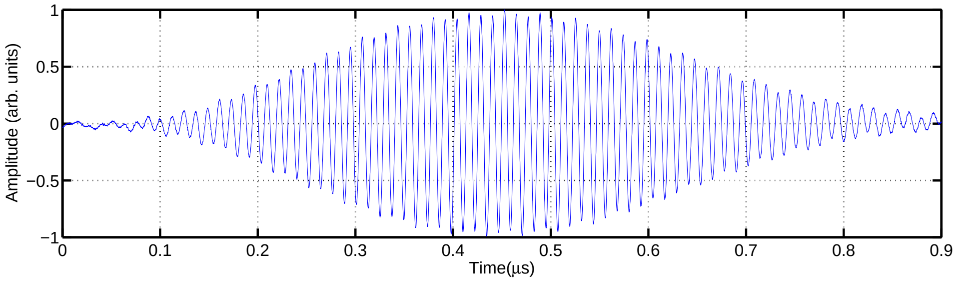

Figure 4.2: Detected probe pulse SAW generated by a Q-switched mode-locked laser and SLM. The experiment required accurate timing so that this signal interacted with various points on the pump SAW packet. By extracting the phase response from this signal at each of these interaction points, there was a direct measure of velocity change with respect to surface stress.

pump and probe SAWs was 4mm and this was strictly taken to be the distance between the centre of the SLM image and the detection point.

The measured phase difference is proportional to the pump/probe interaction distance, and therefore an improved nonlinear measurement would be obtained at longer distances. However, the optimal distance is limited by the SAW detectability (SNR) because the amplitude is diminished by attenuation and aberration. Poor SNR can be overcome by averaging, but this increases the acquisition time of each experiment. Since material aberration is a factor that can limit the interaction distance, correction methods [96], could be incorporated into the experiment to compensate for these effects.

If the interaction distance is very short, the measurement of material nonlinearity is made difficult because the instrumentation would be unable to resolve the very small phase changes in the probe signal. Taking these factors into consideration, an interaction distance of 4mm was appropriate for the fused silica and aluminium samples used in this thesis.

The knife-edge detection system was sensitive to both the pump and probe SAW frequencies. The overall bandwidth of the detector was within a 100kHz to the GHz frequency range. A custom made 82MHz bandpass filter was used (TVC incorpo-

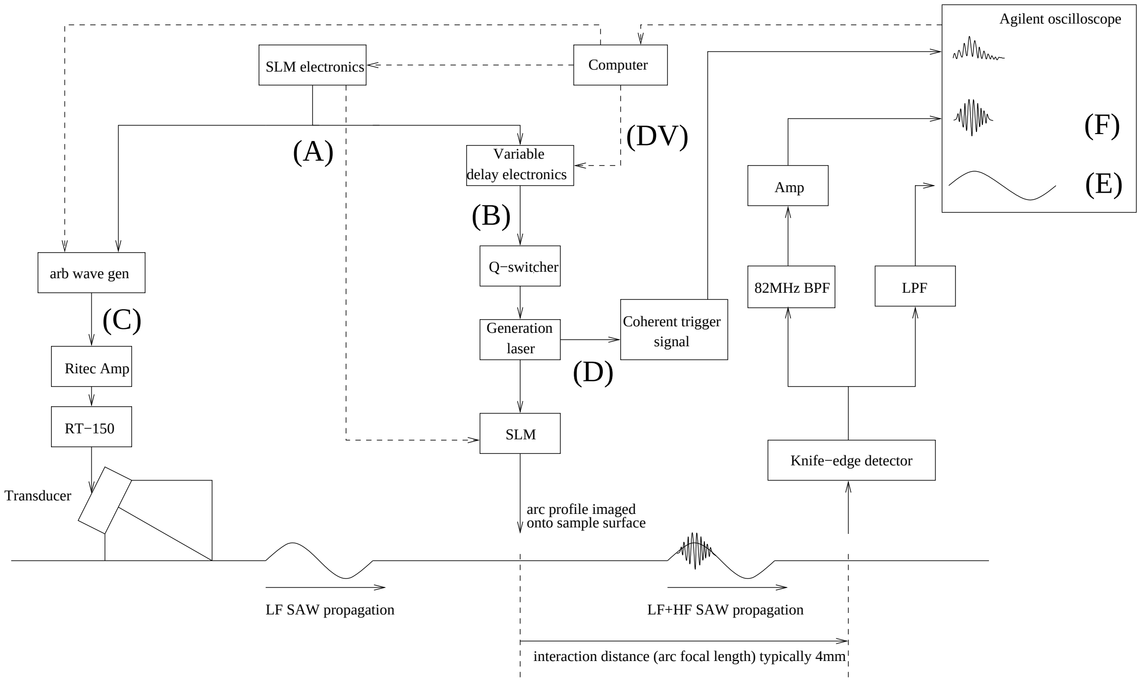

Figure 4.3: Schematic of the nonlinear experiment configuration including the pump and probe SAW generating systems, the delay control system and the knife-edge detector. Letters (A) to (F) and (DV) correspond to figure 4.4 in section 4.3.2.

rated) for these experiments. The Agilent oscilloscope (40GSa/s) was triggered by the coherent trigger pulse, emitted from the generation laser at a rate of 1015Hz. This frequency was governed by the SLM electronics, which provided the master clock for the entire experiment. As the trigger pulse was coherent with the detected 82MHz signal, this allowed accurate recording of the high frequency phase modulations.

4.3.1 Pump SAW generation

A contact transducer was used for all the experiments discussed in Chapter 5. The transducer was attached to a wedge so that a SAW was excited onto the sample surface. The frequency range over which the driving amplifier was most powerful was 0.5−2MHz. NDT-Tech transducers with centre frequencies of 0.5MHz (A414S-SB), 1MHz (A402S-SB) and 2.25MHz (A404S-SB) were used. The transducer, wedge and sample were bonded together with Phenyl salicylate.

The transducer selection was based on its ability to accept high voltage inputs and, therefore, the generation of large displacements (of the order of 20-100nm). Factors such as element size and shape were less important considerations, as the purpose of the transducer was simply to stress the surface of the sample.

The transducer driving signal was generated by the Agilent 33250A arbitrary waveform generator. This device was externally triggered by the timing electronics, and on each trigger event a 3-cycle sine wave with a peak-to-peak amplitude in the range of $0-0.65$V was generated.

This signal was amplified by a Ritec RPR-4000 gated amplifier, which had a gain of 100dB and a peak output power of 8kW. Maximum input voltages to the transducer were 1400V.

4.3.2 Timing setup

The overall ‘speed’ of the experiment was dictated by the repetition rate of the SLM and laser, which was 1015Hz. The digital signal that was generated by the SLM electronics is (by tradition) known as the T/I (true/inverse) signal and this provided the master clock for the entire apparatus (figure 4.4). The T/I signal was a square wave with a duty cycle of 0.5 and a peak voltage of 5V.

The T/I signal was split (A) and the arbitrary waveform generator was triggered directly by its negative-going edge. This then generated a 3-cycle burst (C) at an appropriate frequency for the transducer. The delay electronics also received the T/I signal and generated a new digital signal, referred to as the ‘laser trigger signal’ (B). The electronics consisted of a Spartan 3 Xilinx field programmable gate array (FPGA) board, which was programmed using VHDL code to count down from a given number or ‘delay value’ (DV), determined by the computer. When the count reached zero, it produced a positive edge in the laser trigger signal that triggered the

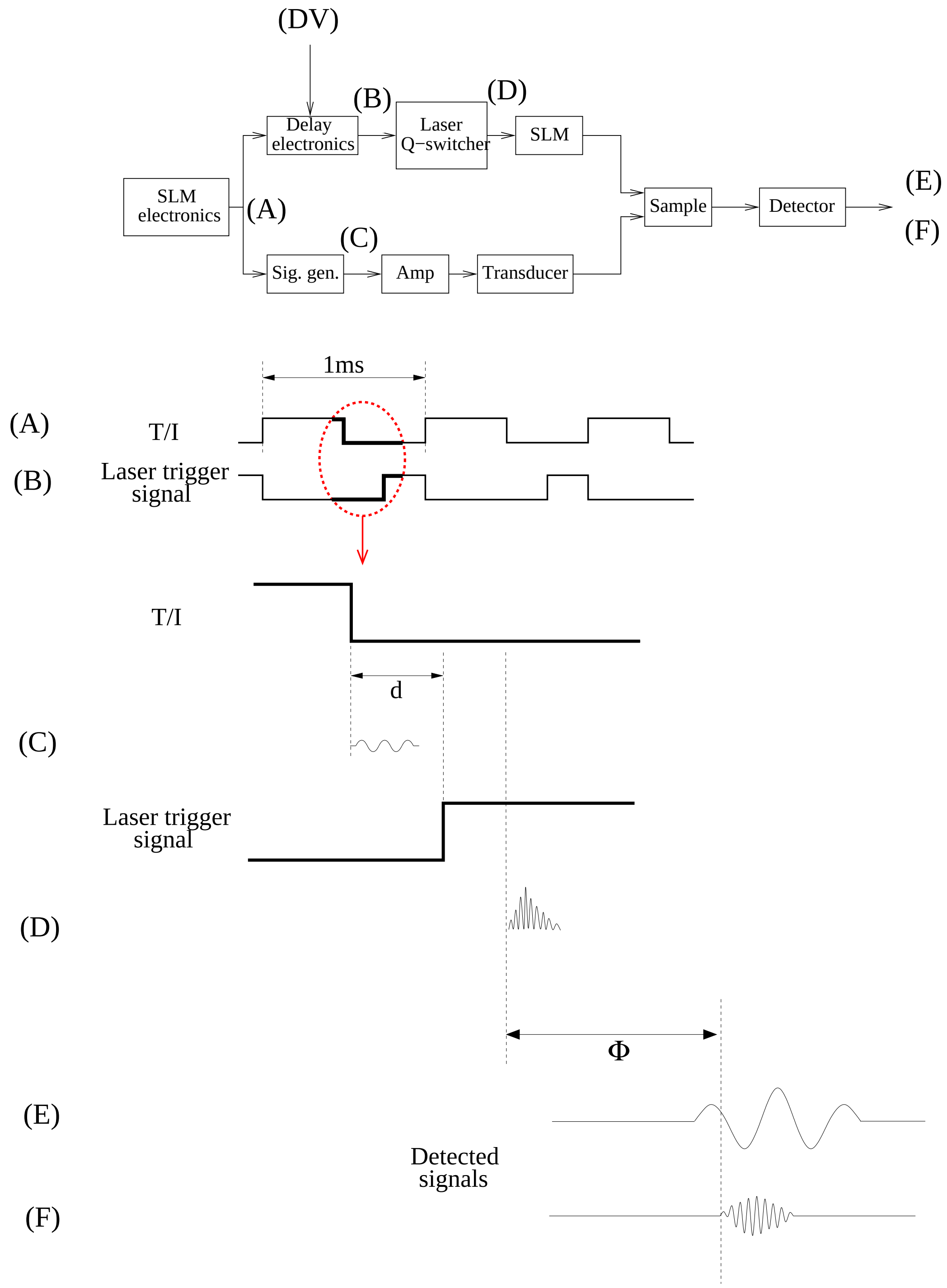

Figure 4.4: Timing setup of the experiment. The SLM electronics generated the T/I digital signal (A) which was used to trigger the signal generator (directly) and also the delay electronics. A delay value (DV) from the computer was used to adjust the time (d) at which the laser was triggered (B) with respect to the signal generator (C). The laser generated a coherent trigger pulse (D) to trigger the oscilloscope. The pump (E) and probe (F) SAWs were then detected and the phase (Φ) of the probe pulse was extracted.

Q-switcher, causing the laser to generate a coherent trigger pulse (D). By adjusting the value of DV, the time delay (d) between the falling edge of T/I (transducer trigger) and the rising edge of the laser trigger signal (laser trigger) was controlled.

The two SAWs that were generated then propagated over the sample, interacting with each other as they propagated and were detected ((E) and (F)). The phase modulation of the high frequency caused by interacting with the low frequency was then measured.

The delay resolution was dependent on the frequency of the clock being used in the FPGA board circuit, and was equal to one pulse of the clock. A 125MHz clock was used so that a minimum delay increment of 8ns was possible. The timing accuracy (jitter) of the delay electronics was also equivalent to one pulse because the clock in the electronics was not synchronised to the rest of the system.

The delay value was a 12-bit number provided by a PCI DIO card in the computer. A single binary increment was equivalent to an 8ns delay. Therefore, the maximum possible delay range was 32.8μs, which was more than sufficient since a typical low frequency wave packet has a duration of 6μs (3-cycle tone burst excites a 0.5MHz transducer).

4.3.3 Experimental timing error

The experiment required critical timing control and, therefore, it is important to discuss the possible impact of two main errors inherent within the system, namely:

1. Timing jitter leading to an error in the phase measurement of the pump.

2. Timing jitter leading to an error in the phase measurement of the probe.

The first issue involves the timing error in the delay electronics and in the firing of the generation laser. The timing error between the input laser trigger signal going high and the output laser pulse (coherent trigger pulse) was measured to have a standard deviation of ∼13ns. Ultimately, the combination of these two errors had an affect on the timing of when the pump and probe SAWs interacted.

The second issue considers the errors involved with triggering the oscilloscope. The coherent trigger signal was used to trigger the oscilloscope because it was synchronised with the detected probe signal and so the phase difference between them could be accurately measured. The amplitude of the coherent trigger signal was not constant and caused an error in the measured phase of the detected probe pulse (figure 4.5).

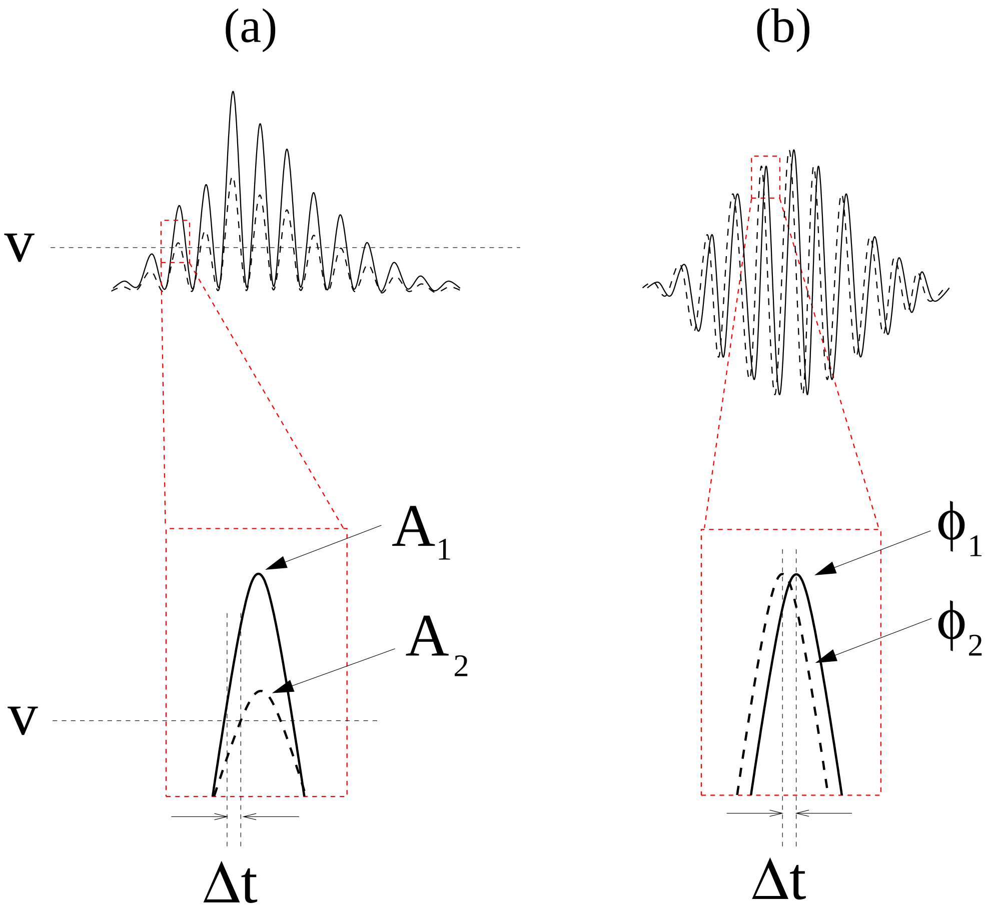

Figure 4.5: Schematic of the oscilloscope timing error. The coherent trigger pulse (a) varied in amplitude (A_1 and A_2), causing the triggering time of the oscilloscope to change by Δt. This affected the measured phase (ϕ_1 and ϕ_2) of the detected probe pulse (b).

More specifically, the oscilloscope triggered on the first spike of the coherent trigger pulse, which was equal to a set voltage (trigger) level (figure 4.5(a)). Depending on the severity of amplitude change, the peak of the first spike may fall below V altogether, or the peak of a preceding spike may exceed V. In either case, the oscilloscope will trigger on a different spike (either the one before or the one after in time) (figure 4.6).

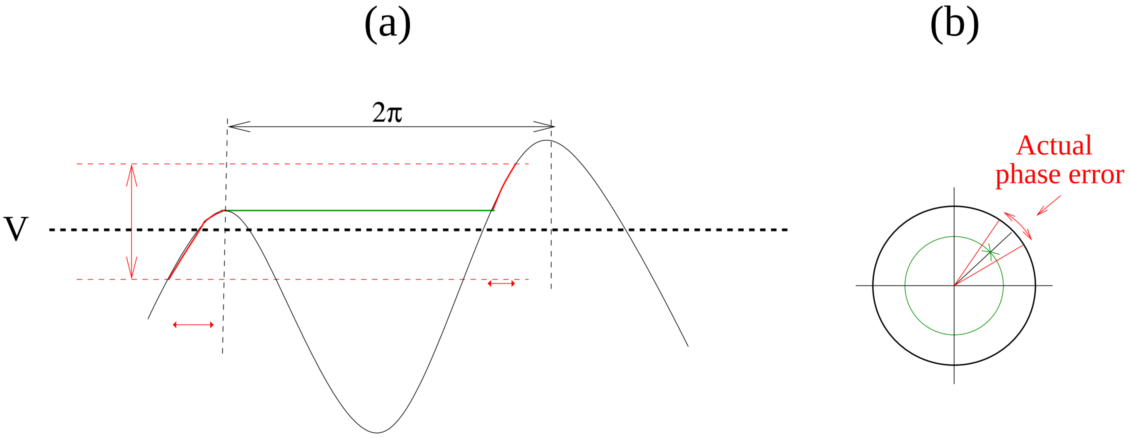

Figure 4.6: When the 'first spike' of the coherent trigger pulse falls below the trigger level (V), the oscilloscope triggers on the adjacent spike (a), causing a 2π phase change in the phase (b).

Although triggering on adjacent spikes does cause a loss of SNR, it is not a concern in terms of detected phase jitter on the detected probe pulse because the phase change equates to 2π and, therefore, causes the phase to wrap round as shown by the green line in figure 4.6(b). The actual phase error is shown by the red line in figure 4.6(b) and is equivalent to 20ps of error.

The degree of error for issues (1) and (2) is dependent on the age of the lamp in the laser. In order to obtain the most stable output from the laser system, the lamp current had to be tuned according to the age of the lamp. To suppress the effects of the timing error and any additional causes of noise, such as the amplifiers used in the knife-edge detector, the detected probe pulse was averaged.

4.3.4 Materials and sample preparation

A number of UV fused silica windows (part: WFS-1006) were purchased from UQG Optics. These samples were disks with a diameter of 100mm and a thickness of 6mm. One side came pre-coated in 200nm of aluminium to make a reflective surface.

In addition, two types of aluminium block (approximately 300×300×6mm) were purchased from Alfa Aesar – Al6061 and Al2024 (parts: 42106 and 42127 respectively). Samples with dimensions of 30×50×6mm were obtained from these blocks and polished on one side.

4.4 Nonlinear/CHOT experiment configuration

The nonlinear experimental configuration discussed in section 4.3, used an SLM and a knife-edge detector to generate and detect ultrasound. This section expands on how CHOTs were incorporated into the nonlinear experiments [94, 97]. The probe SAW is generated by a g-CHOT (figure 4.7(a)) and detected with either a knife-edge detector (figure 4.7(b)) or a d-CHOT (figure 4.7(c)).

The sample used was fused silica and the pump SAW was generated by a 1MHz transducer. Figure 4.8 shows the position of the CHOTs in relation to the transducer on the sample. The approximate distance between the centre of the g-CHOT and the centre of the d-CHOT was 4mm and the transducer wedge was attached to the sample, leaving a 6mm separation distance from the g-CHOT (figure 4.8).

For this experiment, the SLM acted as a mirror and was programmed to reflect all of the light onto the g-CHOT. The light reflected from the SLM illuminated a 3mm×3mm area of the g-CHOT, which excited an 82MHz plane wave SAW.

For both knife-edge and d-CHOT detection configurations, the same 532nm Nd:YAG CW laser was used. Due to the simplicity of the d-CHOT, alterations to the optical setup were minimised when changing from one detection setup to the

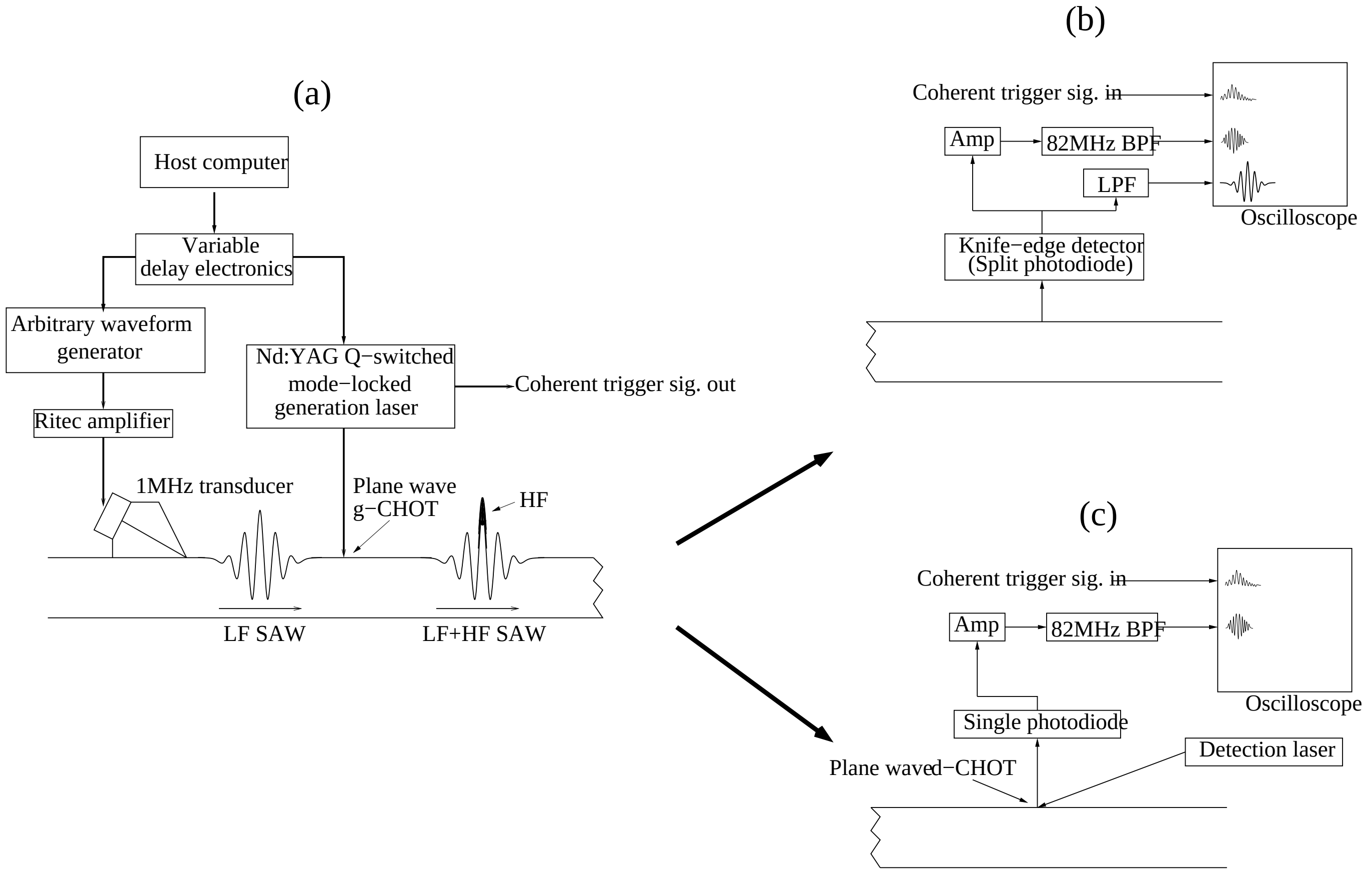

Figure 4.7: Detailed experimental setup using CHOTs. The generation of the 82MHz ultrasound (a) was performed by a plane wave g-CHOT and detected using two different detection systems: a knife-edge (b) and a d-CHOT (c). The low frequency ultrasound was generated by a 1MHz transducer in both cases.

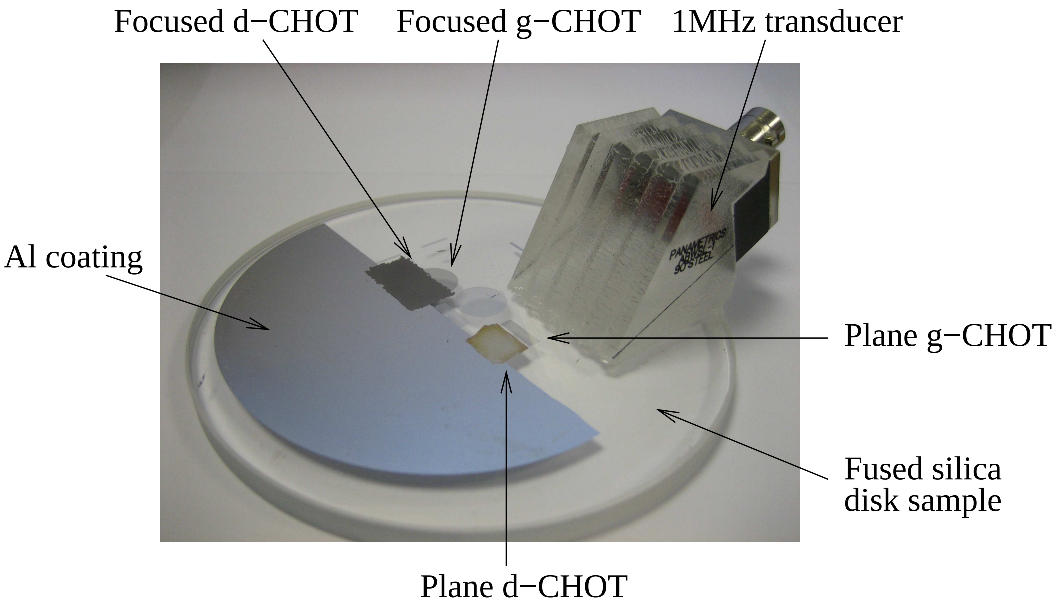

Figure 4.8: A fused silica sample (100mm diameter, 6mm thickness) with several CHOTs. The CHOTs used for the experiments presented in this work are directly in front of the transducer.

other.

4.5 The effects of temperature

Changes in laboratory temperature, even by as little as ±1°C overwhelmed the nonlinear measurements. Temperature change affected the experiment in two ways:

1. Ultrasound velocity is dependent on sample temperature [98].
2. The expansion and contraction of equipment caused changes in the geometrical setup of the apparatus.

To prevent the experimental equipment from overheating, an air conditioning unit was required in the laboratory that was able to maintain a mean temperature of $\sim 25 \pm 1°$C (figure 4.9). The oscillations in the temperature measurements were caused by the unit switching on and off every 10 minutes.

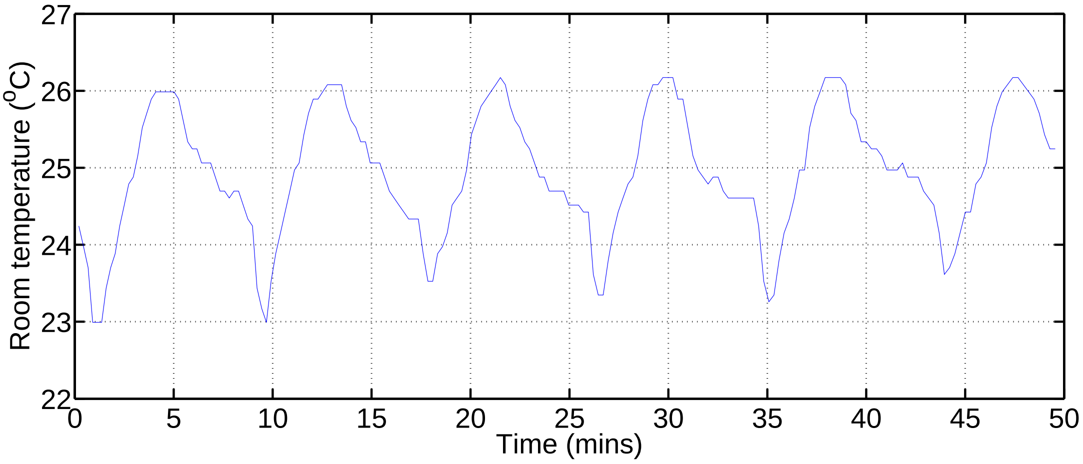

Figure 4.9: Measured room temperature. The oscillations in the measurements were caused by the air conditioning unit regulating the air temperature.

To demonstrate how the changing laboratory temperature affected the results, an experiment was performed using an aluminium-2024 sample. The experiment had a 60-minute duration and the phase of the probe SAW was obtained, along with room temperature (figure 4.9) and sample temperature. The time interval between measurements was approximately 13.5 seconds as this was the time required for the oscilloscope to acquire a single measurement. The sample temperature and measured probe phase are shown in figure 4.10.

A temperature probe was attached to the rear of the sample itself while a second was located in an arbitrary location in the laboratory to measure the air temperature. The sample temperature measurements were accurate to within 0.001°C, while the air temperature was measured with a 0.1°C accuracy. During this experiment, the transducer was turned off, so all the phase modulation was the result of changes in temperature. The probe phase (green line) gradually increased throughout the experiment because the incident laser radiation caused the local sample temperature to rise. In order to demonstrate the high correlation between temperature and phase, the gradient of the phase data was removed (red line). When normalised with the sample temperature, the correlation becomes obvious. Figure 4.11 shows the actual

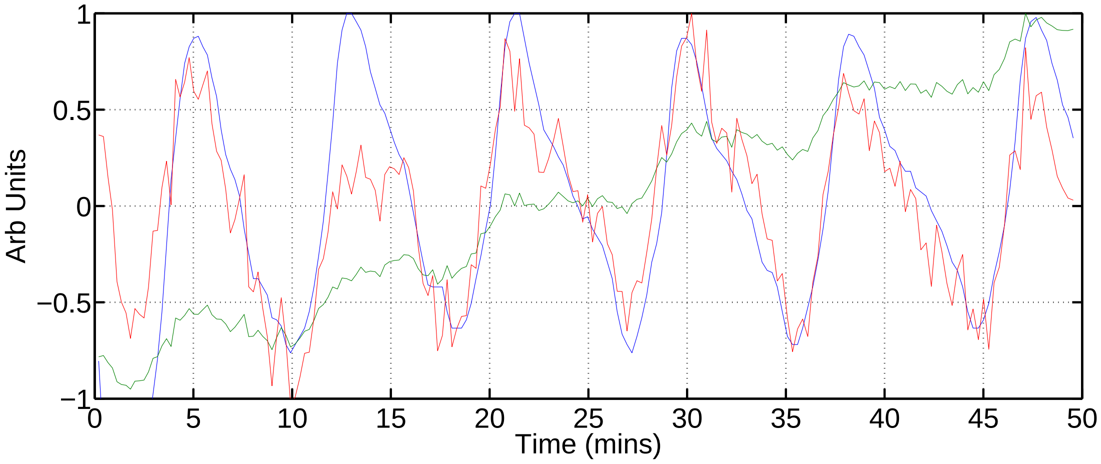

Figure 4.10: Measured sample temperature (blue) and raw phase modulated probe data (green). The gradient of the raw phase data has been removed (red) to show the strong correlation between phase and temperature.

phase throughout the experiment.

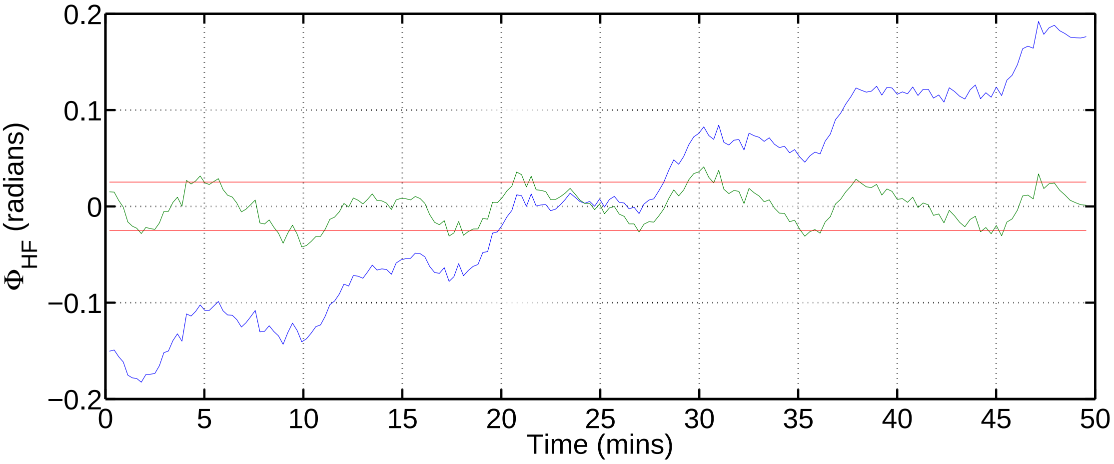

Figure 4.11: Actual probe phase data, before (blue) and after (green) the gradient was removed. When conducting an experiment with the transducer on, the typical phase modulation due to the SAW interaction lay within the limits shown in red.

The oscillations in the phase measurements caused by the temperature variations are approximately ±0.02rads. This was a significant problem because it was found (from experiments presented in Chapter 5) that the phase modulation caused by the material nonlinearity on aluminium-2024 was of a similar order (∼0.0188rads) − indicated by the red lines in figure 4.11. In order to observe the phase modulation caused by the material nonlinearity, the effect of temperature had to be suppressed.

4.6 Suppressing temperature dependence

To minimise the effect of temperature, several suppression techniques were developed.

4.6.1 Temperature control system

Without any temperature control, the experimental apparatus was exposed to the changing laboratory temperature and so the ultrasound velocity was affected by the expansion and contraction of the experimental equipment. The degree of movement experienced by each element in the experimental setup depended on the material type and on its position. For example, elements in close proximity to electronics or heat extractor fans experienced different degrees of temperature variations (and at different times) than elements that were positioned directly underneath the air conditioning unit.

Movement of the SLM head relative to the sample, for example, would cause the SLM image to move on the surface of the sample, thereby affecting the phase measurement. It was vital that the experimental apparatus was protected from ambient temperature variations.

A temperature control system was incorporated into the experiment. This consisted of two temperature controlled enclosures − one placed around the sample, stages and detector system (figure 4.12) and the other placed around the SLM (These are referred to as the 'sample' and 'SLM' enclosures respectively).

The walls and lid of each enclosure were constructed from 30mm thick cavity wall insulation and the internal temperature was regulated by a 33.4W Peltier effect heat pump. A proportional-integral-derivative (PID) controller unit (Supercool: PR-59)

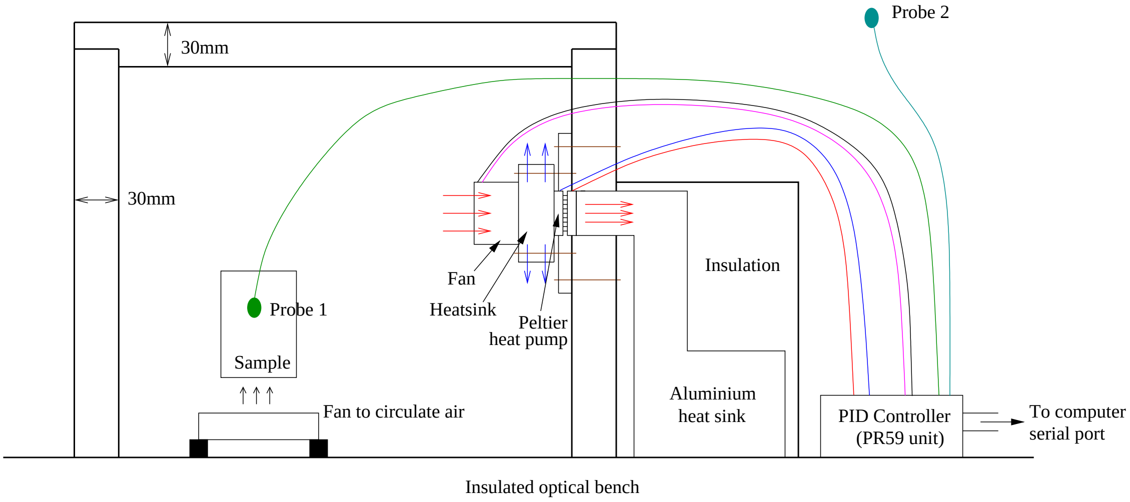

Figure 4.12: The sample enclosure. The temperature probe attached to the sample provided the feedback information for the PID controller. This system maintained a temperature of 26±0.015°C inside the box, while outside temperatures typically varied between 24−26°C.

was used to control the magnitude (and direction) of the Peltier's current and was programmed by the computer via an RS-232 port. Air was circulated in the box, using a fan to blow air across the fins of a heatsink attached to the Peltier. A second fan located below the sample helped prevent the sample surface temperature from rising due to heat from the incident laser beam.

On the other side of the Peltier, a large aluminium block was attached and bolted to the optical bench, which together, acted as a very large 'thermal load' or heatsink. Insulation was placed around the aluminium heatsink so that variations of outside temperature were heavily damped.

The optical bench underneath and surrounding the enclosures was thermally insulated, as the large surface area and high thermal conductivity of the bench meant that it was very efficient at coupling the air inside to the air outside the enclosures.

Where possible, the equipment that produced heat (e.g. CCD camera and electronics) were not contained within the enclosures so that the power demand on the temperature control system was minimised. Devices that could not be removed from the enclosures included the SLM, knife-edge detector electronics, and four mechanical stages. The 2W of IR radiation from the laser also acted as a further heat source.

An initial experiment was performed to investigate the effect of changes in temperature on the phase of the detected probe signal on an aluminium sample. The temperature in the box was increased over a duration of approximately 10 minutes and probe phase measurements were acquired at a rate of one per 13.5s (figure 4.13).

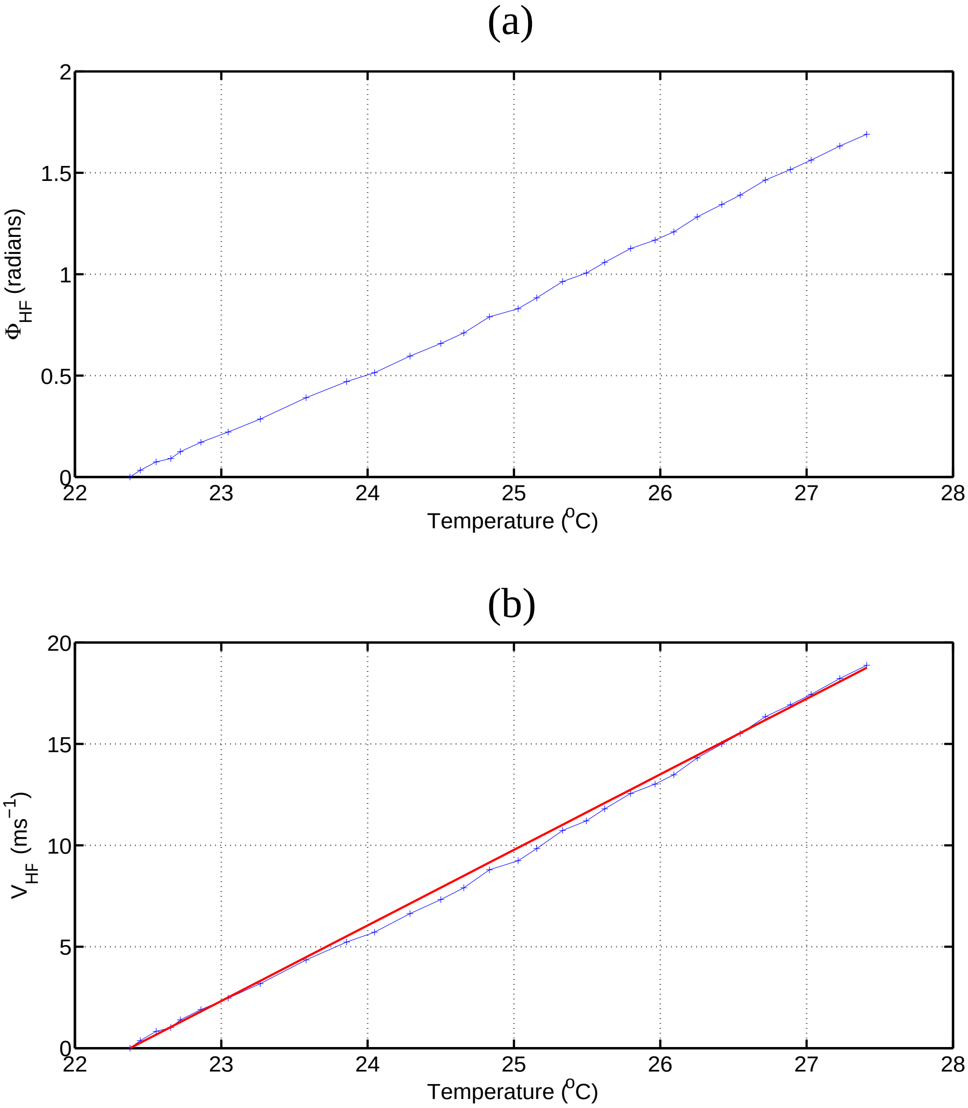

Figure 4.13: Phase (a) and velocity (b) of the detected probe SAW as the temperature in the box was increased. A line (red) has been fitted to the velocity results. The gradient of the line is $3.7\text{ms}^{-1}/°\text{C}$.

The results from figure 4.13(b) show that the measured velocity change with respect to the temperature in the box can be estimated to be 3.7ms^{-1}/°C.

To demonstrate the capability of the temperature control system to suppress changes in ambient laboratory temperature, an experiment was performed in which the target temperatures were set at 26°C and 27.1°C in the sample enclosure and SLM enclosure. Over a 50-minute time period, probe phase measurements and temperature readings were recorded (figure 4.14).

Although the temperature readings taken from the sample (figure 4.14(b)) and SLM (figure 4.14(c)) enclosures both showed small effects of variations in ambient temperature, these were very much reduced, compared with having no enclosure at all. The temperature in the sample enclosure was within a range of ±0.015°C, and a ±0.05°C temperature range was maintained in the SLM enclosure.

Slight indications of temperature variations in the probe phase modulation results were also still present (figure 4.14(d)), although they had been heavily suppressed, compared with the unregulated environment (figure 4.11).

The ramping up of the phase was caused by the incident laser energy on the sample (figure 4.14(d)). Theoretically, there must be a point where the temperature of the sample would reach a steady state. This would have taken an extremely long time, depending on the size and material of the sample, and it would have been impractical for the laser to be on for many hours before running a nonlinear experiment which might only take 20 minutes to perform.

Furthermore, after opening the enclosure (to make adjustments to the optics or replacing the sample, for example), it took at least 20 minutes for the temperature in the enclosure to re-stabilise (figure 4.15), which proved to be an inefficient method of performing experiments.

The phase measurements were still increasing even after 60 minutes and until the system reached a steady state, an experiment could not be performed. Therefore,

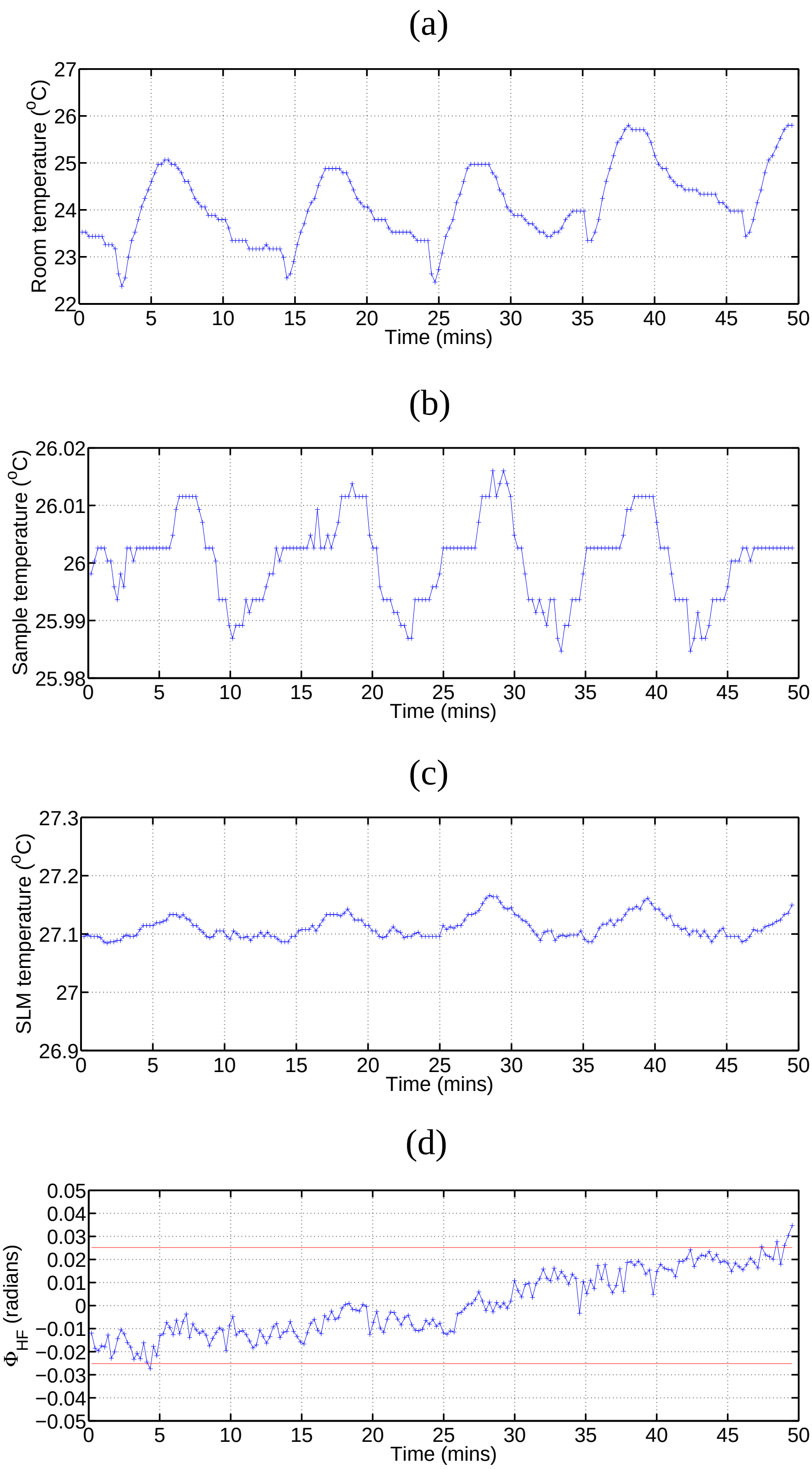

Figure 4.14: Measured laboratory (a), sample enclosure (b) and SLM enclosure (c) temperatures. The probe phase measurements are shown in (d) and the red lines indicate the limits of the modulation caused by material nonlinearity.

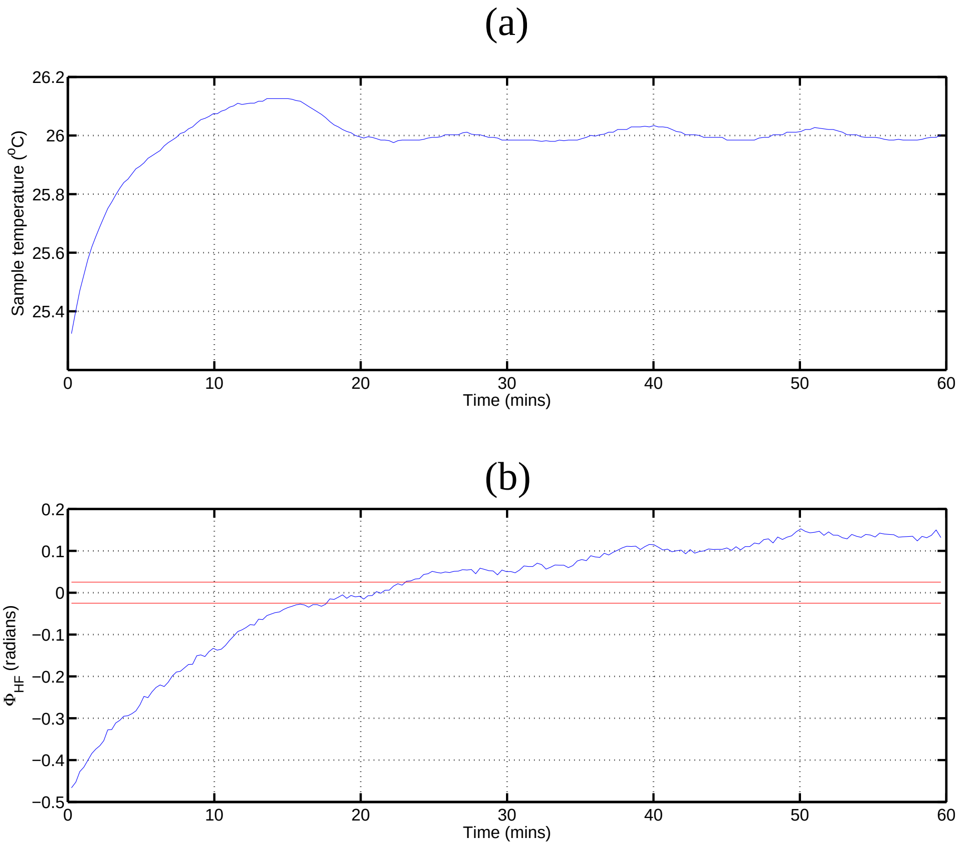

Figure 4.15: Response of the PID controller to a sudden change in temperature. Sample temperature (a) and measured probe phase (b) after temporarily removing the enclosure lid (the lid was replaced at t=0).

alternative and more efficient temperature suppression techniques were developed.

4.6.2 Differential data acquisition

The differential data acquisition technique was used to improve temperature suppression by incorporating a ‘reference’ delay setting so that after every given interaction point (‘target’ delay) with the pump SAW, the delay would return to the reference point. It is vital that both the target and reference sets of data experienced similar temperatures and, therefore, highly correlated. The phase difference ($\Delta\Phi_{HF}$) between the target and reference data should eliminate the effect of temperature variation, leaving the modulation caused by the pump SAW.

To demonstrate the differential data acquisition technique the transducer was not turned on but the temperature and phase measurements were recorded over a period of 50 minutes (figure 4.16).

The laboratory temperature variations (figure 4.16(a)) were still observed in the reference and target measurements (figure 4.16(b)). However, the phase difference between the data sets (figure 4.16(c)) showed only slight variations, which were heavily damped. Furthermore, the overall phase difference remained stable throughout the course of the 45-minute experiment and showed no evidence of ramping-up (figure 4.16(c)).

Slight variations still exist because it is not possible to acquire the target and reference data simultaneously. Therefore, there is a temperature difference between taking the reference and target data. To lessen the effect of temperature further, using this method, the time difference between obtaining the reference and target data would have to be reduced. Although this could be achieved by reducing the number of averages/measurement, the subsequent loss of SNR would be undesirable. Therefore, an alternative method was developed.

4.6.3 Interlacing differential data acquisition

With the interlacing differential data acquisition method, the reference and target data are acquired simultaneously (figure 4.17). This method interlaces the reference and target data by switching between them at a relatively high speed ($\geq$10Hz). Thus, as the average temperature at the times of taking the reference and target data is highly correlated, the mean temperature difference between measurements is minimised. Two channels of the oscilloscope were used simultaneously − one for the reference data and the other for the target data.

Two switches (S1 and S2), were operated by the same 5V square wave. An inverter (I) placed before one of the switches meant that only one of these switches could be on at a single moment in time. The switching waveform came directly from

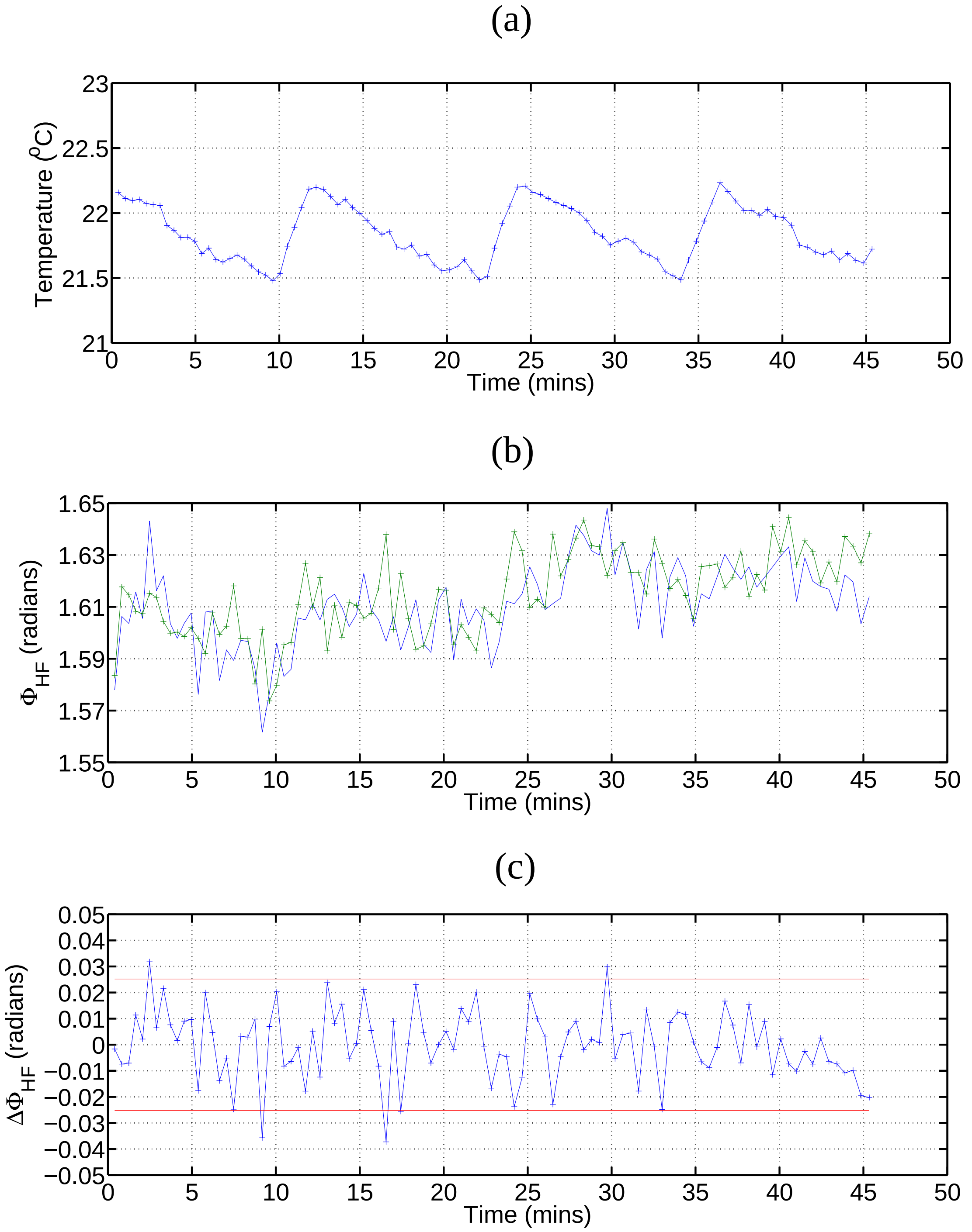

Figure 4.16: Laboratory temperature (a), phase measurements at the target (blue) and reference (green) delays (b) and phase difference ($\Delta\Phi_{HF}$) is shown in (c).

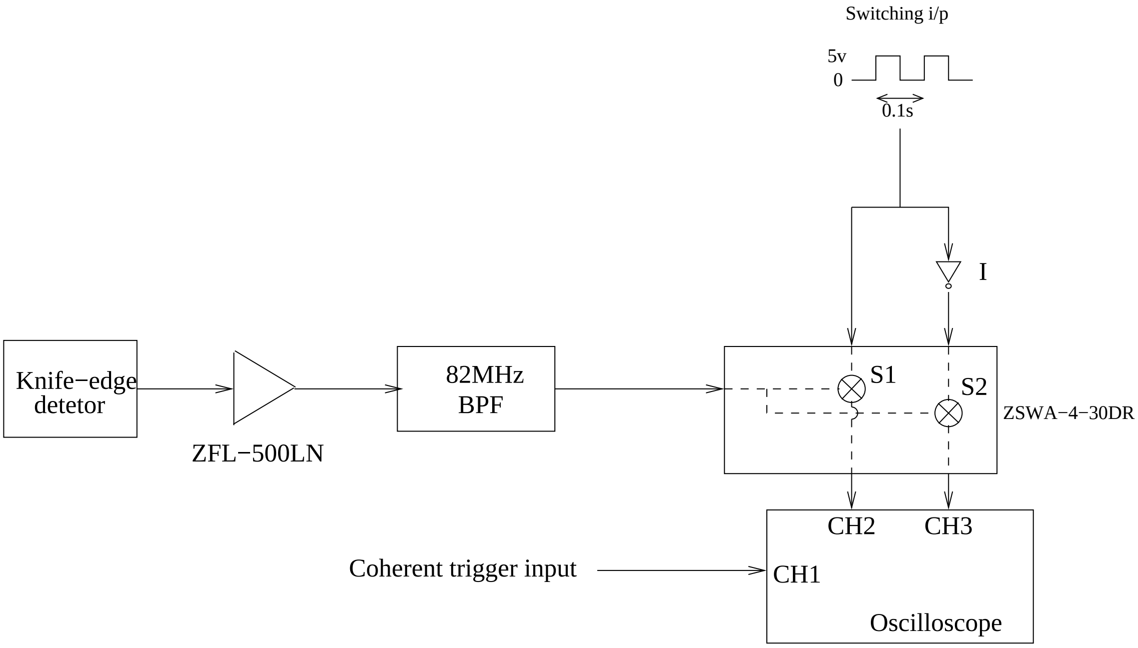

Figure 4.17: Electronic configuration for the interlacing differential data acquisition technique.

the delay electronics.

When S1 was on only channel 1 of the oscilloscope received a signal. The timing electronics were programmed so that in this state, the delay was set to the reference delay. When S2 was on, only channel 2 received a signal and in this second state, the target delay was used. The oscilloscope required 32 seconds to average both channel 1 and channel 2 simultaneously. Once complete, the phase difference between the two waveforms was acquired. The process was then repeated but with a different target delay.

An alternative approach to using two channels of the same oscilloscope would be to use two oscilloscopes. The advantage of dual oscilloscope acquisition is that the duration of the experiment would be reduced because the data collection rate would be faster. However this approach was not implemented, due to a limited number of available oscilloscopes.

The ability of the interlacing differential data acquisition method to suppress the effects of temperature was investigated (figure 4.18). The interlacing frequency was

50Hz and the transducer remained off for the duration of the experiment.

Over the 25 minutes the phase difference remained stable and within limits in which nonlinearity could be measured (shown in red, figure 4.18(c)).

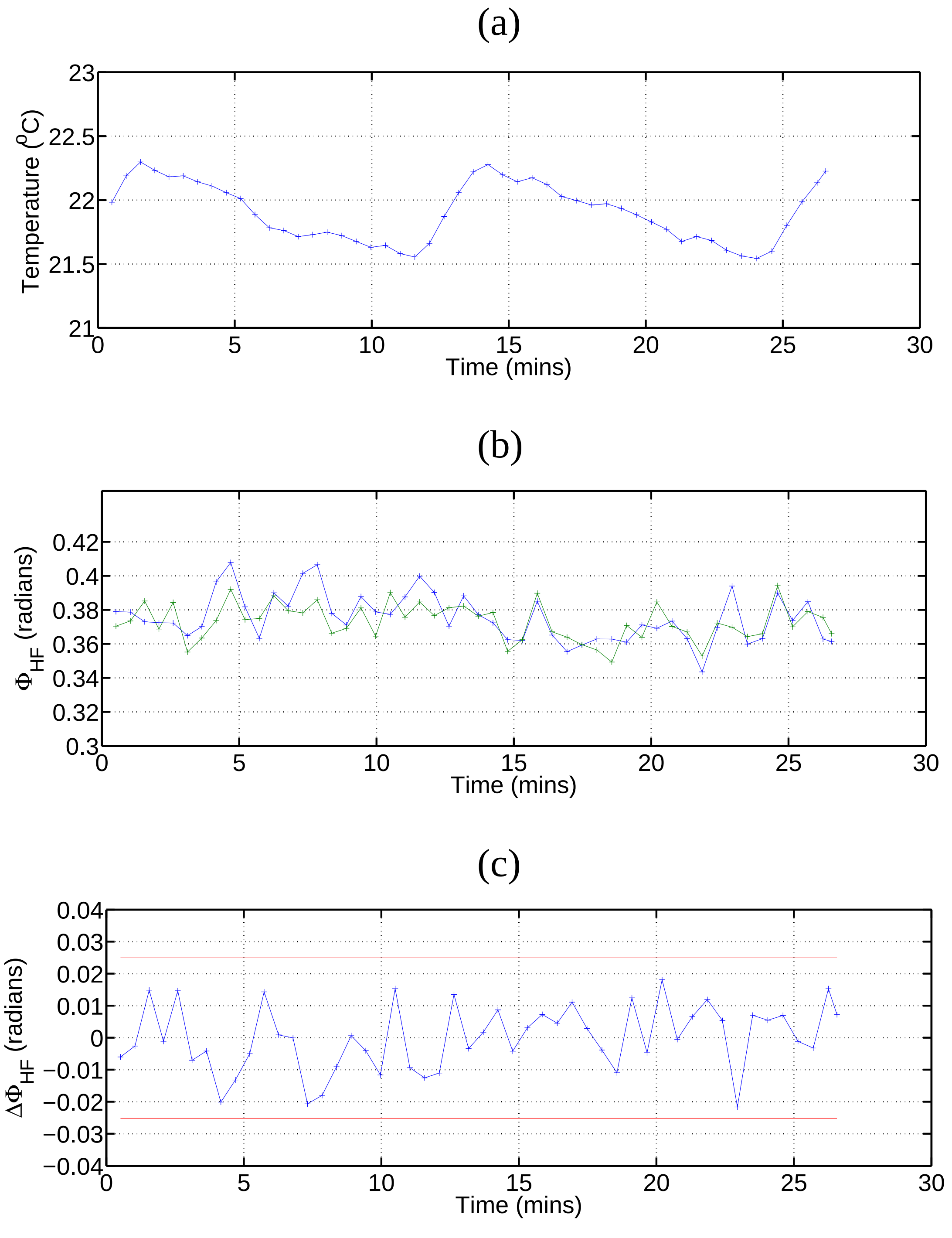

Figure 4.18: Laboratory temperature (a), phase measurements at the target (blue) and reference (green) delays (b) and phase difference ($\Delta\Phi_{HF}$) is shown in (c). The switching frequency of the data collection electronics was 50Hz.

4.6.4 Interlacing differential data acquisition with temperature control

Either of the differential data collection techniques can be used in conjunction with the temperature control system and may result in enhanced temperature suppression. The effects of combining the temperature control system and the interlaced differential data acquisition techniques on maximising temperature suppression were investigated.

There was a marked improvement in noise level by using this combined approach compared with each technique alone (figure 4.19). A quantitative comparison of all the temperature suppression techniques is provided in section 4.8.

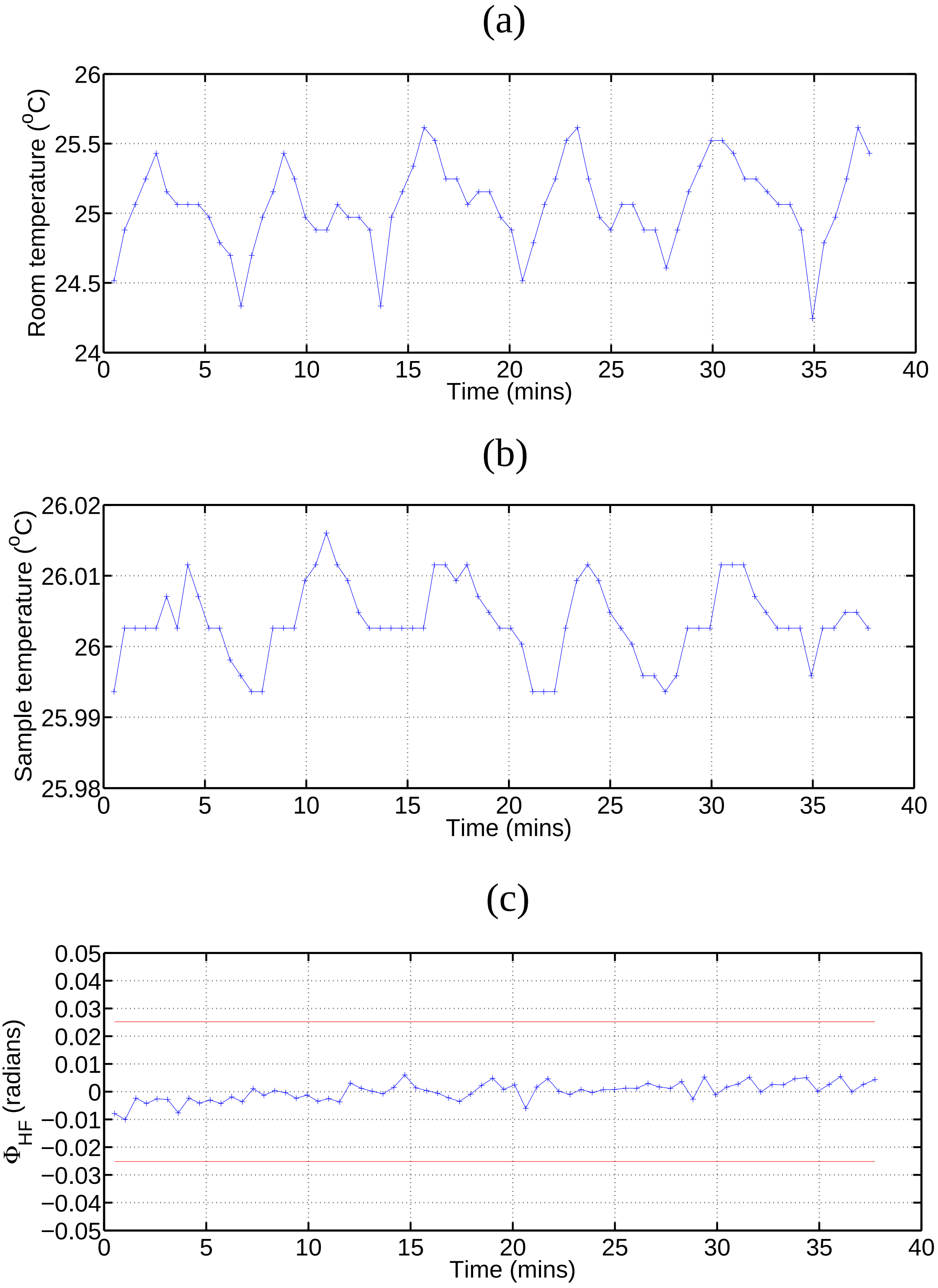

Figure 4.19: Laboratory (a) and sample (b) temperatures. The measured phase difference is shown in (c). The switching frequency of the data collection electronics was 50Hz.

4.7 Comparison of temperature suppression techniques

The temperature control system was successful in reducing the effect of the changing laboratory temperature, but it did have the disadvantage of making experimental times relatively long compared to the other suppression methods. The reason for this is because the temperature in the enclosure had to stabilise before an experiment could be performed.

This was not the case for the differential and interlaced differential techniques which provided a robust and instantaneous means of acquiring data. Both were more successful than the temperature control system in suppressing the phase modulation caused by temperature variations (figure 4.20 and table 4.1).

By using a combination of the temperature control and interlaced differential techniques, the noise caused by temperature variations was further reduced. This combined approach would be particularly useful when working with difficult materials such as titanium, in which SNR is worse than with aluminium, for example. The results presented in chapter 5 were acquired using the interlaced differential data acquisition method only.

Technique	Standard deviation (rads)
None	0.1030
Temperature control	0.0139
Differential	0.0133
Interlacing differential	0.0103
Interlacing differential with temperature control	0.0033

Table 4.1: The standard deviation in phase measurements for the corresponding temperature suppression techniques shown in figure 4.19.

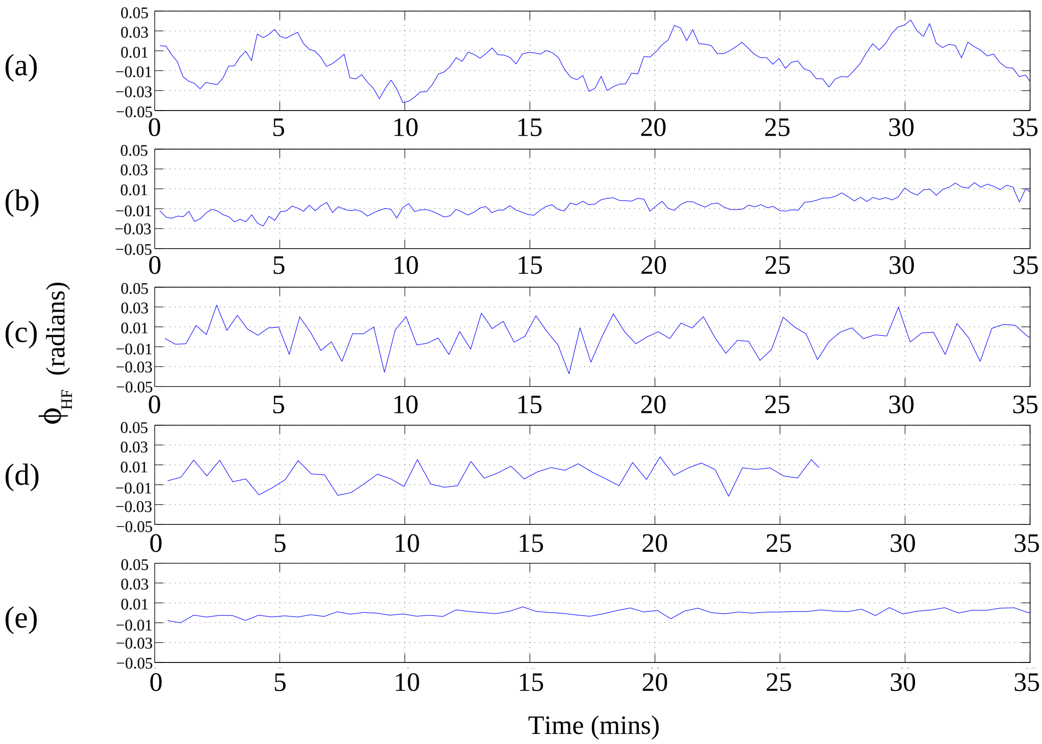

Figure 4.20: Measured phase difference from each of the temperature suppression techniques. No control (a), temperature control system (b), differential data acquisition (c), interlaced differential data acquisition (d) and a combination of temperature control and interlaced data acquisition (e).

4.8 Summary

In order to perform nonlinear experiments, a number of modifications had to be made to the OSAM instrument, which includes the integration of: the pump SAW generation system, the timing control electronics and a robust method of suppressing the effects of temperature on the measurements.

The pump SAW system consisted of a transducer bonded to the sample and the timing control electronics controlled the interaction point of the pump and probe SAWs to within an 8ns accuracy. Changes in ambient laboratory temperature had a large impact on the probe phase. Room temperature changes of ±1°C were causing phase changes that were of the same order as the nonlinear measurements. A number of temperature suppression techniques were developed. The most appropriate technique was the interlaced differential data acquisition method, because it provided adequate suppression of the temperature effect and was immediately effective − unlike the temperature control system.

CHOTs provide an alternative method of generating and detecting ultrasound and have the fundamental advantage over the SLM/ knife-edge detector configuration in that they drastically simplify the optical setup, as well as offering a robust and compact method of performing the nonlinear experiment.

Chapter 5

Experimental Results

5.1 Introduction

Fused silica and aluminium are reported to have a relatively high nonlinearity property compared with titanium for example [4]. Therefore these materials are suitable for the initial development of a nonlinear experiment.

The purpose of the experiment, described in section 5.3, was to verify that the observed measurements were caused by the material nonlinearity and not caused by an artefact of the experiment. The effect of using different pump SAW amplitudes on the experiment is described in section 5.4. Experiments using several pump:probe frequency ratios are also demonstrated in this chapter. In section 5.5, pump SAWs at 0.5MHz, 1MHz and 2MHz were mixed with an 82MHz probe pulse and the measured phase modulation in the probe pulse was compared. In addition, to demonstrate that the nonlinear experiment can be performed using different probe SAW frequencies, three experiments were conducted and discussed in section 5.6. Here, a 1MHz pump SAW interacted with an 82MHz, 164MHz and 246MHz probe SAW and the results were compared. In section 5.7, the nonlinear response of aluminium-2024, aluminium-6061 and fused silica were compared.

5.2 Extracting the phase

The raw data consists of a number of detected probe SAW signals that have interacted with various points (due to the delay settings) of the pump's wave packet and have therefore experienced some degree of phase modulation. Typically, 20000 points were used for each trace, providing a time resolution of 0.1ns/point, which was an adequate resolution to extract the phase of the probe signal. The phase was extracted by taking the fast Fourier transform (FFT) of the received signal and within the frequency spectrum, the point that corresponded to the 82MHz component was located. The phase at this point was then converted to a velocity.

Results herein are presented in terms of velocity-stress graphs and the gradient of the velocity-stress data provides a measure of the material nonlinearity. The gradient was calculated using the method of least-squares. The error in the gradients was also established, based on the statistical spread of the data.

5.3 Validation of nonlinear measurement – the 'anti-propagating' test

It was important to confirm that the phase changes being measured were purely caused by the pump-probe SAW interaction and not by an experimental artefact, such as signal crosstalk or electronic noise. The 'anti-propagating' test was performed to rule out any concern of whether the pump SAW signal had not been completely filtered out by the 82MHz bandpass filter and, therefore, was influencing the probe signal phase measurements.

When the pump and probe SAWs co-propagated, the probe pulse interacted with a single point of the pump SAW and experienced a constant stressed state. When the two SAWs propagated in opposite directions, they did so over different parts of the sample surface, in which case the probe SAW did not experience a constant stress.

In the co- and anti- propagating experiments (figure 5.1), the detection electronics were subjected to exactly the same signals – the only difference between them was the degree of pump-probe interaction. It was expected that the measured phase would be different in each experiment.

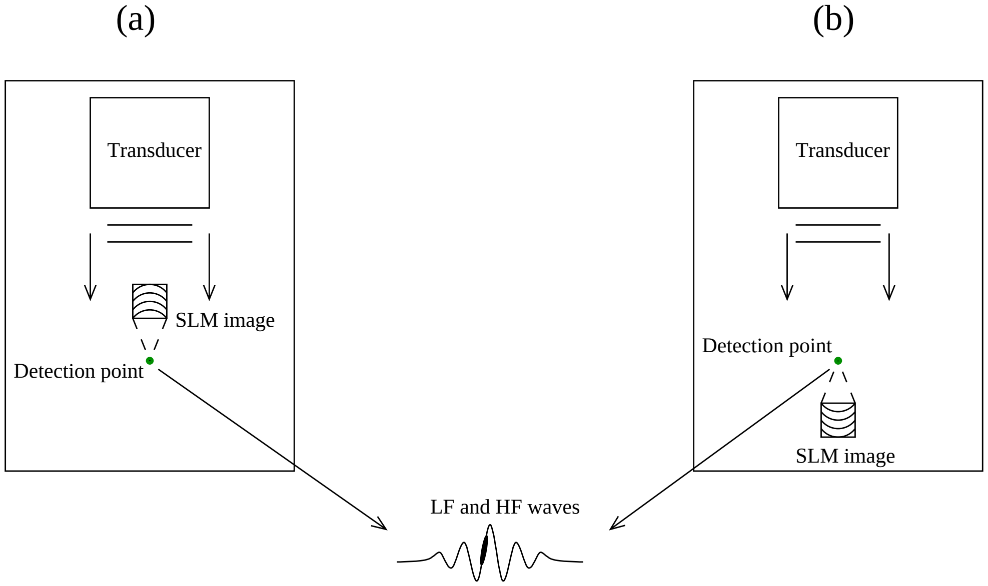

Figure 5.1: Pump and probe SAWs co-propagate (a) and anti-propagate (b). The SLM image (arc profile) is rotated to direct the probe SAW in the desired direction. In both setups, the arc focal length (interaction distance) is 4mm and the distance between the transducer and detection point is the same.

As the SLM image position was fixed in space due to the design of the OSAM instrument, the sample and detector had to be manoeuvred into the appropriate positions for each experiment. In both experiments, the transducer was the same distance (2cm) from the detection point. The SLM image was 4mm above or below the point of detection for the co- and anti propagating experiments. Since the distances between the transducer, SLM image and detection point were the same in both cases, the same delay settings were used. An 8μs delay range, with a delay step of 80ns was used so that the probe pulse interacted with multiple points of the pump SAW packet.

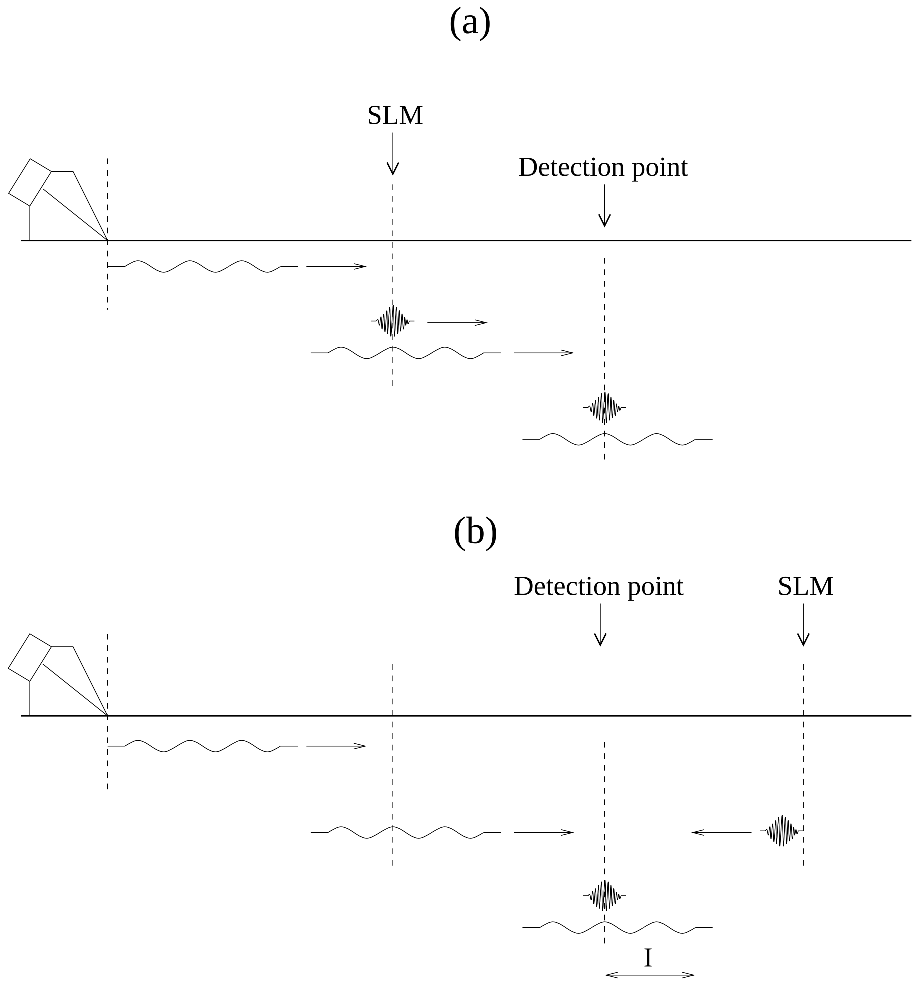

Figure 5.2: In the co-propagating experiment (a), the probe interacts with only one position of the pump. In the anti-propagating experiment (b), the probe interacts with a range of stresses exerted by the pump (indicated by I). The portion of the pump packet that the probe interacts with depends on the delay setting.

In the co-propagating configuration (figure 5.2(a)), the laser was fired at the appropriate time so that the probe SAW interacted with the second peak of the pump wave. When the two waves arrived at the detection point, the probe had experienced a single stressed state and was phase-modulated accordingly.

In the anti-propagating setup (figure 5.2(b)), the pump and probe were triggered (as before) and since they both propagate over the same distance (4mm), they arrived at the detection point as shown − where the probe is located on the second peak of the pump. In getting to this position, the probe had interacted with a portion of the pump wave (indicated by I). This means the probe had experienced all the stresses imposed by this portion of the pump wave. The measured phase of the probe was, therefore, an averaged phase change caused by all of these imposed stresses (figure 5.3).

Using the experimental setup in section 4.3, different electronic channels were used for detecting the pump and probe signals. Consequently, the two signals experienced different delays. This meant that it was not possible to accurately determine the precise location of the probe SAW relative to the pump. Therefore, an arbitrary phase was applied to the results in figure 5.3 so that they coincide with their respective interaction points on the pump SAW packet.

The co-propagating experiment showed a clear correlation between the interaction points and the phase-modulated measurements. In the anti-propagating experiment, the phase modulation appeared to be barely above the noise level. There is clearly a difference between the results from the two setups, confirming that the phase-modulation experienced by the probe SAW is caused by the material nonlinearity and not by an experimental artefact.

5.4 Changing the pump SAW amplitude

To observe the pump-probe interaction, the approach used in section 5.3 altered the triggering delay between the two SAWs so that the probe experienced multiple stress states imposed on the sample by the pump SAW. In this section, the stress imposed by the transducer on the sample was changed by controlling the amplitude of the pump wave and the corresponding probe phase modulation was measured. Only two delay settings were required − a reference and a target delay − and using the interlaced differential data acquisition method, the delay alternated between the two settings at a rate of 50Hz.

The most appropriate reference and target delay settings for this experiment

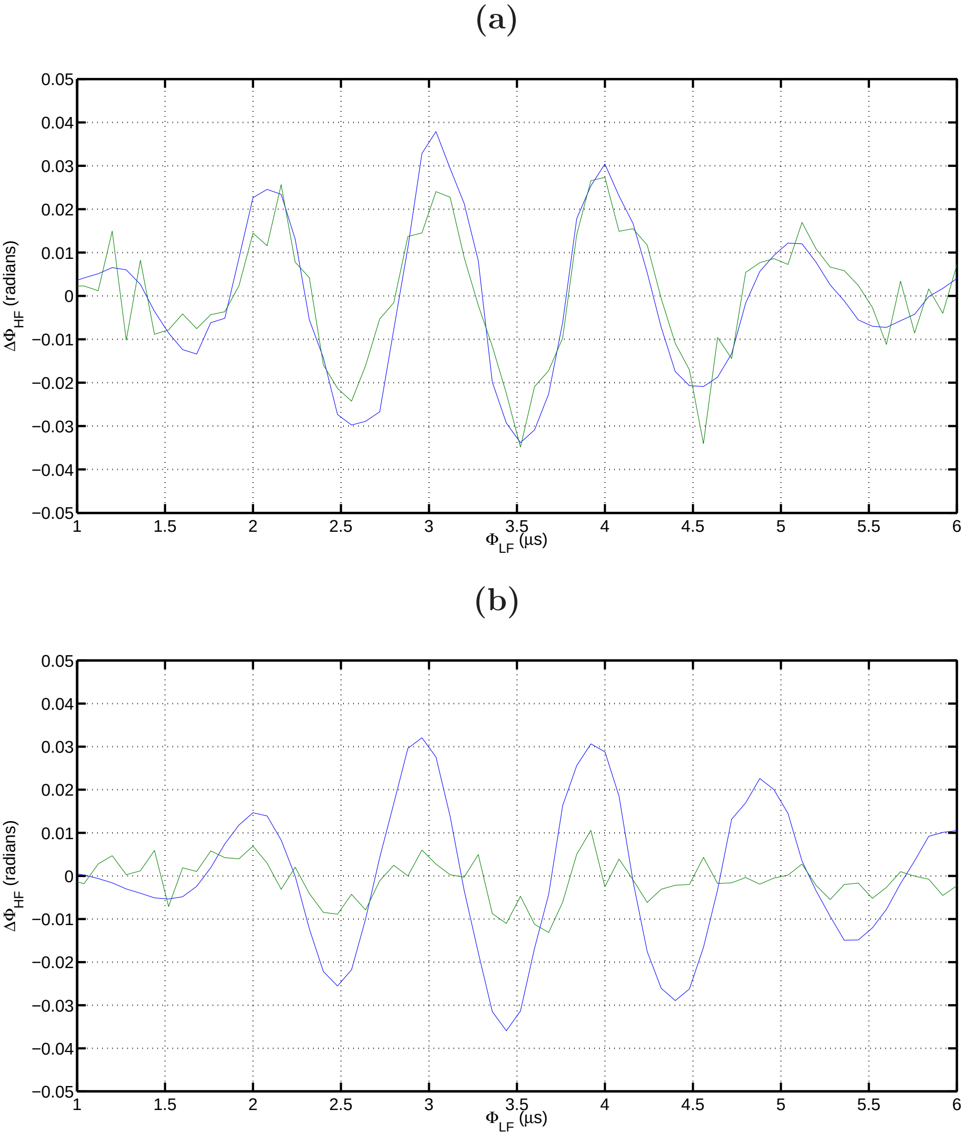

Figure 5.3: Probe phase modulation (green) when interacting with the pump SAW packet (blue) as the two SAWs are co-propagating (a) and anti-propagating (b).

were those that corresponded to the maximum and minimum stress levels imposed by the pump wave. However, since the detected pump and probe signals had different electronic paths, a procedure was developed to overcome the difficulty of accurately establishing which delay values corresponded to these interaction positions.

5.4.1 Selecting appropriate delay settings

The points of maximum and minimum stress are at the peak and trough of the pump wave and have half a cycle difference, in terms of time. The time difference between the reference and target delays was fixed at 0.5μs (since a 1MHz transducer was used) and both delays were incremented so that the probe pulse interacted with the pump wave. The phase modulation experienced at each of the reference and target delays is shown in figure 5.4.

The two delays that provide the greatest contrast in terms of phase modulation are measurements 25 and 31 (REF and TAR, respectively), and are the most appropriate ones to use. It would be unwise to use the delay settings at measurements 28 and 34 because this would result in little or no stress contrast, regardless of the pump SAW amplitude, thereby making the experiment unsuccessful. A trace was obtained to show the probe SAW location relative to the pump SAW at delay measurements 25 and 31 (figure 5.5).

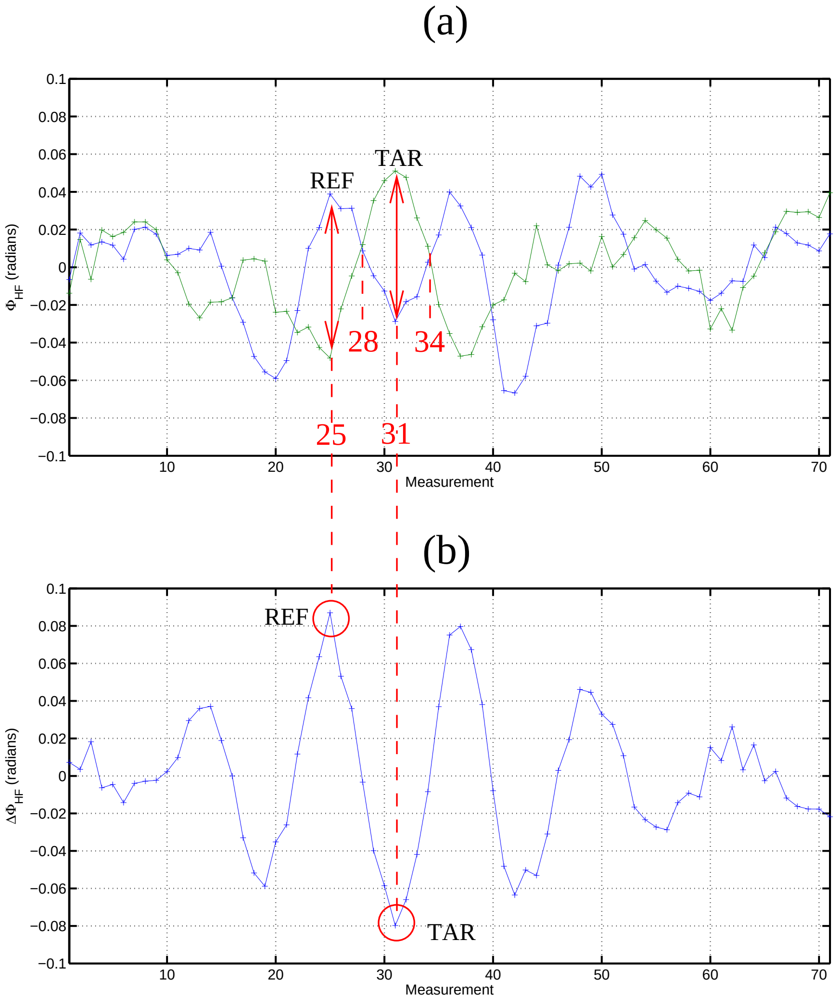

Figure 5.4: Probe SAW phase modulation at reference (blue) and target (green) delays, as they interacted with different points on the pump SAW packet (a). The probe phase difference is shown in (b). The points with maximum phase (i.e. stress) contrast between them are labelled REF and TAR.

The knife-edge detector is sensitive to sample tilt and the point of maximum stress (and displacement) is measured as the point of maximum gradient. This is why the probe pulse appears to be interacting with the rising (REF) and falling (TAR) parts of the pump wave, rather than at the peak and the trough (figure 5.5). Whether there is a +90° or −90° phase difference between the actual displacement and the knife-edge measured displacement is a question that is discussed further in section 5.7.

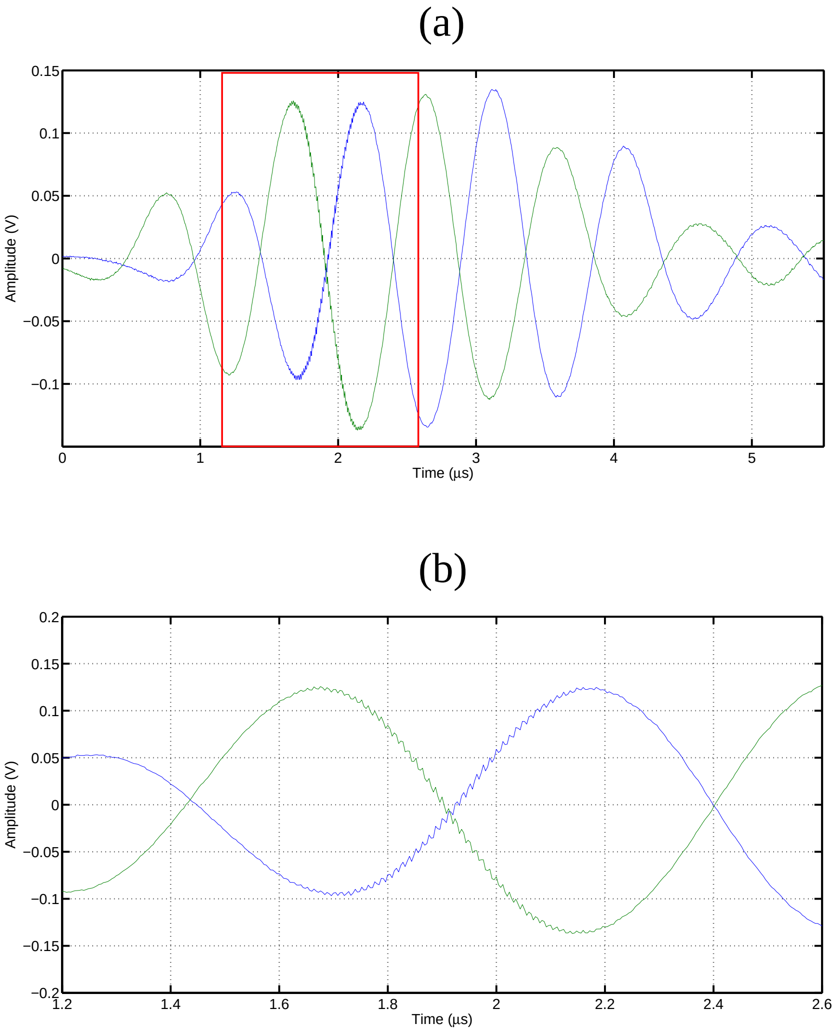

Figure 5.5: Knife-edge detection of the mixed pump and probe signal at REF (blue) and TAR (green) points (a). A close-up of the region highlighted by the red box is shown (b).

5.4.2 Experimental procedure and results

Now that the two delay settings had been established, the actual experiment could be performed. The arbitrary waveform generator produced a 3-cycle 1MHz sine wave. The peak-to-peak voltage amplitude output from the waveform generator was computer-controlled and was increased from 0.02V to 0.64V in steps of 0.02V. The detected pump/probe signals at 6 of these amplitude settings are shown at the reference delay (figure 5.6(a)) and target delay (figure 5.6(b)).

Using the knife-edge calibration technique from section 3.3.3, the peak-peak pump SAW displacement was obtained (figure 5.6(c)) and is plotted against amplifier input. The vertical black lines in figure 5.6(a) indicate the points that were used in the calibration algorithm (although for clarity only 6 pairs are shown − indicated by the red circles. Each pair represents the peak and trough points at each amplitude setting). The red circles in figure 5.6(a) correspond with those in figure 5.6(c).

The phase-modulated results at the reference and target delays were plotted against displacement (figure 5.7(a)) and the difference between the reference and target data with respect to surface displacement is shown in figure 5.7(b). To find the velocity-stress relationship, the phase results were converted to velocity and displacement results converted to stress (figure 5.7(c)).

The velocity difference (ΔV_{HF}) between the reference and target delays increases with stress figure 5.7(c)) and the rate of increase is determined by the gradient of the red line that has been fitted to the data. Using the least-squares method [99], the line gradient was calculated to be $112.8 \pm 5.4 \text{mms}^{-1}/\text{MPa}$. The velocity-stress gradient is a direct measure of the material nonlinearity and is dependent on the material type and level of material fatigue.

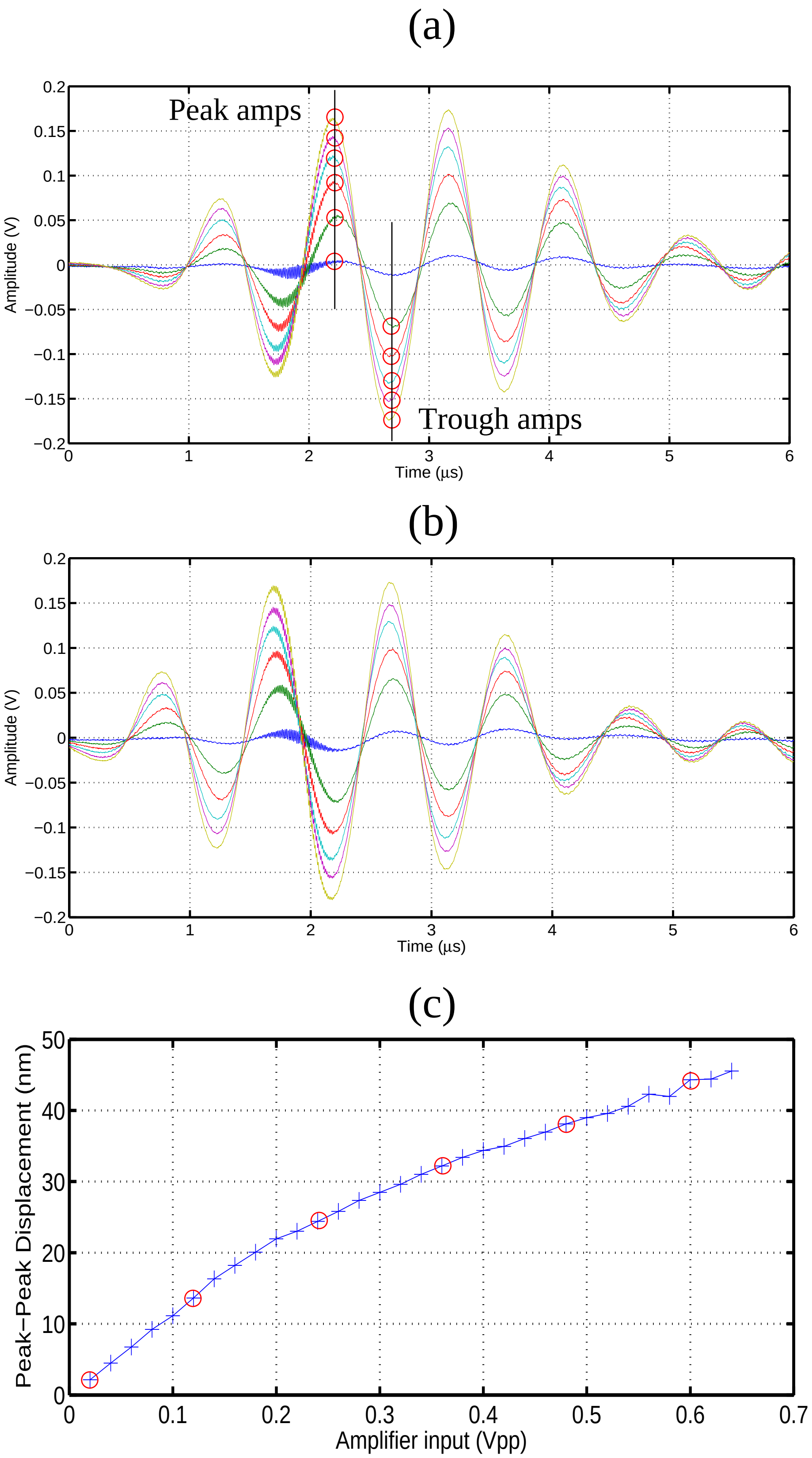

Figure 5.6: Example pump/probe detected signals at various pump amplitude settings at the reference (a) and target (b) delay settings. The surface displacements measured at increasing input voltages to the amplifier are shown (c).

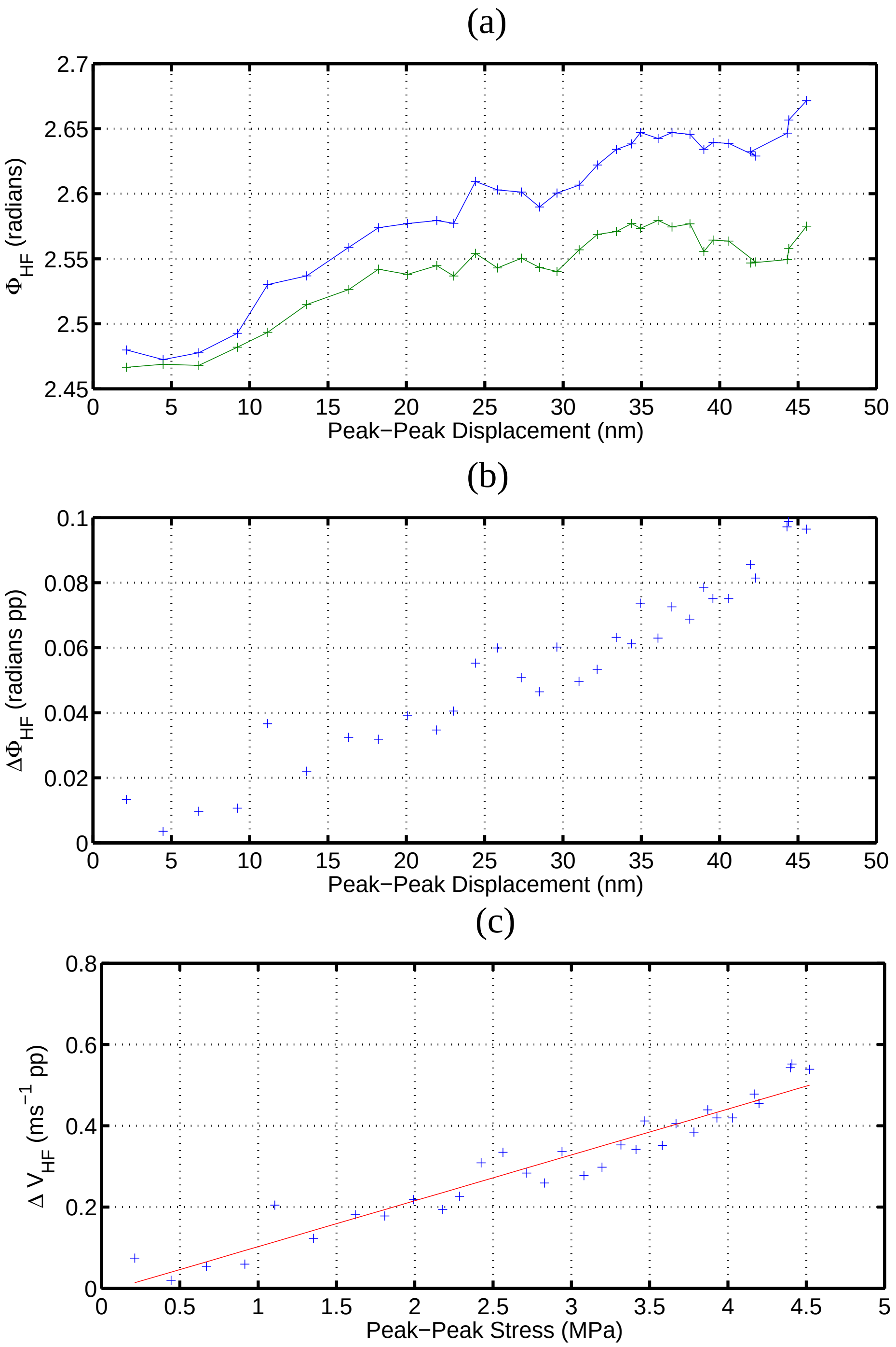

Figure 5.7: Phase modulation at REF (blue) and TAR (green) interaction points with corresponding surface displacement caused by the pump SAW (a). Differential probe phase modulation with corresponding surface displacement caused by the pump SAW (b). The corresponding velocity and applied stress is shown in (c).

5.5 Changing the pump SAW frequency

For a given displacement, the applied stress (σ_{xx}) at the surface of the sample is proportional to the frequency of the pump SAW (figure 5.8).

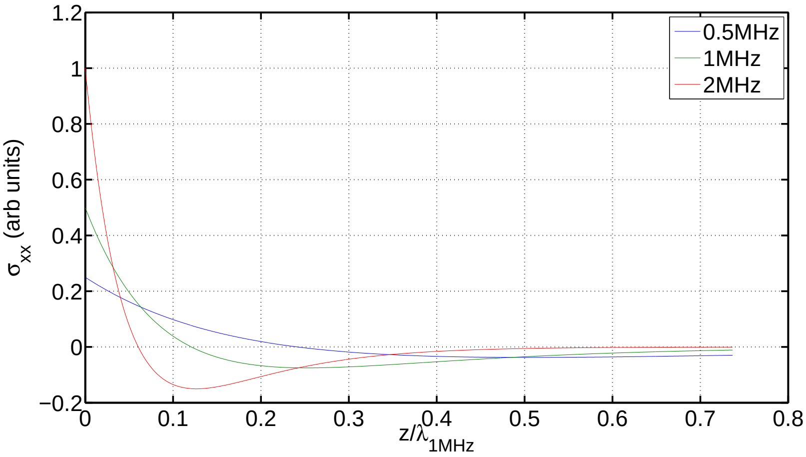

Figure 5.8: Stress (σ_{xx}) against sample depth (z) at a constant displacement for three different SAW frequencies. At the surface, the applied stress is proportional to the SAW frequency. The stress has been normalised to the 2MHz data.

To further investigate this effect, a number of transducers were used to generate the pump SAW on a fused silica sample. The operational bandwidth of the RPR-4000 amplifier was 100kHz to 10MHz, however, the maximum power range (8.1kW root-mean-square [RMS]) was between 0.5MHz and 2MHz. Transducers with centre frequencies of 0.5MHz, 1MHz and 2.25MHz were, therefore, used for this investigation and were excited by a 3-cycle sinusoidal burst at frequencies of 0.5MHz, 1MHz and 2MHz, respectively. In each case, the probe SAW was delayed in time so that it interacted with multiple points of the pump SAW. The phase of the probe SAW at each interaction point was then extracted (figure 5.9). The delay increments were 160ns, 80ns and 40ns for the 0.5MHz, 1MHz and 2MHz pump SAWs, respectively, and the interaction distance was 4mm for all experiments. In each case, the raw phase results shown in blue in figure 5.9 have been filtered by a digital bandpass filter to reduce noise content and are shown in red. The green line is the pump wave, which has been normalised with the phase measurements. At each frequency, there is a clear correlation between the phase measurements and the corresponding pump SAW wave packet.

The unfiltered phase data from figure 5.9 has been plotted against displacement in figure 5.10(a). In figure 5.10(b), the phase measurements have been converted to velocity and lines have been fitted to these data (figure 5.10(c)).

In order to compare the three sets of data, the results were plotted in terms of velocity and stress (figure 5.11(a)). Although the velocity-stress gradients are expected to be the same for all cases, the value obtained for the 0.5MHz SAW pump frequency was higher than those from 1MHz and 2MHz frequencies (table 5.1).

SAW pump Frequency (MHz)	Gradient (mms^{-1}/MPa)
0.5	139.3±3.9
1	122.4±5.1
2	126.5±10.4

Table 5.1: Velocity-stress gradients acquired from figure 5.11(b) for different pump SAW frequencies.

The reason for this discrepancy was because the output from the 0.5MHz transducer was not constant over the duration of the experiment.

For these nonlinear experiments it is important to acquire both the pump and probe traces at each delay, so that the probe phase modulation can be related to surface stress. A single experiment was performed in three parts.

1. Detect pump and probe simultaneously for setting up appropriate delay range.
2. Acquire probe signals at each delay.
3. Acquire pump signals at each delay.

Parts (2) and (3) were not performed simultaneously because in order to obtain the best possible SNR when measuring the probe pulses, it is favourable to minimise any unnecessary splits in the detection channel. Therefore, to acquire the probe

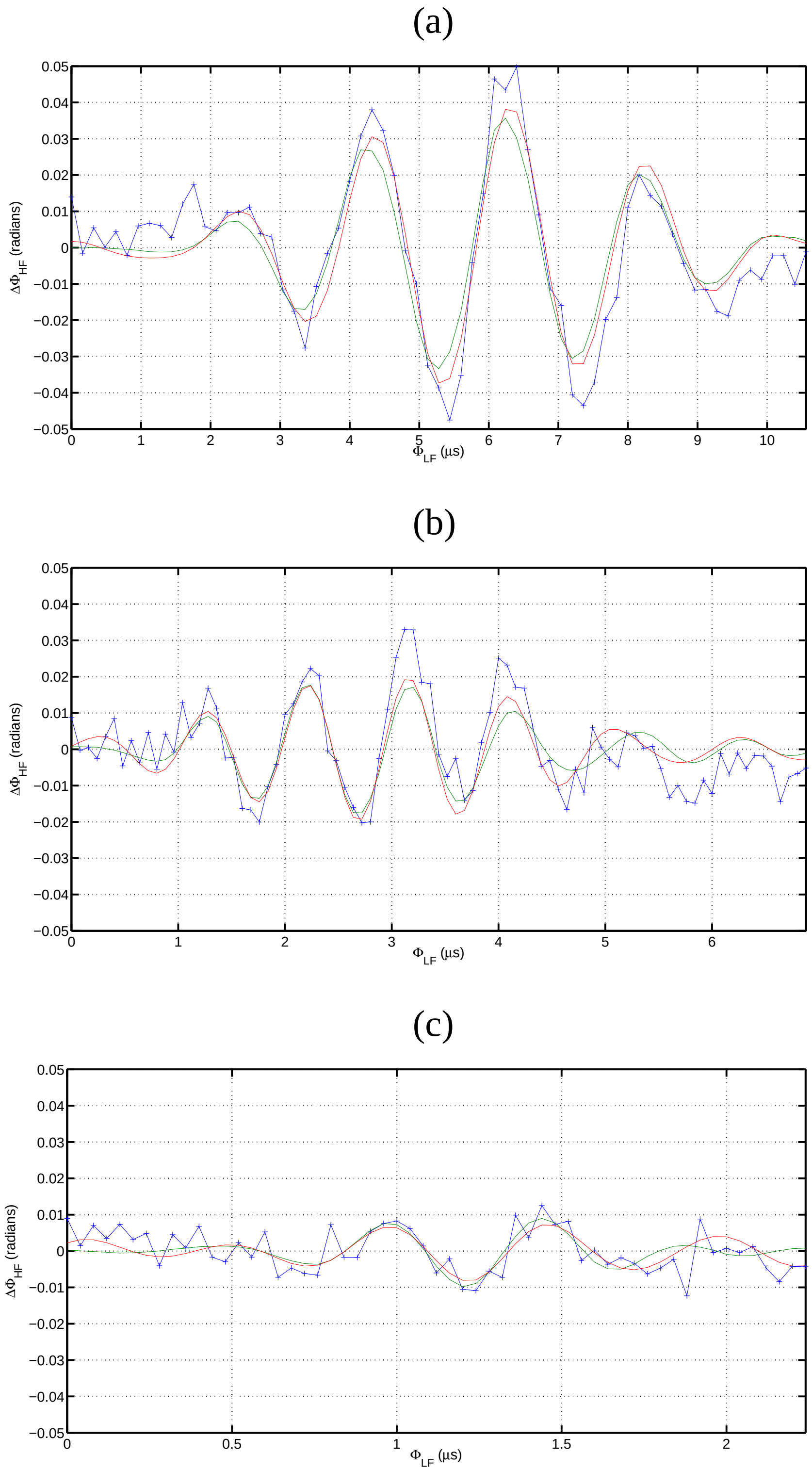

Figure 5.9: Experimental phase-modulated probe measurements on fused silica (blue) when interacting with the 0.5MHz (a), 1MHz (b) and 2MHz (c) pump SAW packets (green) on fused silica. In each case the data have been digitally filtered in MATLAB (red).

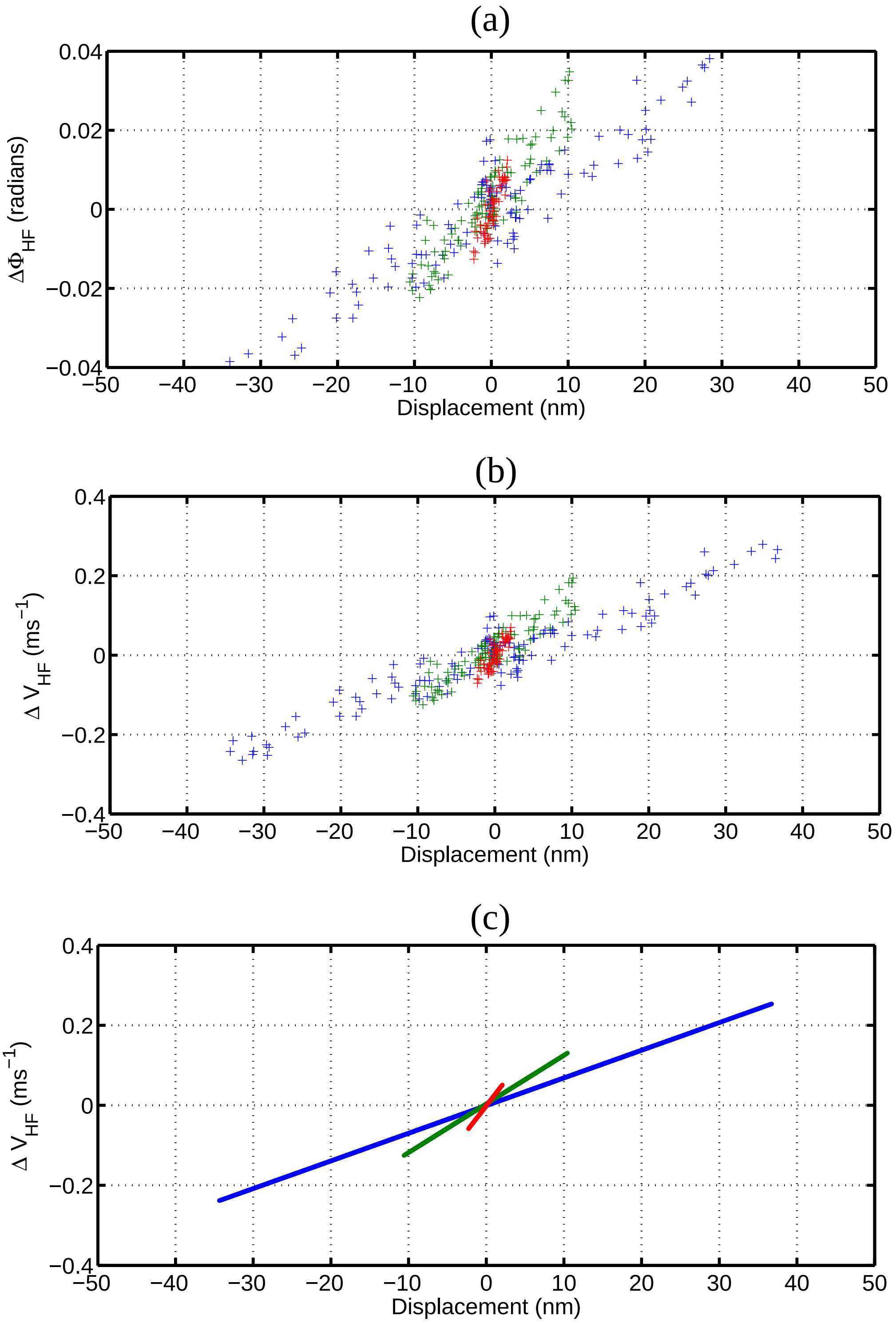

Figure 5.10: Phase (a) and velocity (b) results from a fused silica sample plotted against surface displacement for pump frequencies of 0.5MHz (blue), 1MHz (green) and 2MHz (red). A line has been fitted to the data and is shown in (c). The range of displacement for the higher frequencies is smaller due to the limitations of the transducers.

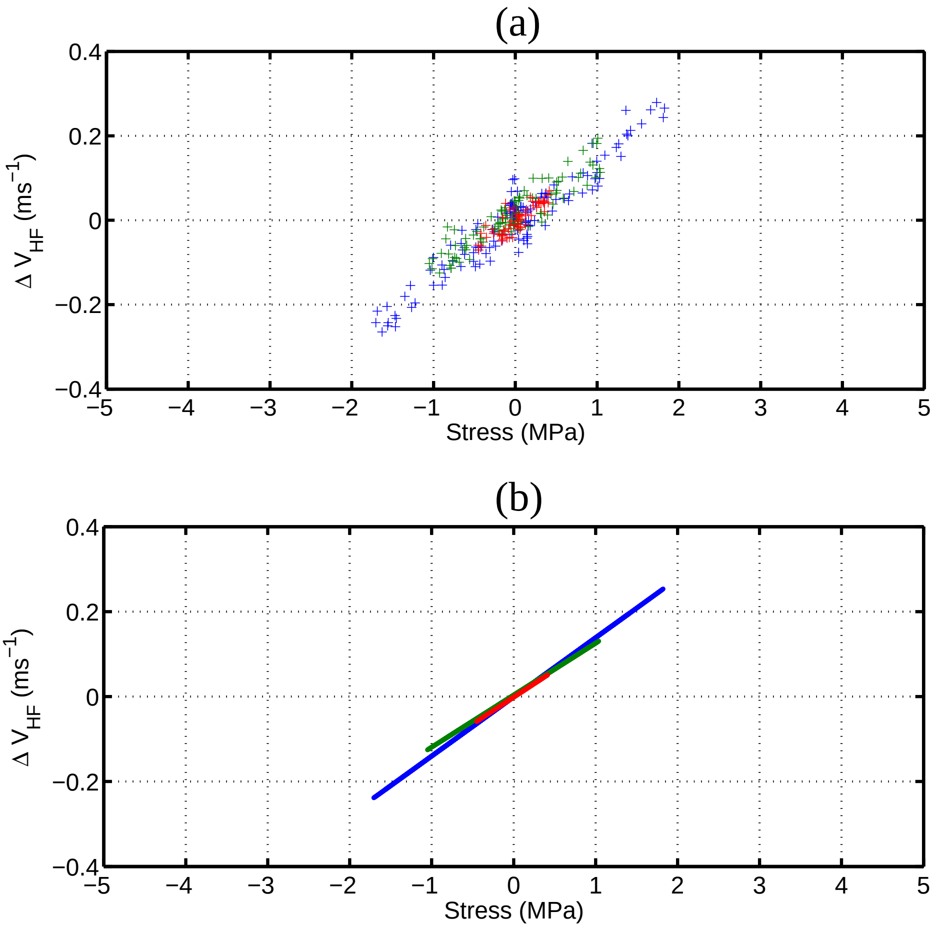

Figure 5.11: Velocity plotted against stress for pump frequencies of 0.5MHz (blue), 1MHz (green) and 2MHz (red) (a) for fused silica. A line has been fitted to the data and is shown in (b). The gradients of these lines are presented in table 5.1.

pulses, the output of the knife-edge detector is filtered with an 82MHz bandpass filter and amplified. Once all the probe data have been captured, part (3) was performed by removing the filter. Provided that the transducer output remained consistent throughout parts (2) and (3), this procedure was perfectly acceptable. However, with the 0.5MHz transducer, it was found that during the first 120 minutes of use, the output gradually increased in amplitude. A possible explanation for this would be that the temperature of the transducer element steadily increased over this period. The other transducers may have been less susceptible to this change in temperature because their element size was 50% smaller and, therefore, reached a steady-state operational temperature more rapidly. The experiments performed using the 1MHz and 2.25MHz transducers showed no evidence of change over time.

5.6 Changing the probe SAW frequency

In all the experiments discussed in this chapter so far, an 82MHz probe SAW was used. The laser system is capable of generating ultrasound at harmonic frequencies of 82MHz (see figure 3.2, section 3.2.1) and in this section, nonlinear experiments performed using 164MHz and 246MHz probe frequencies are presented.

In terms of calculating the stress that the probe SAW experiences, it is advantageous to have a high pump:probe SAW frequency ratio. Theoretically, the stress at the surface is assumed to be purely the σ_{xx} component since $\lambda_{HF} \ll \lambda_{LF}$ and, therefore, the higher the pump:probe frequency ratio, the more this assumption is valid (figure 5.8).

To generate SAWs with the laser system at 164MHz or 246MHz, the line spacing of the SLM image was selected to match the acoustic wavelength at that frequency. This experiment was performed on fused silica, which had a Rayleigh wave velocity of 3393m/s. Hence, 41.4μm, 20.7μm and 10.3μm line spacings were used for 82MHz, 164MHz and 246MHz, respectively. Figure 5.12 shows the probe signal at the three probe frequencies as detected by the knife-edge detector.

For these experiments, a 1MHz transducer was used and the interaction distance between the pump and probe SAWs was kept at 4mm. The interlaced differential data acquisition method was used to suppress the effects of temperature. The phase modulation measurements for each probe frequency are shown in figure 5.13. The raw data (blue) has been digitally filtered and is shown in red. The pump SAW packet is shown in green. There is a high level of correlation between the phase modulation and pump wave packet. The phase of the probe pulse in all three cases has been modulated by the presence of the 1MHz pump SAW. To quantify this modulation, the phase results are first presented with respect to displacement (figure 5.14(a)) and then converted to a velocity modulation (figure 5.14(b)). Lines have been fitted to these data in figure 5.14(c). Figure 5.15(a) shows the velocity modulation results with respect to stress. The gradients of the lines fitted in figure 5.15(b) are presented in table 5.2.

SAW probe Frequency (MHz)	Gradient (mms^{-1}/MPa)
82	126.5±6.1
164	118.3±4.5
246	100.2±5.1

Table 5.2: Velocity-stress gradients acquired from figure 5.15(b) for different probe SAW frequencies.

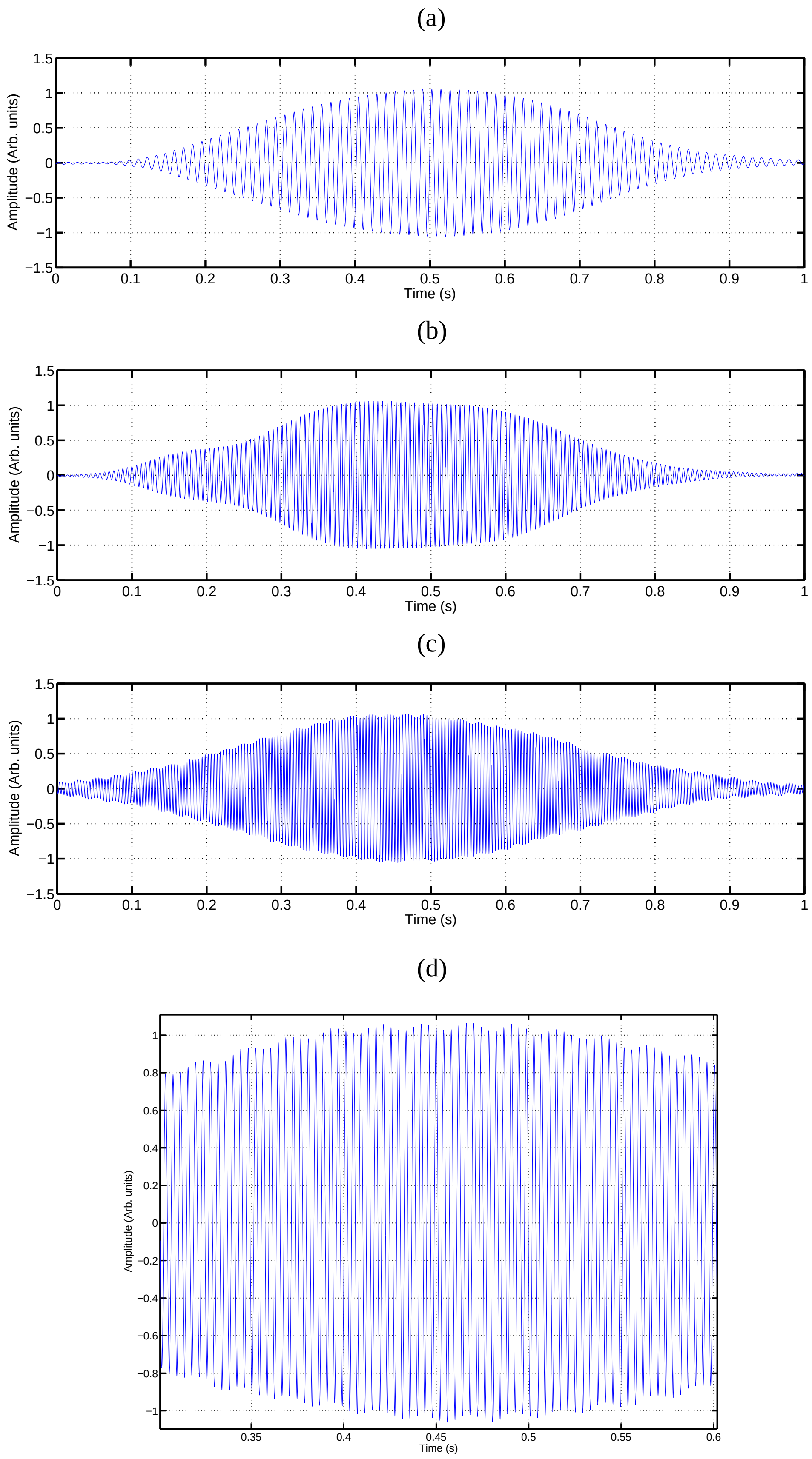

Figure 5.12: The knife-edge detected probe pulses at 82MHz (a), 164MHz (b) and 246MHz (c) used to perform the nonlinear experiments. A zoomed-in picture of the 246MHz signal is shown in (d). The frequency of the laser generated probe pulse is selected by matching the line spacing of the SLM to the acoustic wavelength.

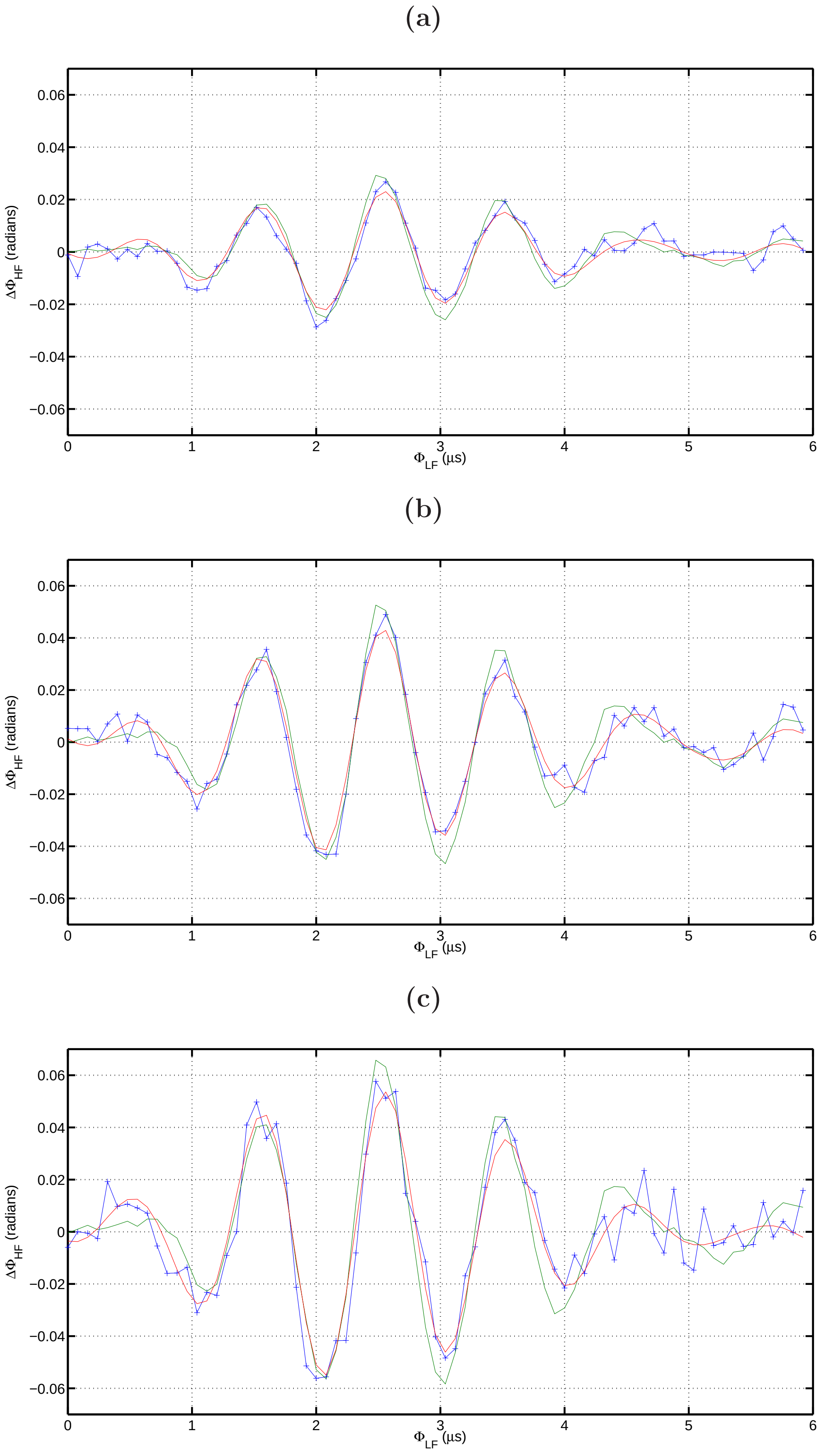

Figure 5.13: Phase modulation measurements (blue) of the 82MHz (a), 164MHz (b) and 246MHz (c) probe frequencies. The data have been filtered and shown in red, and the pump wave packet is shown in green.

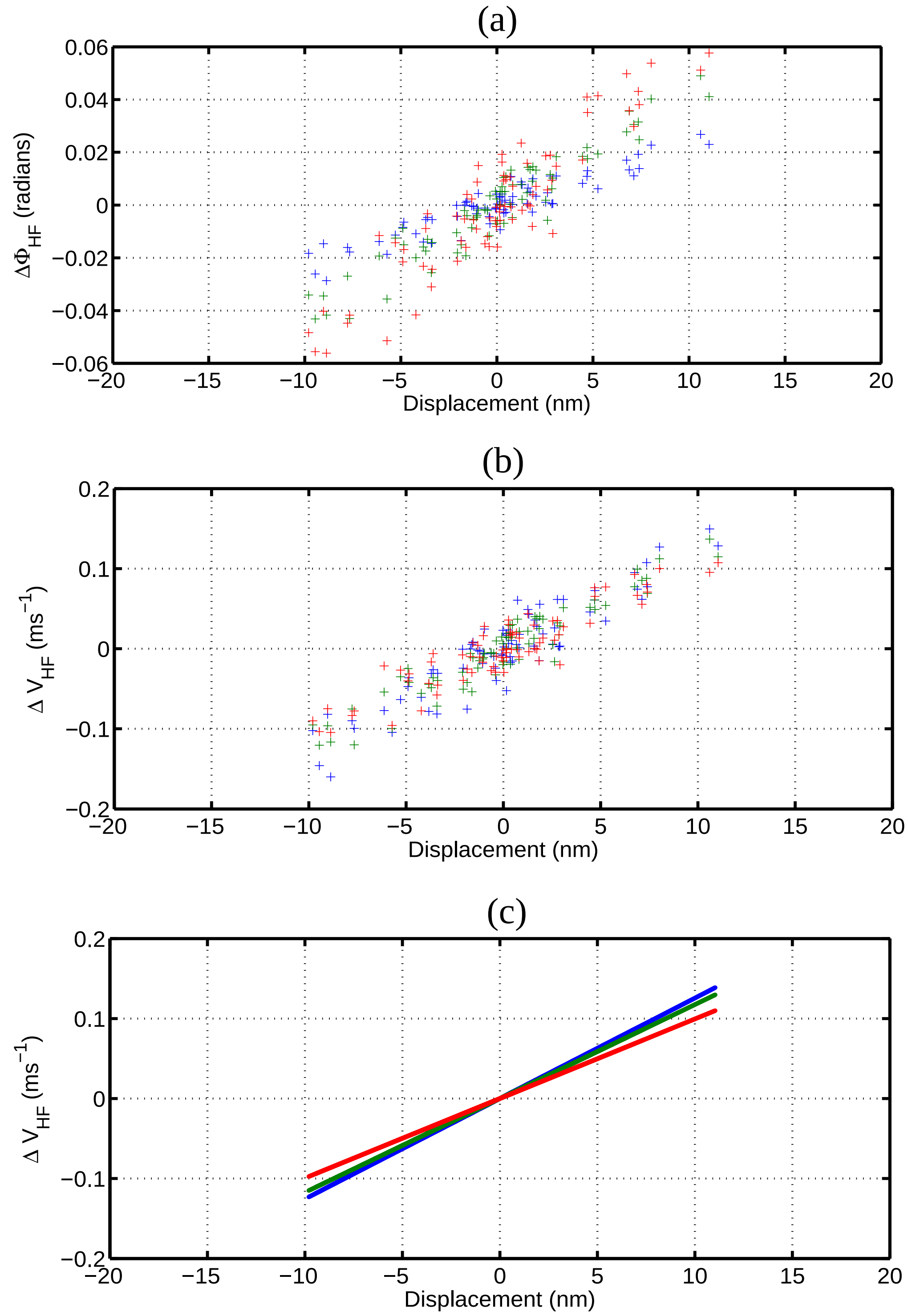

Figure 5.14: Phase (a) and velocity (b) results plotted against surface displacement for probe frequencies of 82MHz (blue), 164MHz (green) and 246MHz (red). A line has been fitted to the data and is shown in (c).

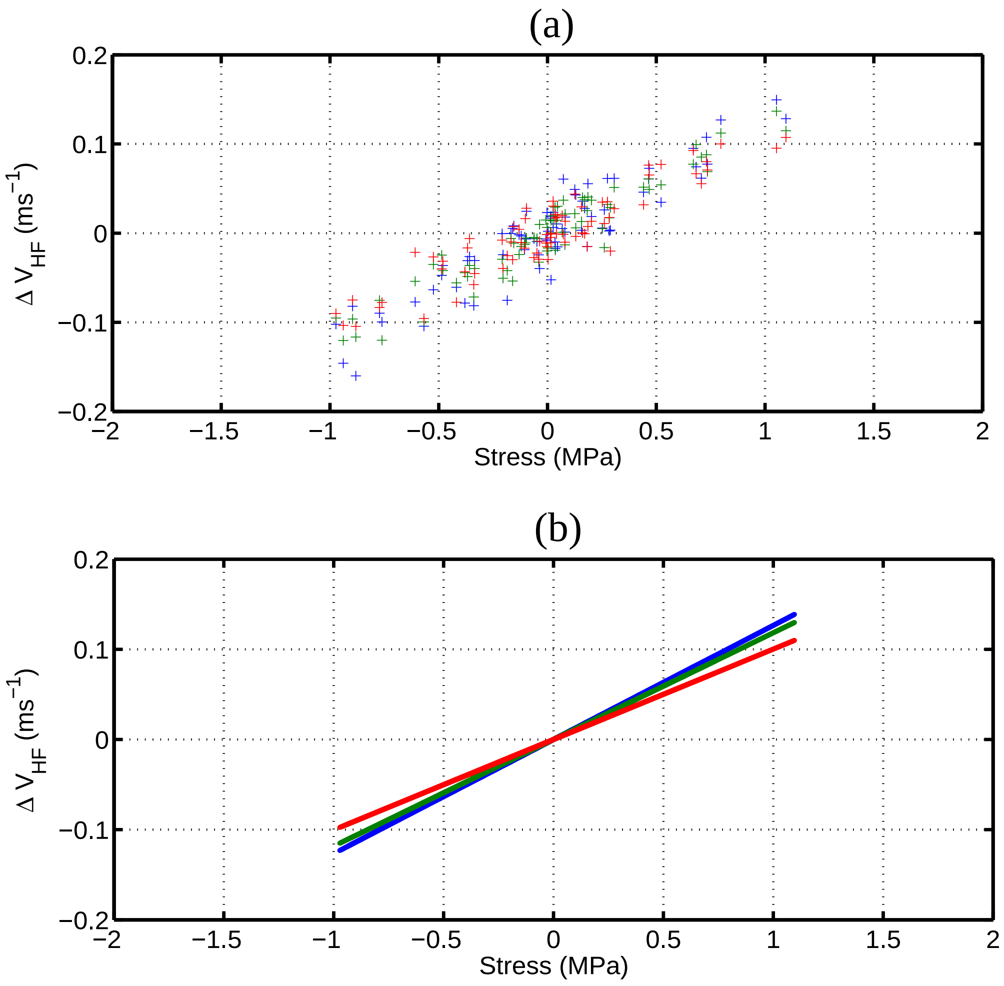

Figure 5.15: Velocity plotted against stress for probe frequencies of 82MHz (blue), 164MHz (green) and 246MHz (red)(a). A line has been fitted to the data and is shown in (b). The gradients of these lines are presented in table 5.2.

5.7 Comparison of nonlinear responses of fused silica and aluminium

Previously reported findings have demonstrated that aluminium and fused silica have opposite nonlinear responses [100, 67, 81, 4]. To validate this, nonlinear experiments were conducted on fused silica, aluminium-2024 and aluminium-6061.

In each experiment the reference delay was set so that the probe SAW interacted with the first peak of the pump SAW packet. This served as a marker so that at this interaction point (reference delay), the corresponding phase measurement was known − thus, allowing a correlation of all other phase measurements and corresponding interaction points.

The first and last target delays were chosen so that they encapsulated the whole of the pump wave packet (5μs in this case), and 80ns delay increments were used so that the probe pulse interacted with 63 points on the pump wave. In order to overcome the effects of changes in temperature on the experiments, results were collected using the differential interlaced data capture method (see section 4.6.3). Phase measurements for all three materials are shown in figure 5.16. The reference delay is indicated by the red circle in each case and it has been aligned with the first peak of the pump wave (shown in blue) so that both sets of data correspond to each other. Clearly, the phase measurements on fused silica and aluminium are 180° out of phase, indicating that with increasing stress, the SAW velocity on one material speeds up while on the other it slows down.

According to the literature [101], the SAW velocity on aluminium is inversely proportional to longitudinal stress. If the velocity slows down, then the phase of the detected signal will become more negative because it will have arrived later in time. The results in figure 5.16 can be adjusted to show this and figure 5.17 shows the phase modulation with actual surface displacement. The unfiltered results are

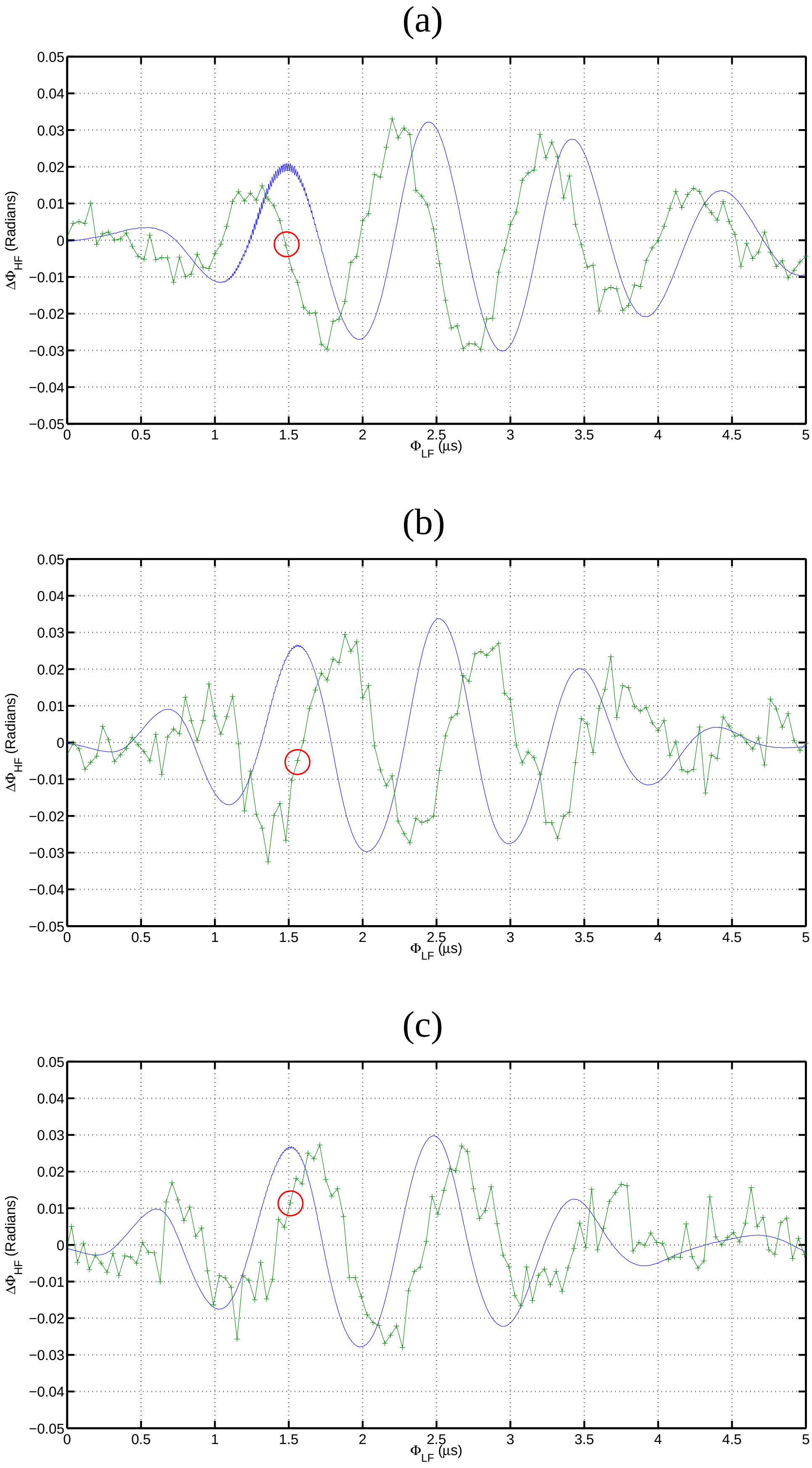

Figure 5.16: Phase modulated probe measurements (green) and a trace of the pump SAW packet (blue) for fused silica (a), Al-2024 (b), Al-6061 (c). The measurement corresponding to the reference delay (indicated by the red circle) is aligned with the pump SAW peak in each case.

plotted against stress in figure 5.18(a) and a line of best fit is plotted in figure 5.18(b) for each of the three materials. The gradients of these lines are presented in table 5.3.

Material	Gradient (mms^{-1}/MPa)
Fused silica	100.1±2.4
Aluminium-2024	−34.4±1.5
Aluminium-6061	−31.9±1.5

Table 5.3: Velocity-stress gradients acquired from figure 5.18(b) for different materials.

The results from this experiment are in agreement with other nonlinear experiments. For example, a mixing pump-probe technique using bulk waves at 2.5MHz and 30MHz, respectively, showed that fused silica had a negative β-parameter, while aluminium, titanium and polystyrene had positive nonlinear parameters [4].

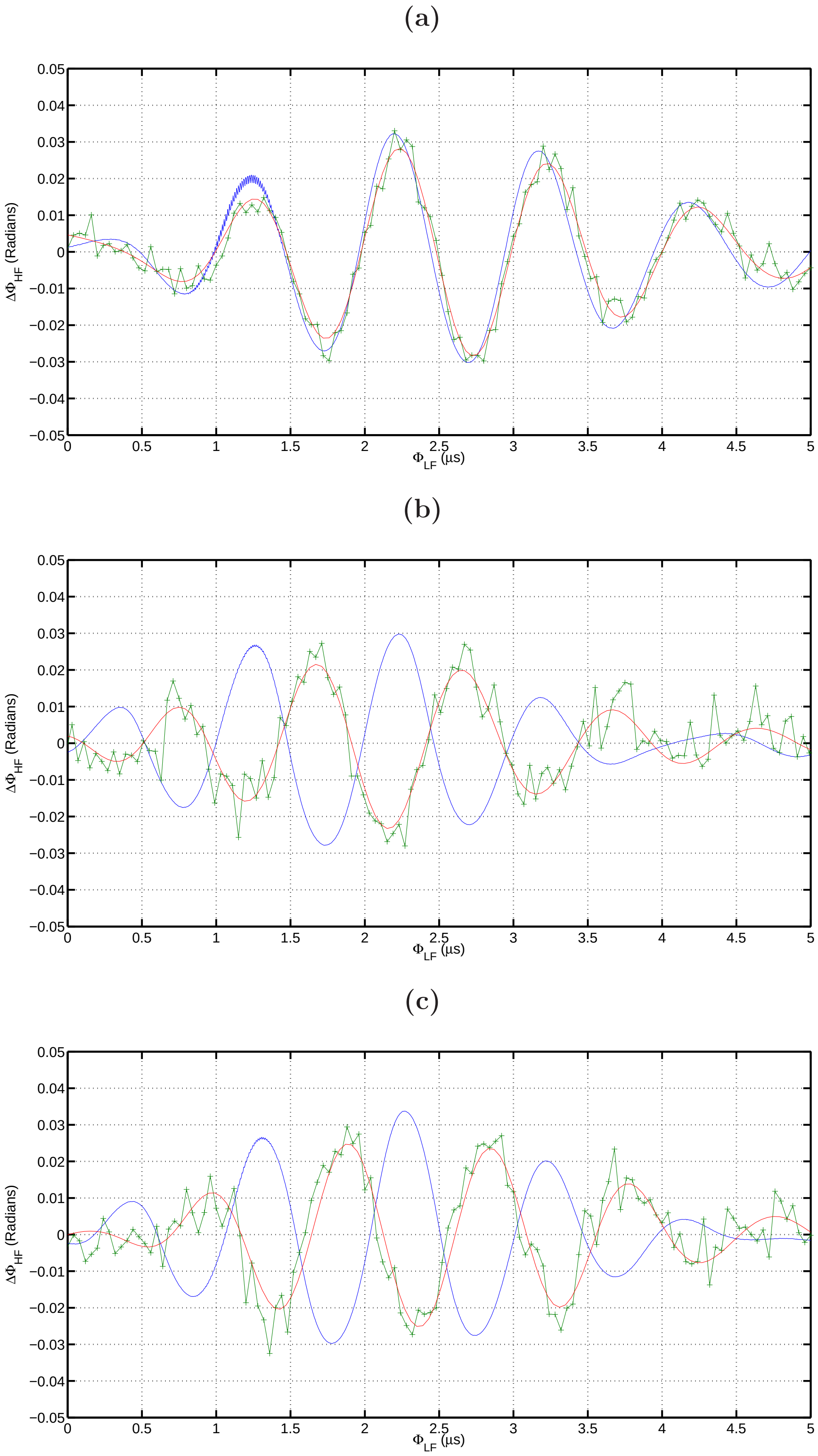

Figure 5.17: The quarter-cycle phase difference between actual and detected surface displacement is removed from the results presented in figure 5.16. The phase modulated probe measurements (green) and a trace of the pump SAW packet (blue) for fused silica (a), Al-2024 (b) and Al-6061 (c). The phase measurements have been filtered and are shown in red in each case.

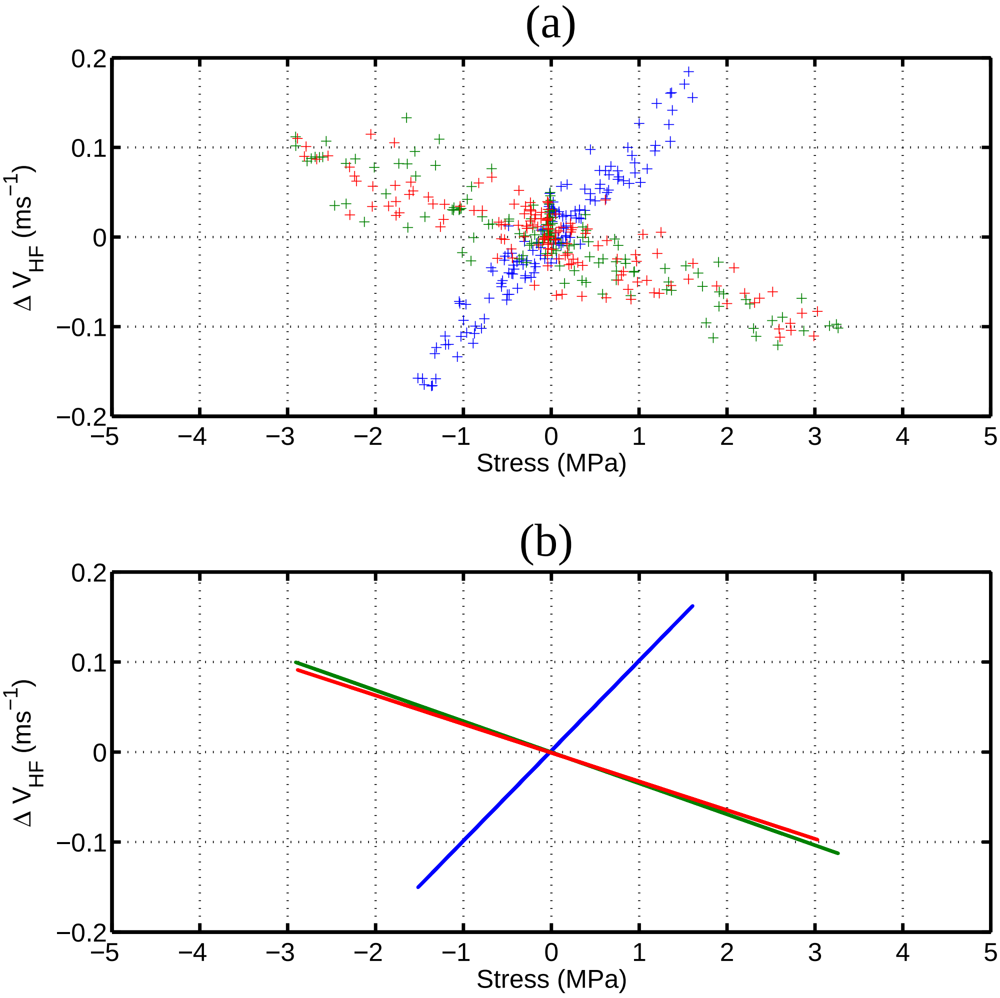

Figure 5.18: Velocity plotted against stress for fused silica (blue), aluminium-2024 (green) and aluminium-6061 (red) (a). A line has been fitted to the data and is shown in (b). The gradients of these lines are presented in table 5.3.

5.8 Nonlinear experiments with CHOTs

In each experiment described so far in this chapter, the high frequency SAW was generated using the SLM and detected by a knife-edge detector. Here, a series of nonlinear experiments were performed that used an alternative method to generate and detect the probe SAW. Two experimental configurations are used in this section and have been described in section 4.4.

1. Generation of the probe SAW using a g-CHOT and detection by a knife-edge detector.
2. Generation of the probe SAW using a g-CHOT and detection by a d-CHOT.

During these nonlinear experiments, the interlaced differential data collection procedure, discussed in section 4.6.3, was used so that the effects of temperature were suppressed. The delay settings were adjusted so that the probe SAW interacted with multiple points on the pump SAW packet, and the corresponding phase modulation experienced by the probe SAW at each of these points was extracted. Figure 5.19(a) and 5.19(b) shows typical probe signals generated by the g-CHOT and detected by knife-edge or d-CHOT detection techniques.

Phase modulation results obtained for both the knife-edge and the d-CHOT detection techniques are shown in figure 5.20(a) and 5.20(b), respectively. In both cases the probe SAW was generated by a plane wave g-CHOT and the interaction distance between the pump and probe SAWs was 4mm.

The pump signal shown in green in figure 5.20 indicates the stress field that the transducer excited on the sample. Different electronic channels were used for detecting the pump and probe signals. Consequently, the delay differences between the two electronic signal paths meant that the signals' time of arrival was also different. For this reason, an arbitrary phase was applied to the pump wave packet so that the probe SAW phase-modulated results coincided with their respective interaction

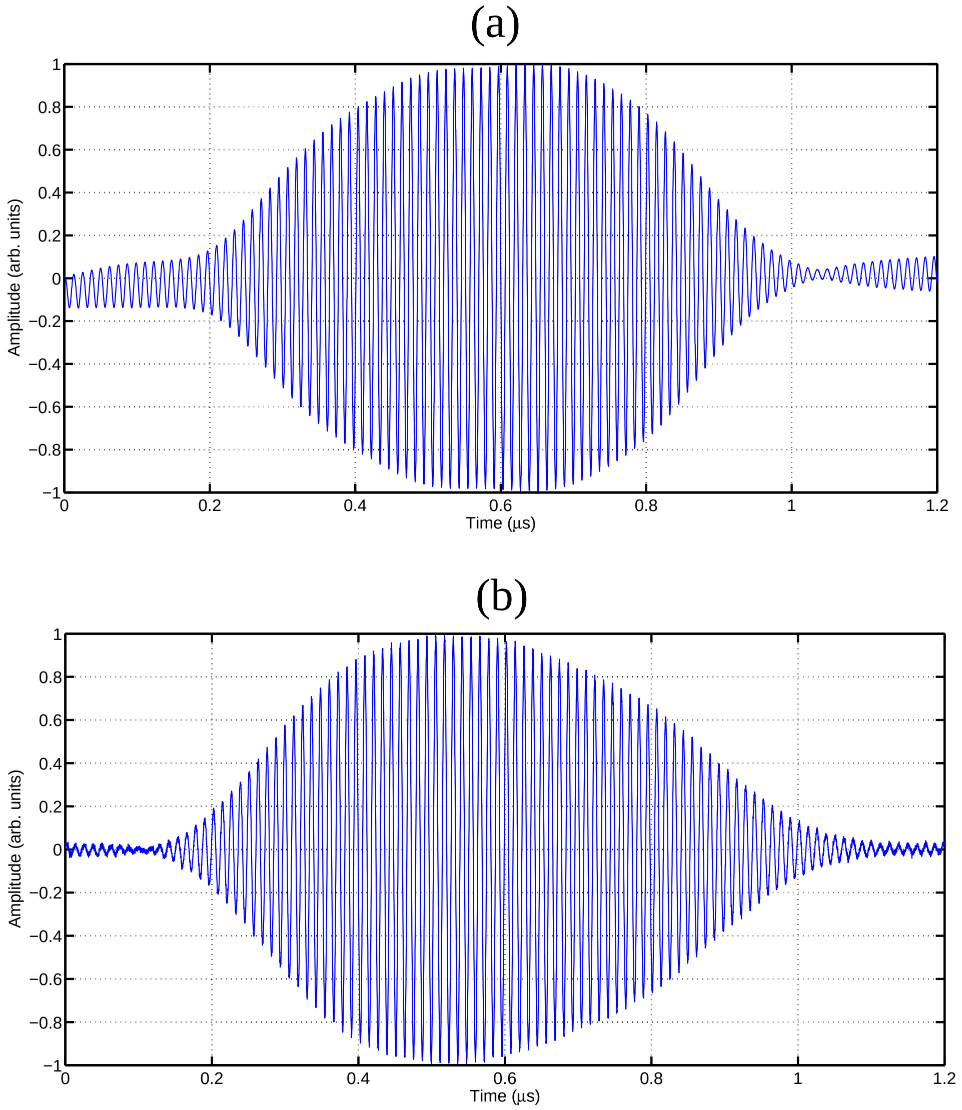

Figure 5.19: A high-frequency SAW pulse generated by a plane wave g-CHOT and detected by the knife-edge detector (a) and a plane wave d-CHOT (b).

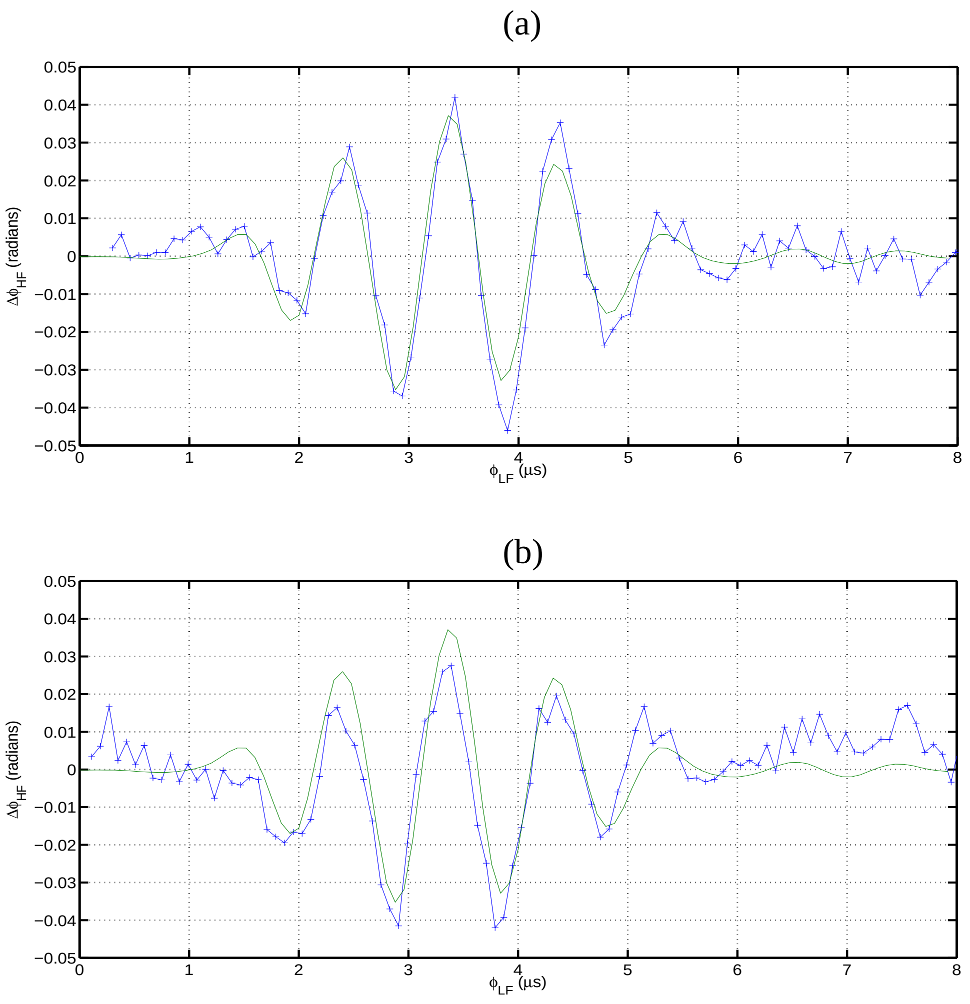

Figure 5.20: Phase modulation ($\Delta\phi_{HF}$) experienced by the knife-edge detected (a) and d-CHOT detected (b) probe pulse at different interaction points with the pump wave packet (shown in green). A g-CHOT generated the high-frequency pulse.

points on the low-frequency wave packet (figure 5.20). In both experiments, the high-frequency pulse was delayed in time in steps of 80ns so that it experienced various stressed states imposed by the low-frequency wave. To compare the results from the two experiments, the phase measurements have been converted to velocity and are plotted against stress in figure 5.21. Lines have been fitted to the data (shown in red) and the gradients of the lines are given in table 5.4.

It can be seen that both the knife-edge detector and the d-CHOT detection techniques, which are completely independent from each other, measured very similar

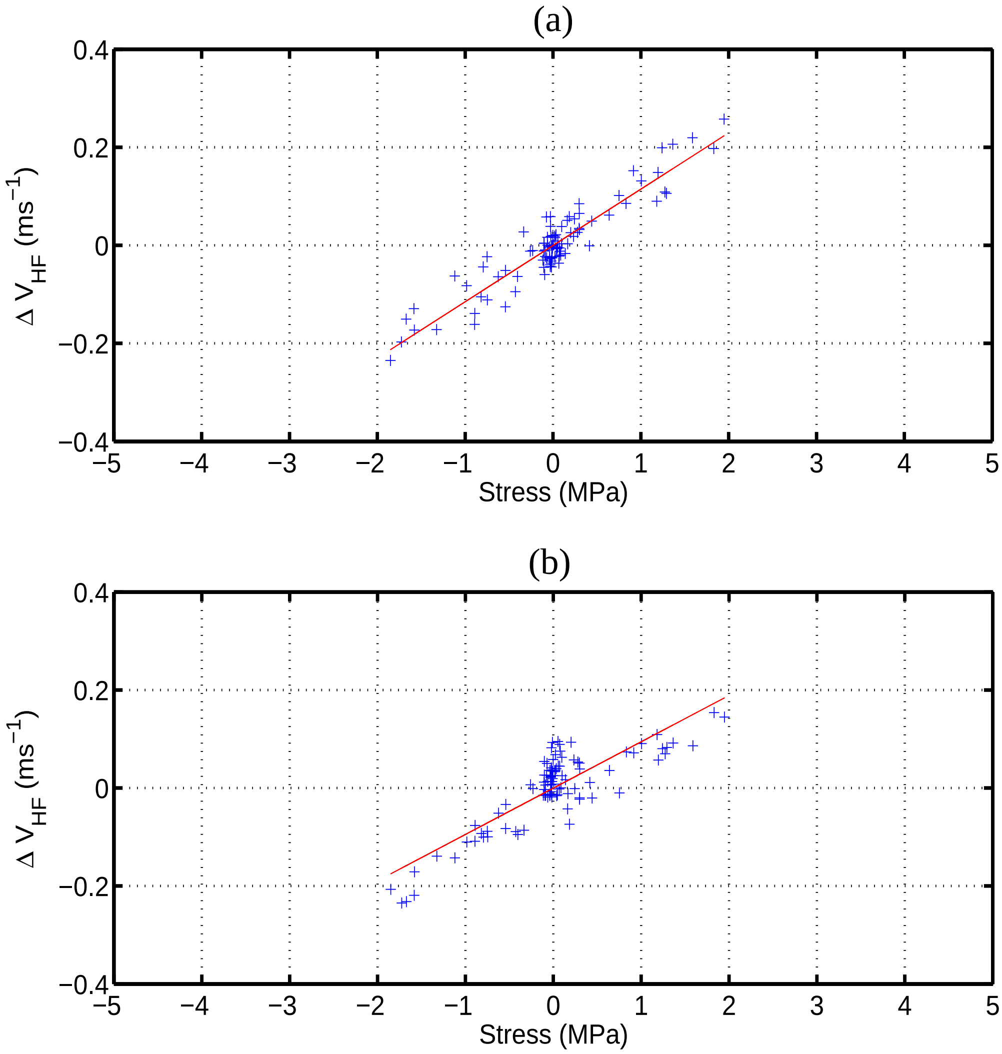

Figure 5.21: Velocity modulation (ΔV_{HF}) of the probe SAW with stress. A g-CHOT generated the high-frequency pulse and was detected by a knife-edge detector (a) and a d-CHOT (b). The gradients of the lines are shown in table 5.4.

phase-modulated results.

Table 5.4 shows that the results obtained with the g-CHOT/d-CHOT experiment are inconsistent with the gradients from other experiments presented in this chapter. The likely reason for the inconsistency between results obtained with the g-CHOT/Knife-edge and g-CHOT/d-CHOT is that the d-CHOT was unable to detect the pump SAW and therefore it was not possible to establish the imposed stress. The stress values used in figure 5.21(b) are actually those obtained from the g-CHOT/knife-edge detector experiment. There must, therefore, be an error in the

Experimental configuration	Gradient (mms^{-1}/MPa)
knife-edge detector	114.9±4.5
d-CHOT	94.6±5.9

Table 5.4: Velocity-stress gradients acquired from figure 5.21 for different detection schemes.

gradient for the g-CHOT/d-CHOT experiment.

This section has discussed how CHOTs can be incorporated into the nonlinear experiment and has allowed for a direct comparison between two completely independent detection techniques. Both the knife-edge and d-CHOT methods have measured similar phase modulations in the high-frequency wave.

5.9 Summary

The aim of all the experiments in this chapter was to demonstrate how nonlinear experiments can be used to measure material nonlinearity. The series of experiments investigating the effect of changing the pump:probe frequency ratio showed that as the pump frequency was increased, the velocity-displacement gradient also increased by approximately a factor of 2.

Combining CHOTs with the nonlinear experiment allowed for a direct comparison between two completely independent detection techniques. Both the knife-edge and d-CHOT methods have measured similar modulations in probe velocity caused by the stress induced by the 1MHz transducer. All the results presented in this chapter in terms of the velocity-stress gradient are summarised in table 5.5. The velocity-stress gradient for fused silica was relatively consistent across all nonlinear experiments. If the results for the 0.5:82MHz and g-CHOT/d-CHOT experiments were omitted (for reasons described in the 'Notes' column), then the mean velocity-stress result is ∼115.2mms^{-1}/MPa.

The results from nonlinear experiments showed that the relationship between applied stress and velocity change for fused silica and aluminium was found to be opposite. In the literature, fused silica was reported to have a negative β-parameter, while metals such as titanium and duraluminium had positive values [4]. From table 5.5, the velocity-stress gradient value for Al-6061 was approximately 30% of that for fused silica. The relative nonlinearity of the two materials is in reasonable agreement with the literature [100], where β-values of 12.4 ± 0.2 (fused silica) and 4.5 ± 0.2 (Al-6061) were presented.

Nonlinear experiment	Material	Pump SAW frequency (MHz)	Probe SAW frequency (MHz)	Gradient ($\text{mms}^{-1}/\text{MPa}$)	Notes
Pump SAW amplitude changed (section 5.4)	Fused silica	1	82	112.8±5.4	
Pump SAW frequency changed (section 5.5)	Fused silica	0.5	82	139.3±3.9	Output from 0.5MHz transducer was not constant - possible cause of error in stress measurements
	Fused silica	1	82	122.4±5.1	
	Fused silica	2	82	126.5±10.4	
Probe SAW frequency changed (section 5.6)	Fused silica	1	82	126.5±6.1	
	Fused silica	1	164	118.3±4.5	
	Fused silica	1	246	100.2±5.1	
Fused silica and aluminium compared (section 5.7)	Fused silica	1	82	100.1±2.4	
	Al-2024	1	82	−34.4±1.5	
	Al-6061	1	82	−31.9±1.5	
Applied CHOTs to experiment (section 5.8)	Fused silica (g-CHOT/Knife-edge)	1	82	114.9±4.5	Error in g-CHOT/d-CHOT experiment since unable to detect pump SAWs (Real stress values unobtainable). Approximated by using stress measurements from g-CHOT/Knife-edge experiment
	Fused silica (g-CHOT/d-CHOT)	1	82	94.6±5.9	

Table 5.5: Summary of results from all the experiments performed in this chapter.

Chapter 6

Conclusion and further work

The aim of this research was to develop a laser-based ultrasonic technique that could measure material nonlinearity. The experiment used a pump-probe wave mixing technique [2] in which the stress exerted by a pump wave caused a material velocity change, thereby modulating the phase of the probe signal.

The work was novel because the experiment was performed using high-frequency SAWs, generated and detected using lasers. The OSAM instrument generated the probe SAW at frequencies of 82MHz (and its harmonics), while the pump SAW was generated by a transducer. The ultrasound was detected by a knife-edge detector. In addition, similar results were obtained using a g-CHOT/d-CHOT system on fused silica.

The main difference between the technique presented here and the previously reported methods [13, 5] is that the stress was imposed by an ultrasonic transducer, rather than a stressing jig. Measuring velocity modulation is challenging, as only relatively small stresses (<10MPa) can be exerted by the transducer. However, this technique has an advantage over other methods because it could be applied to specimens *in situ* i.e. the specimen would not have to be removed from its point of operation to be placed in a jig.

Changes in laboratory temperature were found to cause velocity modulations of a similar order of magnitude as the nonlinear measurements. Ambient temperature variations of ±1°C were sufficient to engulf the measurements, so several temperature suppression methods were developed to overcome this problem. The effects of temperature were resolved by incorporating a temperature-controlled box around the experimental apparatus and/or an electronic data acquisition system.

The principal conclusions for this work are:

1. A laser-based ultrasonic experiment has been developed and is capable of measuring material nonlinearity. Materials that have been tested so far are fused silica and aluminium.

2. Results showed velocity-stress gradients for fused silica, Al-2024 and Al-6061 to be $+115.2\text{mms}^{-1}/\text{MPa}$, $-34.4\text{mms}^{-1}/\text{MPa}$ and $-31.9\text{mms}^{-1}/\text{MPa}$, respectively.

3. The nonlinear responses of fused silica and aluminium have been shown to be opposite in sign, which is in agreement with the literature.

Further work includes the application of this nonlinear experiment to more 'difficult' materials such as titanium, which is commonly used in aircraft engine components. As the grain structure of titanium can cause 82MHz SAWs to be aberrated [102], one of two existing aberration correction techniques would have to be applied [96], in order to perform a nonlinear experiment on this difficult material.

To validate the results presented in this thesis, it is important to compare the results with those obtained using different experimental techniques, such as the mechanically applied stress method described in [13] for example. The materials that were used in each case were different and so in order to have a direct comparison, nonlinear experiments on steel and silicon nitride samples need to be performed.

The main advantages that CHOTs have over the SLM/knife-edge detector system are the greatly reduced cost and complexity of the optical setup required to perform experiments. Although no experiments have been performed using CHOTs on metals, to-date, this is a potential application. In order to generate ultrasound on aluminium for example, the lines of the g-CHOT would have to be made of a material that has either a lower or higher absorption coefficient. Provided that there is a sufficient absorption contrast between the two materials, either of these options would be suitable. The use of a g-CHOT to generate the low-frequency SAW on the test material would have the advantage of making this nonlinear experiment completely non-contact. In order to get the sufficiently high pump SAW amplitudes required for the experiment, there may be a risk of causing damage to the sample surface.

The nonlinear experiments in this thesis were performed on un-fatigued materials, but with a view to applying it to fatigued samples. The elastic properties of a material are affected by fatigue, which can be quantified by the velocity-stress slope. Rolls-Royce have shown considerable interest throughout the duration of this research and a follow-on project has been initiated with a number of academic and industrial partners. The aim of this project is to develop a technique that can measure the residual life of aircraft engine components so that their usable life can be safely and reliably extended. This consortium will prepare a wide range of fatigued samples, which will then be tested using the technique described in this thesis.

Appendix A: Material Properties

Property	Symbol	Fused silica	Aluminium
Rayleigh velocity (m/s)	v	3393	2906
Density (Pa)	ρ	2200	2770
Young's Modulus (GPa)	E	73	70.3
Shear Modulus (GPa)	μ	31	26.1

Table A1: Values used in the analysis in section 1.4.2 [63].

Appendix B: Brief history of the OSAM Instrument

Over the last 15 years, the instrument we now call the OSAM has gone through various stages of development. In 1994, a nonlinear experiment based on measuring changes in SAW velocity caused by an applied static stress was developed [13]. These experiments were performed on silicon nitride and steel samples. A mode-locked Q-switched laser was used as the generation source, and the beam was focused to a single line on the sample using a cylindrical lens. The output of the generation system produced a short burst of SAWs at a fundamental frequency of 82MHz. The detection system consisted of a two-beam homodyne Michelson interferometer. Each of the two beams, which were separated by a known distance, detected the surface displacement caused by the passing SAW. The time delay between the detected SAW signals could then be accurately obtained and the SAW velocity determined.

Around 1996, the generation system implemented computer generated holograms [42] and diffractive acoustic elements [103]. These holograms were capable of generating an arbitrary distribution of light onto the sample surface and therefore, single or multiple lines or arcs could be used to generate SAWs. By using arcs, the ultrasound was focused to a single point, which increased the SNR for the point detection.

By 1998, it was possible to take images of the ultrasound on certain samples. The high-speed analogue electronics that were now an integral part of the system allowed fast acquisition of the complex amplitude of the detected ultrasound. The detection system now consisted of a knife-edge detector. The computer-generated holograms were then replaced by a spatial light modulator [43]. This device was computer-controlled and could be programmed to distribute the light onto the sample in any desired profile. The effects of aberration were then studied and techniques were developed to correct aberration [104, 96, 105, 106, 102].

In 2003, a second OSAM system was built and was called the ARROSAM. The work on aberration correction continued and an acoustic wavefront sensor (AWFS) [107] was incorporated into the ARROSAM. The combination of the SLM and AWFS meant that the higher-order aberration correction method could be implemented more rapidly than with a single knife-edge detector.

In addition, the ARROSAM was used to develop a technique that was capable of mapping the microstructure of multi-grained materials such as titanium alloys and aluminium. This technique was called Spatially Resolved Acoustic Spectroscopy (SRAS) [108, 109].

In 2003, a nonlinear technique was developed that was based on the parametric interaction between the 82MHz SAW generated by the OSAM instrument and a low frequency (0.5−2MHz) stressing SAW. The stress applied to the sample was found to modulate the velocity of the 82MHz SAW [94].

Appendix C: OSAM Alignment

Introduction

There are many elements of the OSAM system that have to be aligned for maximum efficiency. These range from simple everyday tasks, such as focusing the sample, to more major issues, such as re-aligning the generation laser cavity. The latter is rarely performed and is only necessary after major maintenance work has been carried out on the laser.

Laser cavity

The three elements of the laser that are generally adjusted are the two mirrors at each end of the laser cavity and the position of the Q-switcher crystal. The laser beam is expanded and then projected onto a screen and a CCD camera is setup so that the spatial properties of the beam can be observed. The aim is to adjust these laser components to obtain a single circular beam (single mode) with a Gaussian spacial intensity. The coherent trigger pulse 'quality' is a further alignment guide, as this also provides feedback on the temporal properties of the laser. A high amplitude, well-defined coherent trigger pulse, such as the one shown in section 3.2.1, indicates an optimised Q-switched and mode-locked laser system has been attained.

SLM and surrounding optics

The output beam from the laser has to be directed and accurately expanded to the appropriate size to illuminate the SLM. By keeping the laser beam orthogonal at all times and at a consistent height above the optical table ($\sim$10cm), alignment is generally made easier. Once aligned, the first half-wave plate and beam expander system are fixed into place and are rarely adjusted. The optical components enclosed by the dashed box in figure 3.1 (section 3.2) are attached to the same fixture so that there is no relative movement between them. The individual components within it can, however, be adjusted. For example, both beam splitters can be rotated and tilted, the halfwave plate can be easily rotated, the beam block position in the horizontal and vertical planes can be adjusted so that the appropriate area of the SLM is illuminated and the CCD camera can be removed when necessary to accommodate the placement of the temperature controlled box (section 4.6.1). The SLM head is mounted independently on a mechanical stage so that its distance from the sample can be adjusted. It also has in-built tip/tilt adjustments for precise positioning.

Sample

There are three main components of the OSAM instrument that have to be in focus with the sample and, therefore, in focus with each other. These are the SLM, the detection system and the imaging (CCD camera) system. If any one of these is in focus with the sample initially, then the task of aligning the other two parts is made much easier. If this is not the case, and all parts are out of focus, then the alignment process becomes more complicated. This section details the general procedure that was used when the OSAM was in a state of complete mis-alignment.

In order to have the best possible chance of aligning the system, an ‘ideal’ sample is used. This is a flat, smooth, polished mirror with a known velocity (2952m/s). The sample should have one or two scratches as these will be used to focus the CCD camera onto the sample.

The sample scratches are first illuminated by a torch or LED, and the CCD camera position (relative to the sample) is adjusted. When the image of the scratches looks sharp on the camera system, it means that the camera and sample are in focus.

An SLM image is uploaded to the SLM, consisting of a series of plane lines. The line spacing is chosen to match the acoustic wavelength of the sample which is 36μm for an ideal sample. Plane SAWs are used at this stage as there is a greater chance of detecting a signal than with focused waves. Any mis-alignment (which is very probable at the early stages of the alignment process) means it is unlikely that the location of the arc focus is precisely where the detection probe is situated, whereas the detector position is less critical with plane waves.

The SLM position is then adjusted so that the lines become sharp and clearly defined on the CCD camera image. At this point both the SLM and camera are in focus with the sample. If required, the halfwave plate in front of the SLM can be rotated at this stage so that the maximum contrast between light and dark lines of the SLM image is achieved.

The next stage is to get the detector system into focus with the sample. Any scratches, patches of dust or even a finger print present on the surface of the sample will cause the light from the detection laser to be scattered. In order to see the spurious reflections, a white card is temporarily held in front of the sample. The sample position is then moved until these reflections appear sharp and in focus on the white card. When this is achieved, the sample and detector system are in focus.

The focusing lens situated directly in front of the knife edge detector can then be positioned so that the light is shared equally between the two photodiodes. Finally, the SLM line spacing is adjusted to confirm that the 82MHz SAWs are most efficiently generated at a line spacing of 36μm.

Bibliography

[1] SD Sharples, M Clark, and MG Somekh. All-optical adaptive scanning acoustic microscope. *Ultrasonics*, 41:295–299, 2003.

[2] M Vila, F Vender Meulen, S Dos Santos, L Haumesser, and O Bou Matar. Contact phase modulation method for acoustic nonlinear parameter measurement in solid. *Ultrasonics*, 42:1061–1065, 2004.

[3] IA Viktorov. *Rayleigh and Lamb waves: physical theory and applications*. New York: Plenum Press, 1967.

[4] X Jacob, C Barriere, and D Royer. Acoustic nonlinearity parameter measurements in solids using the collinear mixing of elastic waves. *Applied Physics Letters*, 82(6):886–888, 2003.

[5] M Duqennoy, M Ouaftouh, and M Ourak. Determination of stresses in aluminium alloy using optical detection of Rayleigh waves. *Ultrasonics*, 37:365–372, 1999.

[6] Lord Rayleigh. On waves propagating along the plane surface of an elastic solid. *Proceedings of the London Mathematical Society*, 17:4–11, 1885.

[7] C Minton. Inspection of metals with ultrasonic surface waves. *Nondestructive Testing*, 12(4):13–16, 1954.

[8] EG Cook and HE Van Valkenburg. Surface waves at ultrasonic frequencies. *ASTM Bulletin*, pages 81–84, 1954.

[9] G Alers, MA Tennison, RB Thompsom, and BR Tittmann. Visualisation of surface elastic waves on structural materials. *Ultrasonics*, 11(4):174–177, 1973.

[10] R Adler, A Korpel, and P Desmares. An instrument for making surface waves visible. *IEEE Transactions on Sonics and Ultrasonics*, (3):157–161, 1968.

[11] DA Cook and YH Berthelot. Detection of small surface-breaking fatigue cracks in steel using scattering of Rayleigh waves. *NDT and E International*, 34:483–492, 2001.

[12] Q Shan and RJ Dewhurst. Surface-breaking fatigue crack detection using laser ultrasound. *Applied Physics Letters*, 62(21):2649–2651, 1993.

[13] MG Somekh, M Liu, HP Ho, and CW See. An accurate non-contacting laser based system for surface wave velocity measurement. *Measurement Science and Technology*, 6:1329–1337, 1995.

[14] GR Gerhart. Rayleigh wave velocity for a stress-induced slightly anisotropic solid. *Journal of the Acoustical Society of America*, 60(5):1085–1088, 1976.

[15] Y Iwashimizu and O Kobori. The Rayleigh wave in a finitely deformed isotropic elastic material. *Journal of the Acoustical Society of America*, 64(3):910–916, 1978.

[16] B Mi, E Michaels, and TE Michaels. An ultrasonic method for dynamic monitoring of fatigue crack initiation and growth. 119(1):74–85, 2005.

[17] PD Warren, C Pecorari, OV Kolosov, SG Roberts, and GAD Briggs. Characterisation of surface damage via surface acoustic waves. *Nanotechnology*, 7:295–301, 1996.

[18] I Pape, CW Lawrence, PD Warren, SG Roberts, GAD Briggs, OV Kolosov, AW Heys, CF Paines, and BK Tanner. Evaluation of polishing damage in alumina. *Philosophical Magazine A*, 80(8):1913–1934, 2000.

[19] M Clark, SD Sharples, and MG Somekh. Non-contact acoustic microscopy. *Measurement Science and Technology*, 11:1792–1801, 2000.

[20] M Clark, SD Sharples, and MG Somekh. Fast, all optical Rayleigh wave microscope: Imaging on isotropic and anisotropic materials. *IEEE Transactions on Ultrasonics, Ferroelectrics and Frequency Control*, 47(1):65–74, 1999.

[21] P Cawley and DN Alleyne. The use of Lamb waves for the long range inspection of large structures. *Ultrasonics*, 34(2-5):287–290, 1996.

[22] DN Alleyne and P Cawley. The interaction of Lamb waves with defects. *IEEE Transactions on Ultrasonics, Ferroelectrics and Frequency Control*, 39(3):381–397, 1992.

[23] T Hayashi and K Kawashima. Multiple reflections of Lamb waves at a delamination. *Ultrasonics*, 40:193–197, 2002.

[24] S Grondel, C Delebarre, J Assaad, J Dupuis, and L Reithler. Fatigue crack monitoring of riveted aluminium strap joints by Lamb wave analysis and acoustic emission measurement technique. *NDT and E International*, 35:137–146, 2002.

[25] Z Chang and A Mal. Scattering of Lamb waves from a rivet hole with edge cracks. *Mechanics of Materials*, 31:197–204, 1999.

[26] B Culshaw, G Pierce, and P Jun. Non-contact measurement of the mechanical properties of materials using an all-optical technique. *IEEE Sensors Journal*, 3(1):62–70, 2003.

[27] W Gao, C Glorieux, and J Thoen. Laser ultrasonic study of Lamb waves: determination of the thickness and velocities of a thin plate. *International Journal of Engineering Science*, 41:219–228, 2003.

[28] DN Alleyne and P Cawley. Optimisation of Lamb wave inspection techniques. *NDT and E International*, 25(1):11–22, 1992.

[29] EA Ginzel and RK Ginzel. Ultrasonic properties of a new low attentuation dry couplant elastomer. *NDTnet*, 1(2), 1996.

[30] RJ Dewhurst, CE Edwards, ADW McKie, and SB Palmer. Comparative study of wide-band ultrasonic transducers. *Ultrasonics*, 25(6):315–321, 1987.

[31] PR Murray and RJ Dewhurst. A laser/EMAT system for thickness monitoring applications using shear and l-s mode-converted waves. *Measurement Science and Technology*, 12:1651–1659, 2001.

[32] Paul Mcintire. *Nondestructive testing handbook Volume 7, 2nd Edition*. ASNT, 1991.

[33] S Boonsang and RJ Dewhurst. Enhancement of laser ultrasound/electromagnetic-acoustic transducer signals from Rayleigh wave interaction at surface features. *Applied Physics Letters*, 82(19):3348–3350, 2003.

[34] PR Murray and RJ Dewhurst. Application of a laser/EMAT system for using shear and ls mode converted waves. *Ultrasonics*, 40(1-8):771–776, 2002.

[35] GS Kino. *Acoustic waves: Devices, imaging and analogue signal processing*. Prentice-Hall, 1987.

[36] DC Hurley. Nonlinear propagation of narrow-band Rayleigh waves excited by a comb transducer. *Journal of the Acoustical Society of America*, 106(4):1782–1788, 1999.

[37] S Kenderian, BB Djordjevic, and RE Green. Point and line source laser generation of ultrasound for inspection of internal and surface flaws in rail and structural materials. *Research in Nondestructive Evaluation*, 13:189–200, 2001.

[38] PA Doyle and CM Scala. Near-field ultrasonic Rayleigh waves from a laser line source. *Ultrasonics*, 34:1–8, 1996.

[39] RJ Dewhurst and Q Shan. Optical remote measurement of ultrasound. *Measurement Science and Technology*, 10(11):139–168, 1999.

[40] FL di Scalea, TP Berndt, JB Spicer, and BB Djordjevic. Remote laser generation of narrowband surface waves through optical fibers. *IEEE Transactions on Ultrasonics, Ferroelectrics and Frequency Control*, 46(6):1551–1557, 1999.

[41] J Huang, S Krishnaswamy, and JD Achenbach. Laser generation of narrow-band surface waves. *Journal of the Acoustical Society of America*, 92(5):2527–2531, 1992.

[42] M Clark, F Linnane, SD Sharples, and MG Somekh. Frequency control in laser ultrasound with computer generated holography. *Applied Physics Letters*, 72(16):1963–1965, 1998.

[43] SD Sharples, M Clark, and MG Somekh. Efficient and flexible laser ultrasound generation using spatial light modulators. *Electronics Letters*, 37(18):1145–1146, 2001.

[44] T Stratoudaki, JA Hernandez, M Clark, and MG Somekh. Cheap optical transducers (CHOTS) for narrowband ultrasonic applications. *Measurement Science and Technology*, 18:843–851, 2007.

[45] JP Monchalin. Optical detection of ultrasound. *IEEE Transactions on Ultrasonics, Ferroelectrics and Frequency Control*, 33(5):485–499, 1986.

[46] AS Murfin, RA Soden, D Hatrick, and RJ Dewhurst. Laser-ultrasound detection systems: a comparative study with Rayleigh waves. *Measurement Science and Technology*, 11(8):1208–1219, 2000.

[47] CB Scruby and LE Drain. *Laser Ultrasonics, Techniques and Applications*. Adam Hilger, Bristol, UK, 1990.

[48] JP Monchalin. Optical detection of ultrasound at a distance using a confocal fabry-perot interferometer. *Applied Physics Letters*, 47(1):14–16, 1985.

[49] JB Hoyes, Q Shan, and RJ Dewhurst. A non-contact scanning system for laser ultrasounic defect imaging. *Measurement Science and Technology*, 2(7):628–634, 1991.

[50] M Klein, B Pouet, and P Mitchell. Photo-emf detector enables laser ultrasonic receiver. *Laser Focus World*, 36(8):S25–S27, 2000.

[51] L Noui and RJ Dewhurst. A laser beam deflection technique for the quantitative detection of ultrasonic Lamb waves. *Ultrasonics*, 31(6):425–432, 1993.

[52] RL Whitman and A Korpel. Probing of acoustic surface perturbations by coherent light. *Applied Optics*, 8(8):1567–1576, 1969.

[53] J Lawall and E Kessler. Michelson interferometry with 10pm accuracy. *Review of Scientific Instruments*, 71(7):2669–2675, 2000.

[54] JH Yi, SH Kim, and YK Kwak. A nanometric displacement measurement method using the detection of fringe peak movement. *Measurement Science and Technology*, 11:1352–1358, 2000.

[55] L Bjorno. Forty years of nonlinear ultrasound. *Ultrasonics*, 40(1-8):11–17, 2002.

[56] YP Zheng, RG Maev, and IY Solodov. Nonlinear acoustic applications for material characterisation: A review. *Canadian Journal of Physics*, 77(12):927–967, 1999.

[57] EN Simons. *Testing of Metals*. David and Charles: Newton Abbot, 1972.

[58] N Ranganathan and P Mazot. Changes in elastic constants associated with fatigue damage in an aluminium alloy. *Material Science and Engineering*, 147:161–166, 1991.

[59] PB Nagy, G Blaho, and L Adler. Excess nonlinearity in materials containing microcracks. *Review of Progress in Quantitative Nondestructive Evaluation*, 13:1997–1994, 1994.

[60] PB Nagy. Fatigue damage assessment by nonlinear ultrasonic materials characterization. *Ultrasonics*, 36:375–381, 1998.

[61] PP Delsanto. *Universality of nonclassical nonlinearity: Applications to nondestructive evaluations and ultrasonics*. Springer, 2007.

[62] JD Achenbach. *Wave propagation in elastic solids*. North-Holland, 1973.

[63] GWC Kaye and TH Laby. *Tables of Physical and Chemical Constants*. J Wiley and Sons, 1993.

[64] H Ledbetter. Sound velocities, elastic constants: Temperature dependence. *Material Science and Engineering A*, (442):31–34, 2006.

[65] MF Hamilton and DT Blackstock. *Nonlinear Acoustics*. Academic Press, 1998.

[66] JK Na, JH Cantrell, and WT Yost. Linear and nonlinear ultrasound properties of fatigued 410cb stainless steel. *Review of Progress in Quantitative Nondestructive Evaluation*, 15:1347–1352, 1996.

[67] RB Thompson, O Buck, and DO Thompson. Higher harmonics of finite amplitude ultrasonic waves in solids. *Journal of the Acoustical Society of America*, 59(5):1087–1094, 1976.

[68] MA Breazeale. The ubiquitous nonlinearity: Its origin in solids. *Ultrasonics symposium*, pages 1–10, 1987.

[69] O Buck, L Morris, and JM Richardson. Acoustic harmonic generation at unbonded interfaces and fatigue cracks. *Applied Physics Letters*, 33(5):371–373, 1978.

[70] DJ Barnard. Variation of nonlinearity parameter at low fundamental amplitudes. *Applied Physics Letters*, 74(17):2447–2449, 1999.

[71] K Jhang and K Kim. Evaluation of material degradation using nonlinear acoustic effect. *Ultrasonics*, 37:39–44, 1999.

[72] K Jhang. Applications of nonlinear ultrasonics to the NDE of material degradation. *IEEE Transactions on Ultrasonics, Ferroelectrics and Frequency Control*, 47(3):540–548, 2000.

[73] A Hikata, BB Chick, and C Elbaum. Dislocation contribution to the second harmonic generation of ultrasonic waves. *Journal of Applied Physics*, 36(1):229–236, 1965.

[74] JH Cantrell and WT Yost. Nonlinear ultrasonic characterisation of fatigue microstructures. *International Journal of Fatigue*, 23:S487–S490, 2001.

[75] EGH Lean, CC Tseng, and CG Powell. Optical probing of acoustic surface-wave harmonic generation. *Applied Physics Letters*, 16(1):32–35, 1970.

[76] DC Hurley and CM Fortunko. Determination of the nonlinear ultrasonic parameter b using a Michelson interferometer. *Measurement Science and Technology*, 8:634–642, 1997.

[77] A Moreau. Detection of acoustic second harmonics in solids using a heterodyne laser interferometer. *Journal of the Acoustical Society of America*, 98(5):2745–2752, 1995.

[78] J Herrmann, J Kim, LJ Jacobs, J Qu, JW Littles, and MF Savage. Assessment of material damage in a nickel-base superalloy using nonlinear Rayleigh surface waves. *Journal of Applied Physics*, 99(12):Art. No. 124913, 2006.

[79] JL Blackshire, S Sathish, J Na, and J Frouin. Nonlinear laser ultrasonic measurements of localized fatigue damage. *Review of Quantitative Evaluation*, 22:1479–1487, 2003.

[80] J Frouin, S Sathish, TE Matikas, and JK Na. Ultrasonic linear and nonlinear behaviour of fatigued Ti-6Al-4V. *Journal of Materials Research*, 14(4):1295–1298, 1999.

[81] P Li, WP Winfree, WT Yost, and JH Cantrell. Observation of collinear beam-mixing by an amplitude modulated ultrasonic wave in a solid. In *1983 Ultrasonics Symposium*, pages 1152–1156, 1983.

[82] KEA Van den Abeele, PA Johnson, and AM Sutin. Nonlinear elastic wave spectroscopy (NEWS) techniques to discern material damage, part 1: Nonlinear wave modulation spectroscopy (NWMS). *Research in nondestructive evaluation*, 12(1):17–30, 2000.

[83] DM Donskoy and AM Sutin. Vibro-acoustic modulation nondestructive evaluation technique. *Journal of Intelligent Material Systems and Structures*, 9(9):765–771, 1998.

[84] AM Sutin and DM Donskoy. Vibro-acoustic modulation nondestructive evaluation technique. In *Conference on Nondestructive Evaluation of Aging Aircraft*, pages 226–237, 1998.

[85] KEA Van den Abeele, AM Sutin, J Carmeliet, and PA Johnson. Micro-damage diagnostics using nonlinear elastic wave spectroscopy (NEWS). *NDT and E International*, 34(4):239–248, 2001.

[86] V Zaitsev and P Sas. Nonlinear response of a weakly damaged metal sample: A dissipative modulation mechanism of vibro-acoustic interaction. *Journal of Vibration and Control*, 6(6):803–822, 2000.

[87] V Yu Zaitsev, AM Sutin, I Yu Belyaeva, and VE Nazarov. Nonlinear interaction of acoustical waves due to cracks and its possible usage for crack detection. *Acoustical Physics*, 46(4):427–432, 2000.

[88] D Donskoy, A Sutin, and A Ekimov. Nonlinear acoustic interaction on contact interfaces and its use for nondestructive testing. *NDT and E International*, 34(4):231–238, 2001.

[89] AM Sutin and DM Donskoy. Nonlinear vibro-acoustic nondestructive testing technique. In *8th International Symposium on Nondestructive Charaterisation of Materials*, pages 133–138, 1998.

[90] Z Yan and PB Nagy. Thermo-optical modulation for improved ultrasonic fatigue crack detection in Ti-6A1-4V. *NDT and E International*, 33:213–223, 2000.

[91] P le Bas, K Van Den Abeele, S Dos Santos, T Goursolle, and O Bou Matar. Experimental analysis for nonlinear time reversal imaging of damaged materials. In *9th European conference on NDT, Berlin*, 2006.

[92] K Van Den Abeele, T Kathowski, and C Mattei. Nonlinear acoustic and ultrasonic NDT of aeronautical components. In *Innovations in Nonlinear Acoustics: 17th International Symposium on Nonlinear Acoustics*, pages 75–78, 2006.

[93] SD Sharples. *All-optical scanning acoustic microscope*. PhD thesis, The University of Nottingham, 2003.

[94] IJ Collison, T Stratoudaki, M Clark, and MG Somekh. Measurement of elastic nonlinearity using remote laser ultrasonics and CHeap optical transducers and dual frequency surface acoustic waves. *Ultrasonics*, in press.

[95] ED Palik. *Handbook of optical constants of solids*. London: Academic Press, 1998.

[96] SD Sharples, M Clark, and MG Somekh. Dynamic higher-order correction of acoustic aberration due to material microstructure. *Applied Physics Letters*, 81(12):2288–2290, 2002.

[97] IJ Collison, T Stratoudaki, M Clark, and MG Somekh. Measurement of elastic nonlinearity using remote laser ultrasonics with CHeap optical transducers and dual frequency surface acoustic waves. In *International Congress on Ultrasonics*, 2007.

[98] K Salama and CK Ling. The effect of stress on the temperature dependence of ultrasonic velocity. *Journal of Applied Physics*, 51(3):1505–1509, 1980.

[99] LG Parratt. *Probability and experimental errors in science: an elementary survey*. Dover Publications, inc. New York, 1961.

[100] GE Dace, RB Thompson, and O Buck. Measurement of the acoustic harmonic generation for materials characterization using contact transducers. *Review of Progress in Quantitative Nondestructive Evaluation*, 11:1685–1692, 1991.

[101] M Kato, T Sato, and K Ando. Determination of the higher-order elastic compliance constants of metals from measurements of the dependence of ultrasound velocity on stress. *Journal of the Acoustical Society of America*, 101(4):2111–2121, 1997.

[102] SD Sharples, M Clark, IJ Collison, and MG Somekh. Adaptive acoustic imaging using aberration correction in difficult materials. *Insight*, 47(2):78–80, 2005.

[103] SD Sharples, M Clark, and MG Somekh. Noncontact continuous wavefront/diffractive acoustic elements for Rayleigh wave control. *Electronics Letters*, 74(24):3604–3606, 1999.

[104] SD Sharples, M Clark, and MG Somekh. All-optical adaptive scanning acoustic microscope. *Ultrasonics*, 41(4):295–299, 2003.

[105] IJ Collison, SD Sharples, M Clark, and MG Somekh. Adaptive correction for acoustic imaging in difficult materials. In *Review of Progress in Quantitative Nondestructive Evaluation*, volume 24A and 24B 760, pages 1616–1621, 2005.

[106] JA Hernandez, M Clark, IJ Collison, M Somekh, and SD Sharples. Statistical characterisation of metals from ultrasonic aberrations. In *2005 IEEE Ultrasonics Symposium*, volume 1-4, pages 1139–1142, 2005.

[107] SD Sharples, M Clark, and MG Somekh. Surface acoustic wavefront sensor using custom optics. *Ultrasonics*, 42:647–651, 2004.

[108] SD Sharples, M Clark, and MG Somekh. Fast noncontact imaging of material microstructure using local surface acoustic wave velocity mapping. In *Proceedings of 2005 IEEE Ultrasonics Symposium*, pages 886–889, 2005.

[109] SD Sharples, M Clark, and MG Somekh. Spatially resolved acoustic spectroscopy for fast noncontact imaging of material microstructure. *Optics express*, 14(22):10435–10439, 2006.